Master Thesis report
Technische Universiteit Delft

Single Laser Adaptive Optics system for the ELT/METIS

Feasibility and performance study

Benjamin Arcier

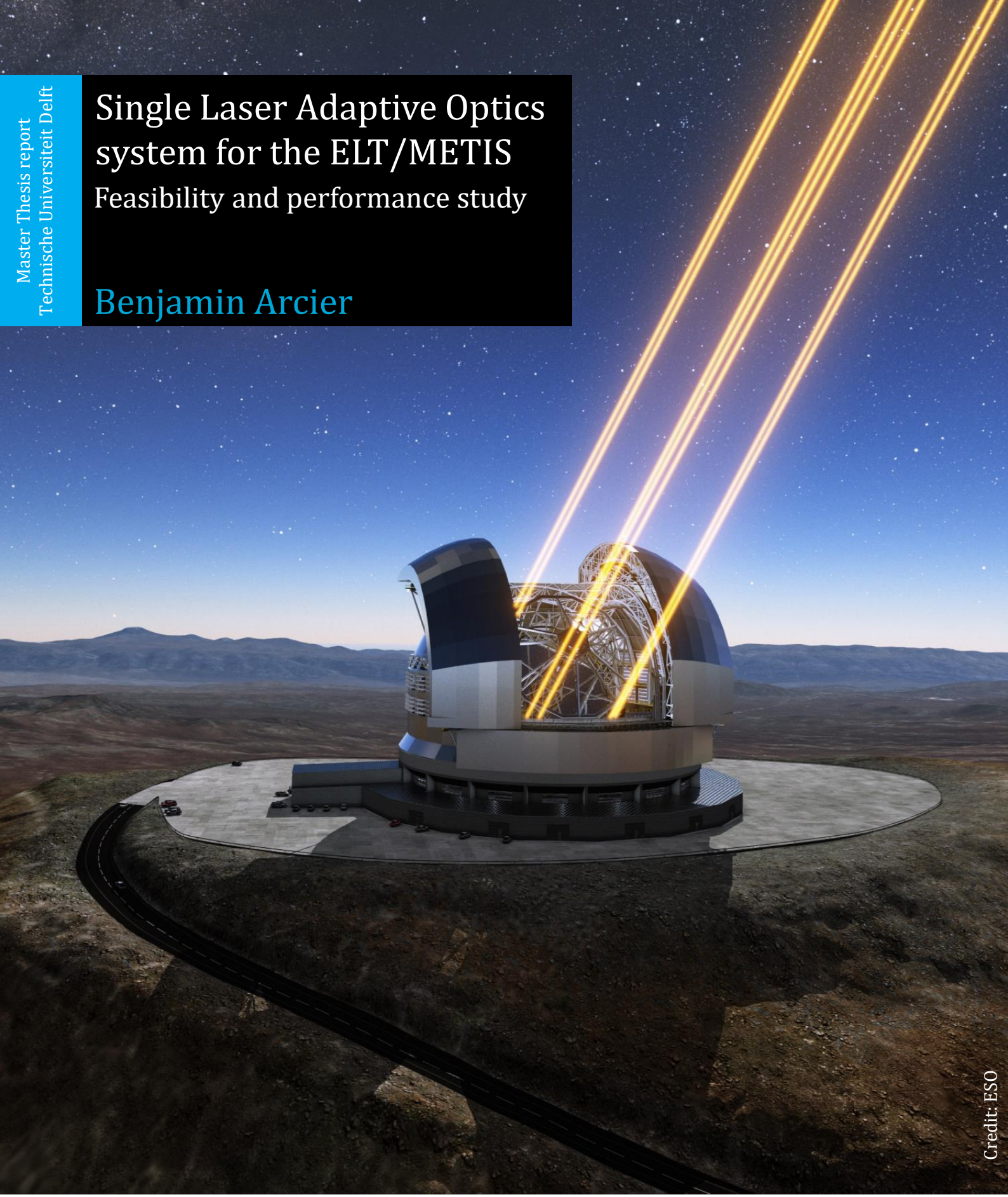

Credit: ESO

TU Delft Delft University of Technology

Challenge the future

N° student: 4627660

Defense date: 13/12/2018

Single Laser Adaptive Optics system for the ELT/METIS

Feasibility and performance study

by

Benjamin Arcier

MSc Student at TU Delft

as part of

MSc Space Flight - Space Exploration

in MSc. Aerospace Engineering

at Delft University of Technology

Tutor:	Pr. Bernhard Brandl	TU Delft / Leiden University
	Dr. Remko Stuik	Leiden University

Committee:	Pr. Bernhard Brandl	TU Delft / Leiden University
	Dr. Remko Stuik	Leiden University
	Dr. Stephanie Cazaux	TU Delft
	Dr. Hans Kuiper	TU Delft

TU Delft Delft University of Technology

Preface

First of all, I would like to thank Pr. Bernhard Brandl: from the day I went to his office, he has guided me during all my Master at TU Delft. Then, I would like to thank Emeric Le Floc'h, who was my tutor during my internship at CEA-Saclay: he is the person that introduced me to the astrophysics world, giving me the keys to progress in this domain. Finally, I would like to thank Dr. Remko Stuik, who had to endure all my questions during these 9 months of research. Questions for which he always took time to answer, which allowed me to understand complicated concepts way faster than what I would have done by my own means.

My roommates also supported me during my researches in the Netherlands, being the first public of my advances throughout the months. And of course, nothing would have been possible without the help of my family, my friends and my girlfriend, who gave be the strength and advise to finish my studies.

Life rises out of death, death rises out of life, in being opposite they yearn to each other, they give birth to each other and are forever reborn. And with them all is reborn, the flower of the apple tree, the light of the stars.

Ursula K. Le Guin, *The Farthest Shore*

Abstract

Demonstrated by the James-Webb Space Telescope launch, the scientific community shows more and more interest in mid-infrared observations. The diffraction limit of an instrument is inversely proportional to the diameter of the telescope: the larger the primary mirror, the higher the resolution. Therefore, the instrument METIS (Mid-Infrared ELT-based Imager and Spectrograph), based on the 37-meter aperture Extremely Large Telescope, will take advantage of the giant mirror to achieve an unrivaled resolution in mid-infrared. However, to reach this limit, the perturbations created by the temperature fluctuations in the atmosphere need to be removed by Adaptive Optics (AO).

METIS will already have an AO system, called Single Conjugate Adaptive Optics (SCAO). However, this system will require a Natural Guide Star (NGS) with a K-band magnitude of $m_K = 11$. This limits considerably the sky coverage where the atmospheric compensation (thus high-resolution observations) could be done. The idea is to use an artificial guide star, called Laser Guide Star (LGS), to get rid of this constraint. This is performed by shooting a laser at the 90-km sodium layer, tuned so that it excites the atoms there that re-emits toward the ground. For a telescope with the size of the ELT, several lasers are recommended in a configuration called Laser Tomography AO or Multi-Conjugate AO. The plurality of the lasers allows removing errors such as the focus anisoplanatism. However, because of the complexity and cost of such a solution, the only available answer for the ELT/METIS is a Single Laser AO system (SLAO). This will be less complex and expensive at the expense of a decrease in the performances. The question is: what are the performances of such a SLAO system, and how could it be made?

The Yorick Adaptive Optics (YAO) simulator has been used to estimate the performances of the SLAO system for the ELT/METIS. The elongation of the LGS beam, created by the finite thickness of the sodium layer, plays a crucial role in the process and has direct consequences on the performances. A parameter analysis has been performed to define the most suitable Field of View, number of sub-apertures, pixels size to tackle the problem. An algorithm has also been developed in MATLAB, coupled with the results from the YAO algorithm. The goal of this algorithm was to estimate the correction that could be brought by the so-called truth sensing on the features left by the LGS correction because of the beam elongation. This sensing will require a natural guide star coupled with the existing SCAO sensor of the METIS instrument and will work in addition to the SLAO sensor. Once the parameters settled, it has been possible to create an optical design with ZEMAX. Because the distance between the telescope and the sodium layer varies relatively to the zenith angle, the focal point of the LGS beam changes accordingly: the optical system needs to tackle this. It was also required to find a solution to separate the LGS beam from the science beam: two solutions have been described, with their advantages and limitations detailed. Finally, a mechanical implementation of the system has been made to explain how such a system could be hanged.

The work performed has allowed estimating the Strehl ratio obtained for the SLAO system with the ELT/METIS, which would be around 60%. These results have been confirmed by the European Southern Observatory and their AO experts. The study made on the truth sensing of the system has allowed putting constraints on the natural guide star brightness required ($m_K < 16.5$), and the sky coverage of the SLAO system which would be almost 100%. The optical design made with ZEMAX has shown great performances so that the perturbations induced by the system are small enough to be able to measure correctly the ones created by the atmosphere. The solution proposed with the mechanical design could pave the way for further study in the domain.

The Adaptive Optics with a single laser guide star is complicated, especially for a telescope with the size of the ELT. Using a laser guide star instead of a natural one creates additional complications that need to be solved to achieve good performances, especially if only one LGS can be used. The solution proposed would allow to considerably increase the sky coverage of the system, which is currently limited to few percents with the SCAO system. However, further studies need to be done, such as the evaluation of the real impact of the NGS magnitude on the system performances, or the design of the complete and realistic mechanical design.

Contents

List of Figures

List of Tables

List of Acronyms, Abbreviations and Units

Acronyms

AGN	Active Galactic Nuclei
ALMA	Atacama Large Millimeter/sub-millimeter Array
AO	Adaptive Optics
APD	Avalanche Photo-Diode
CCD	Charge Coupled Device
COMPASS	COMputing Platform for Adaptive optics SystemS
CuRe	Cumulative Reconstructor
CuReD	Cumulative Reconstructor with domain Decomposition
DC	Dark Current
ESA	European Space Agency
ESO	European Southern Observatory
ELT	Extremely Large Telescope
FFT	Fast Fourier Transform
FoV	Field of View
FWHM	Full Width at Half Maximum
HST	Hubble Space Telescope
IFU	Integrated Field Unit
JWST	James Webb Space Telescope
LGS	Laser Guide Star
LHC	Large Hadron Collider
LLT	Laser Launcher Telescope
LTAO	Laser Tomographic Adaptive Optics
MCAO	Multi-Conjugate Adaptive Optics
METIS	Mid-infrared ELT Imager and Spectrograph
MIR	Mid-InfraRed
MIRI	Mid-InfraRed Instrument
NGS	Natural Guide Star
NIRSpec	Near-InfraRed Spectrograph
OCTOPUS	Optimized Cluster Tool for aO Parallel Ultimate Simulations
PAH	Polycyclic Aromatic Hydrocarbons
PI	Principle Investigator
PSF	Point Spread Function
PWFS	Pyramid Wave-Front Sensor
QE	Quantum Efficiency
RON	Read-Out Noise
SCAO	Single Conjugate Adaptive Optics
SLAO	Single Laser Adaptive Optics
SED	Spectral Energy Distribution
SH-WFS	Shack-Hartmann Wave-Front Sensor
SLAO	Single Laser Adaptive Optics
SMBH	Super Massive Black Hole
SR	Strehl Ratio
S/N	Signal to Noise ratio
TT	Tip/Tilt
VISIR	VLT Imager and Spectrometer for mid-InfraRed
VLT	Very Large Telescope
WF	Wave-Front
WFS	Wave-Front Sensor
YAO	Yorick Adaptive Optics

Units

AU Astronomical Units (Sun-Earth distance $\approx 150 \times 10^6 km$)

erg Erg - Luminosity unit ($1\ erg = 10^{-7} J$)

ly Light-Year ($1\ ly \approx 9.46 \times 10^{15} m$)

Lo Solar luminosity $L_\odot \approx 3.83 \times 10^{26} W$

Mo Solar mass $M_\odot \approx 2 \times 10^{30} kg$

pc Parsec (Distance at which 1 AU is seen under 1": $1\ pc \approx 3.4\ ly$)

Jy Jansky - Flux density unit ($1\ Jy = 10^{-26}\ W.m^{-2}.Hz^{-1}$)

str Steradian - Angular surface ($1\ str = 1\ rad^2$)

Å Angström - Wavelength Unit (1 Å $= 0.1\ nm$)

Sr Strehl ratio - Ratio between the maximum of the real PSF over the diffraction limited one

Notes

In this report, the instruments and the telescopes on which they are (will be) based will sometimes be noted as **Telescope/Instrument**, so it is easier to identify.

Chapter 1

Introduction and context

Contents

From the Galilean lenses to the first telescopes with mirrors, humankind has continuously tried to improve the instrumentation performances. The purpose was to see dimmer and dimmer light sources in space so that the mechanisms that drive the universe formation and evolution could be understood more in-depth. In extra-galactic science, high-quality instrumentation allows observing the galaxy formation at early epochs (Oteo et al., 2017 [55]), to more precisely observe the structure of the Universe, the composition of the interstellar and intergalactic medium or even to better understand the physics behind Super-Massive Black-Holes at the center of almost every galaxy (Netzer, 2015 [52]). Telescopes such as the Hubble Space Telescope (HST) have been sent into space not to be disturbed by the perturbations induced by our planet's atmosphere. This instigated a complete revolution in astronomy, with pictures showing thousands of galaxies in few square-arcmin portions that were appearing empty in the first place (Beckwith et al., 2006 [5]): the universe is vast, filled with billions of galaxies that contain hundred billion of stars. However, sending a telescope to space puts constraints on its characteristics, particularly the size of its mirror. The James Webb Space Telescope (JWST) and its 6.5-meter mirror will be the largest mirror ever launched, and that already represents an incredible challenge: sending larger mirrors is for the moment unthinkable. Therefore, even if they have a tremendous sensitivity, space-based telescopes have their resolution limited by the size of their primary aperture. The round primary mirror of the telescope acts like the two-dimensional long-slit of the Young diffraction experiment. The light coming from the object observed is interfering with itself, because of its wave nature. This is creating the Airy patterns that limit the resolution of the instrument.

On the ground, telescopes with 8-meter mirrors or more already exist (VLT, Subaru or Keck for example): in theory, these telescopes could reach a higher resolution than space-based ones. However, to achieve these performances, the perturbations from the atmosphere need to be removed. This will even be more critical for the Extremely Large Telescope (ELT), with its 37-meter apertures: to reach the diffraction limited resolution and use 100% of the resolution capacities provided by their gigantic primary mirror, Adaptive Optics (AO) systems are required (Tyson and Frazier, 2012 [78]).

The subject of this Master Thesis is to study the Adaptive Optics solution for one of the 3 first-light instruments of the Extremely Large Telescope (ELT): the Mid-infrared ELT-based Imager and Spectrograph (METIS) that will perform both galactic and extragalactic science.

1.1. The ELT/METIS

1.1.1. Presentation of the Extremely Large Telescope

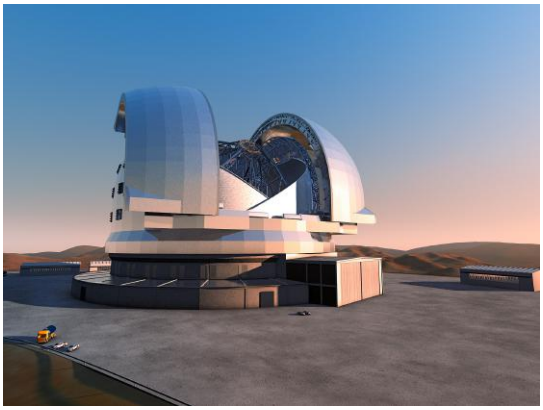

(a) The Extremely Large Telescope (ELT) (ESO, 2011 [25])

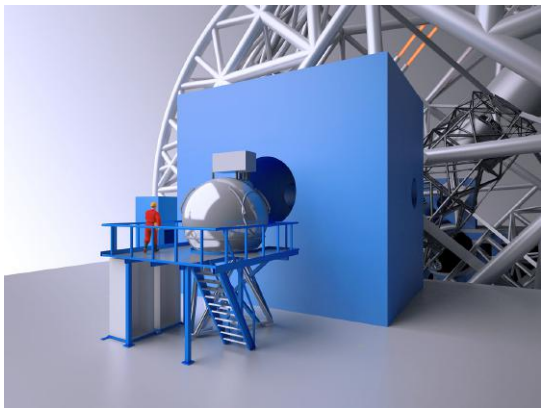

(b) The METIS instrument on the nasmyth plateform Brandl et al., 2016 [15]

Figure 1.1: The 39-meter telescope and one of its instrument: METIS

The Extremely Large Telescope ELT is a reflector telescope with the largest primary mirror (for optical/IR observations) that will be built in 2022 (ESO, 2011 [25]). The circular aperture will have a diameter of 37.3 m, for a collecting area of 978 m^2 and a focus number $f/17.48$. The size of this aperture not only increases the sensitivity for point sources compare to the former generation of ground-based telescopes, it also increases the spatial resolution. Indeed, the diffraction limited resolution is inversely proportional to the diameter of the telescope aperture. However, as stated before, one needs to get rid of the atmospheric turbulence that limits the resolution of the telescope. Without it, the resolution that could be obtained would be the same as a 20 cm telescope (at 0.5 μm). The size of the primary mirror, composed of 798 hexagonal mirrors, is only 5 cm thick. Deformations inherent to the weight, temperature fluctuations, segments alignment are unavoidable: they have an impact on the telescope performances and need to be compensated. The solution is to make an active control on the telescope's mirrors to compensate for the perturbations. This control is the key for this telescope, and it will not reach its maximum performances without it.

The optical path of the ELT consists on five mirrors (see Figures 1.2a and 1.2b), with the fifth one directing the light beam toward a Nasmyth platform where the instruments will be located. The function of these mirrors are:

M1 The first mirror is segmented, with a diameter of approximately 37 m and an 11.1-meter central obstruction. This mirror is mounted on actuators, with the possibility for each primary mirror segments to move in piston and tip/tilt to compensate for temperature fluctuations and gravity. This mirror is in charge of collecting the maximum amount of light and focus it on the M2, which explains its concavity and its size.

M2 The second mirror is an active one with a diameter of 4.2 m for a weight of 12 tonnes. It will be hanged above the M1 mirror.

M3 The tertiary mirror is 3.8 m across and will be used to refocus together with M2 and M4 mirrors.

M4 The quaternary mirror is the deformable mirror at very high frequencies that will be able to compensate for the atmospheric perturbations. This will be discussed more in details below.

M5 The fifth mirror of the ELT is responsible for the low order perturbations from the atmosphere and the tip/tilt/field-stabilization. The 2.6×2.4 m mirror is a fast steering mirror. This mirror is inclined at ≈ 52.75 deg and mounted on a rotating stage to serve both Nasmyth platforms (Barriga et al., 2014 [4]).

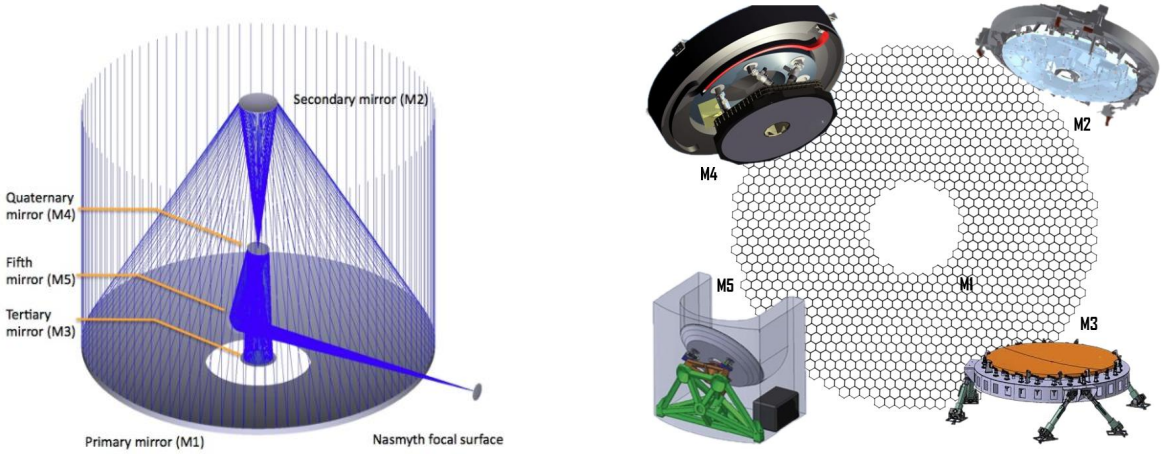

(a) The mirror configuration for the ELT

(b) Current design for the ELT mirrors

Figure 1.2: The optical path of the ELT (ESO, 2011 [25])

1.1.2. The Mid-Infrared ELT based Imager and Spectrograph METIS

METIS is a mid-infrared imager and spectroscope based on the ELT telescope (Brandl et al., 2016 [15]). It will be located on the Nasmyth platform of the ELT, along with the two other first light instruments of the telescope (see Chapter 7 for more information).

It will cover the L- ($2.9-4\ \mu m$), M- ($4.6-5\ \mu m$) and N- ($7.5-13\ \mu m$) band. The instrument will provide imaging with coronography (the fact of hiding the central brightest object to be able to observe the surrounding, particularly useful for exo-planet science) on the M- and N bands, medium-resolution spectroscopy (long-slit spectroscopy) over the L and M bands and high-resolution Integral Field Unit spectroscopy (IFU) in the L and M bands ($2.9-5\ \mu m$). METIS will be an instrument mainly designed for exo-planets characterization, but a part of its science case is focused on extra-galactic science. The Figure 1.3 represents an optical overview of the instrument. A video that can be found at `http://media.astron.nl/various/Other_projects/METIS_MOVIE/flash.html` presents the instrument. Although most of the characteristics are outdated, it gives a good overview of the ELT/METIS. These are the main functions of the different instrument's components:

SLAO This is the project that will be conducted during this Master Thesis. The first element of the SLAO is a beam splitter. Two solutions are currently under discussion: the first one would be an annular mirror that reflects the beam from the laser guide star (slightly de-focused since it is at a finite distance). The second one would be a dichroic. The part of the beam coming from the laser is then sent to the zoom optics that will adapt the focal length of this beam so that the focus will always be made on the fixed wavefront sensors. Chapter 2 and 6 will go further into details.

WCU The Warm Calibration Unit is used to calibrate the instrument before its use. A point source will be generated by this unit and send directly to the METIS instrument. It allows for example to measure the transmission of the device and to calibrate it to interpret correctly the science observations that will be made with it. This calibration unit will be located above the cryostat.

Window The window represents the delimitation between the cryostat and the warm part of the instrument. This part undergoes the considerable temperature differences (−200°C in the cryostat). It must be large enough for enabling the desired field of view, sufficiently thin for maximizing the optical transmission but also sufficientlyresistant so that it will not break (and transform the inside of the cryostat into a $14M€$snowball !). Moreover, it must let go through a broad band in the infrared, from the K-band ($\approx 1.1\mu m$ to the N- band ($\approx 13\mu m$).

CFO ,The Common Fore Optics, is the unit that will "prepare" the science beam for the analysis by the imager and spectroscope. The first instrument is the cold stop, which is responsible for removing the background emissions created by the spiders that suspend the M2-mirror. Then the de-rotator is used:

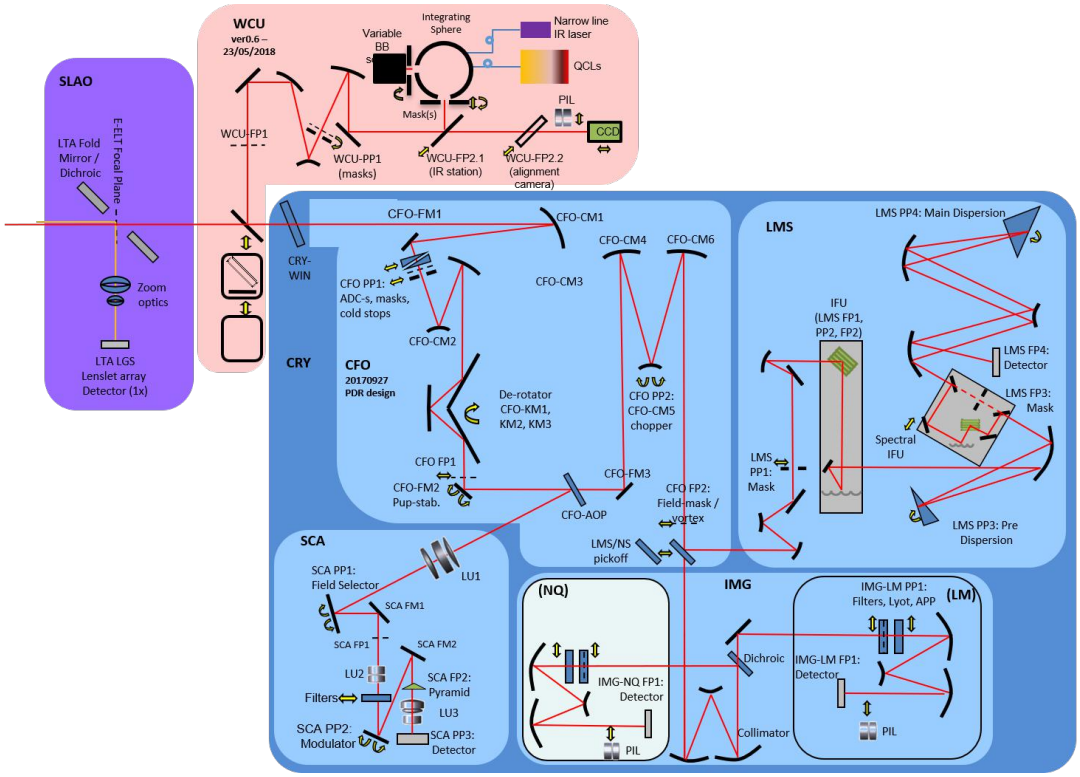

Figure 1.3: The optical system overview of METIS (Brandl et al., 2016 [15])

the ELT is tracking a star in the sky by rotating along its axis during the night. However, this rotation means that the field is also revolved around the targeted point. The de-rotator will compensate for this rotation. Finally, the chopper will remove the thermal background created at the location of the target, by slightly rotating a mirror to observe the sky portion nearby the target. Since there is no source in this zone, the signal measured is the background signal. By doing this on both sides of the science target, it is possible to interpolate the background level at this location and to subtract it.

SCAO The Single Conjugate Adaptive Optics uses the AO-pickoff to recover the signal. This pickoff reflects the K-band part of the beam while letting the L-, M- and N-band signals go through it. The beam is reflected on a field selector, which is used to select a guide source that is not necessarily in the center of the FoV. It is then sent to the wavefront sensors, where the signal will be analyzed as it will be explained after.

IMG The Imager in the L-, M- and N-band is the first instrument of METIS. This imager includes long slit spectroscopy and a coronagraphy for high contrast imaging. A dichroic is again used to split the light between the L-/M- bands and the N-band.

LMS An Integral Field Unit spectroscopy (IFU) in the L- and M-band, including a mode with extended instantaneous wavelength coverage.

This instrument will be the condensate of several instruments that are already based on the VLT such as CRIRES (IFU in L- and M-band) and VISIR (imager in M-, N-band), which explains the complexity of the ELT/METIS.

1.2. The high-resolution astronomy in the mid-infrared

The Mid-infrared astronomy is becoming more and more critical for the astrophysics community: several of the principal instruments created have observed or will observe in this wavelength range like JWST/MIRI (Ressler et al., 2008 [62]), SPICA/MIRACLE (Nakagawa, 2008 [51]), VLT/VISIR (Rio et al., 1998 [63]) or Spitzer/IRAC (Werner et al., 2004 [80]). Figure 1.4 represents the Mid-infrared wavelength with L-, M- and N-bands.

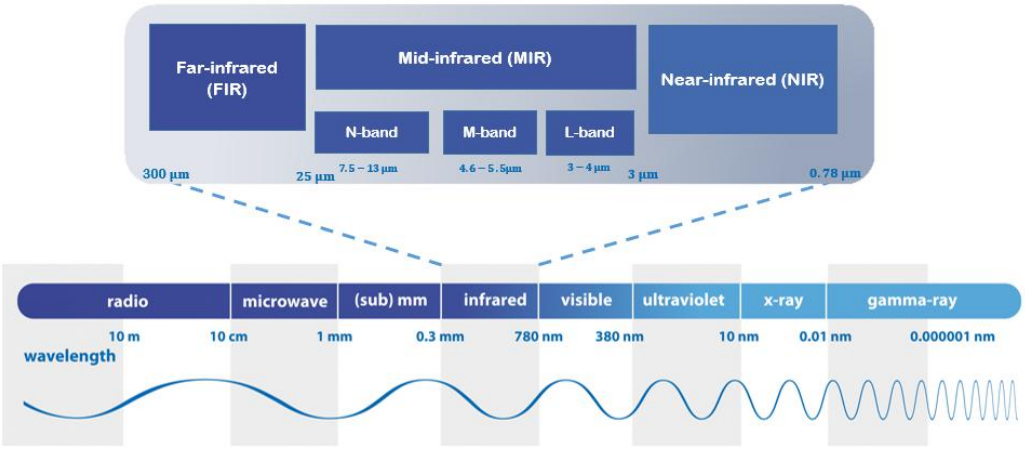

Figure 1.4: The light spectrum, with a focus on the ELT/METIS wavelengths

The reason why these bands are more and more observed lies in the unique information that they can provide (Le Floch́, 2016 [45]). Below a summary of the main extra-galactic science that could be performed with the instrument is summarized. The focus is made on the extra-galactic science because this is the one susceptible to be improved mainly by the Single Laser Adaptive Optics system. The appendices A, B and C detail the work that has been performed during my internship at CEA-Saclay, with a focus on the science that could be made with the ELT/METIS.

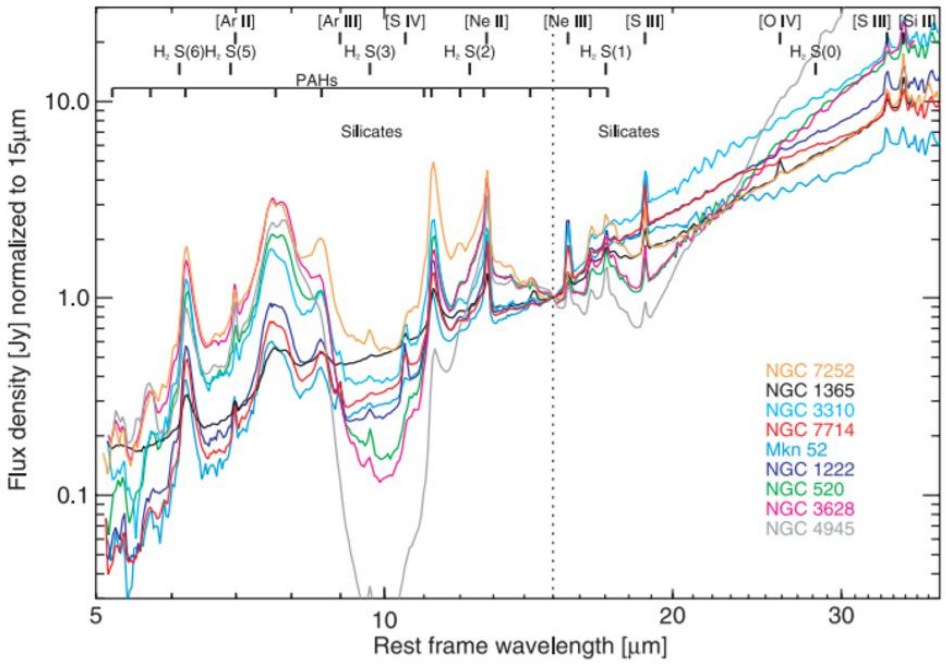

Figure 1.5: Galaxies spectrum of starburst galaxies in the mid-infrared.(Brandl et al., 2006 [10]). The nature of the main emission lines observed are written on the top left.

- In the L-band ($3-4\ \mu m$), the instrument will observe for example the continuum emission from the Rayleigh-Jean part of the cold stars' spectra. Because these cold, less massive stars are the most numerous and dominate with their mass the total stellar population, measuring their luminosity gives information about the mass of the stars observed in the galaxy. It can also give some indications about the age of the stellar population, their metallicity (Sparke and Gallagher, 2007 [74]). A spectrometer in this band could also detect the presence of typical lines that are emitted by the environment of very hot stars created in star formation regions. There is the $C-H$ stretch mode of a Polycyclic Aromatic Hy-

drocarbons (PAH) at 3.3 μm for very close galaxies. It is also possible to detect the H-α line (0.656 μm), which is a typical tracer for star formation activity redshifted in the L-band for $z \approx 3.6-6.1$. This tracer is less influenced by the extinction than UV light, which gets absorbed in the majority by the dust. Since the first star-forming galaxies were probably dusty, this characteristic is primordial for the study of the long distance ones.

- In the M-band ($4.6-5\ \mu m$), the emission in the continuum from very hot dust could be detected, while the one from cold stars emissions becomes too faint. This dust is heated by Active Galactic Nuclei (AGN), whose activity is locally way more energetic than other phenomena such as star formation. Since the emission wavelength of dust (considered as a black-body) depends on its temperature, this wavelength will be shorter than for the dust heated by star formation. As a consequence, the positive continuum slope in the L-/M-band that can be observed in the infrared comes from buried AGNs. Observing at this wavelength could bring some information about their activities.

- Finally in the N-band ($7.5-13\ \mu m$), the predominant phenomenon that produces light is the re-emission from cooler dust heated by the star formation. The continuum at this range of wavelength can be a tracer for the star formation activity deeply enshrouded in dust. Some lines can also be observed, such as the [NeII]12.81 μm or PAHs (see Figure 1.5) at very low redshift which also traces the number of massive and young stars.

However, observing in the mid-infrared is also very challenging for ground observatories. First, the low transmission of the atmosphere around Earth in the infrared disturbs the light path and decreases the amount of signal that can be recovered. Second, considering objects as black-bodies, the wavelength's peak of emission only depends on their temperature (the Wien's law, which is $\lambda_{max} \approx 2900\ \mu m.K/T$). A quick computation for the mid-infrared bands indicates that objects with temperatures between −50°C and 700°C have their peaks right inside the mid-infrared band. Thus a strong noise for almost all the objects from our planet. Space instruments are naturally cooled down by their environment and can protect themselves from solar and Earth emissions with thermal shields as for the JWST for example. However, ground-based observatories had to develop ways to remove the noise created by the devices and the sky background.

First, instruments such as METIS are put in cryostats at temperatures below −200°C to prevent the thermal emissions from the instruments. The thermal background emitted by the device and the atmosphere can also be removed with a process called chopping which is performed as follow. For the ELT/METIS, a mirror inside the instrument is moved at high frequency to observe the signal emitted by the sky at adjacent positions of the science object observed. From the signals measured, it is possible to interpolate the signal received at the location of the science object and to remove it (Kitchin, 2014 [40]). These techniques improve significantly the sensitivity of the instrument.

But to reach the diffraction limited resolution provided by the 37-meter diameter of the ELT, an atmospheric compensation device needs to be made. This is what is called the Adaptive Optics. High-resolution becomes crucial when the purpose is to distinguish two objects close together for example. In Figure 1.6, the left side shows what a system without high resolution sees from the two stars system: a massive blob with indistinguishable features. However, increasing the resolution by using Adaptive Optics allows the separate the individual contributions of the two stars, as it is shown on the right side of Figure 1.6.

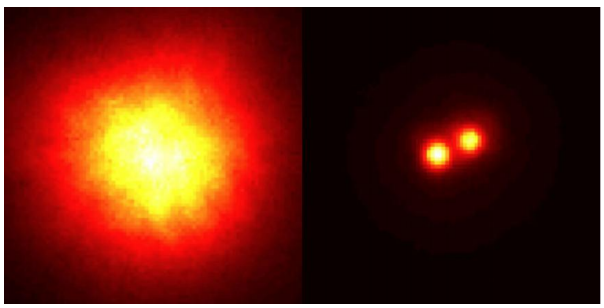

Figure 1.6: The star HIC 59206 with the VLT/CRIRES without (left) and with (right) Adaptive Optics (ESO)

1.3. The Single Conjugate Adaptive Optics for the ELT

The Single Conjugate Adaptive Optics (SCAO) is the simplest form of Adaptive Optics. Figure 1.7 describes its principle for the ELT/METIS.

The atmosphere, by its temperature fluctuations, has no homogeneous optical index. Thus, light rays propagate through this atmosphere at different velocities, which creates optical path differences when they arrive on the telescope's mirror. The wavefront (represented with the horizontal grey lines in Figure 1.7) represents the plane where all the photons emitted from the same source with the same initial phase are located at a given epoch. It is supposed to be flat at the entrance of the Earth atmosphere (no perturbations in space), but the passage through the atmosphere deforms it. This deformation is another representation of the optical path differences between the photons: at a given epoch, because of these thermal fluctuations, some photons have gone through a longer/shorter distance. Which means that their phase is different which is created interference between them. Interference that consequently blurs the image, decreasing the resolution of the instrument considerably.

It is common in AO to use the Fried's parameter r_0 (that depends on the observation wavelength as $r_0 \propto \lambda^{6/5}$) to quantify these perturbations. Often expressed at $0.5\mu m$, it defines the seeing limited resolution θ_{r_0} at a given wavelength: $\theta_{r_0} \sim \lambda / r_0$. Without any atmospheric compensation device, the resolution of a ground-based telescope will be limited to ≈ 0.6" (Tyson, 2010 [77]), no matter the size of the primary aperture of this telescope (see Left in Figure 1.6). The higher the deformation from the atmosphere, the lower the Fried's parameter will be. The idea of the Adaptive Optics is to compensate the phase differences (redress the wavefront) created by the atmosphere so that the resolution of the system can be improved (see Right in Figure 1.6).

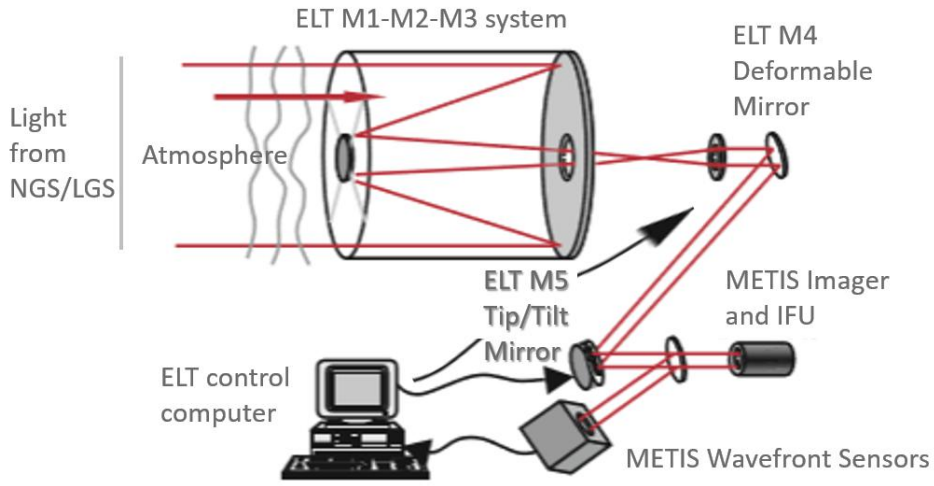

Figure 1.7: The Adaptive Optics principle explained for the ELT/METIS case

To be able to compensate the perturbations created by the atmosphere, the first thing to do is to be able to quantify these perturbations. The idea is to use the light emitted by a "guide," which is an object that must be bright enough to be able to measure the atmospheric properties. In the case of SCAO, the guide is a Natural Guide Star (NGS), most of the time a star or a quasi-stellar object. Thanks to this guide, the atmospheric perturbations can be sensed by the WaveFront Sensor (WFS) that is located inside the METIS instrument. The information is then sent to the ELT control computer that will deform and rotate respectively the M4- and M5-mirror to compensate for the deformations, to minimize them as much as possible. This principle is called the "Phase Conjugation." Let's say that at a given location, some rays of light are slightly in advance compared to others. The mirror will delay them slightly, by locally deforming itself to increase the optical path of those rays. The same principle can also be applied to the opposite situation, where some rays are late compared to others.

It can be noticed that the WFS is located after the deformable mirror M4 and the rotating mirror M5. This has been made so that the perturbations that are measured by the sensors are the residual. The so-called residual is what remains of the optical path differences from the atmospheric perturbations after the M4 and

M5 tried to correct them and corresponds to the redressed wavefront. Ideally, this residual would be equal to zero, where all the atmospheric perturbations on the light path differences would be compensated. But in reality, lots of errors that will be described below prevents that. Nonetheless, the purpose of an Adaptive Optics system is to keep the residual map fluctuations as small as possible. The science instrument of METIS (Imager and IFU) are located at the same location, after the deformable mirror. What the WFS sees is the same as the science instruments.

The atmospheric perturbations evolve with time, with a typical time scale of $\tau_0 \approx 50\ ms$. It means that the AO correction must be done continuously at a high frequency $f_G >> 1/\tau_0$, so that the changes on the mirror are kept "up-to-date" relatively to the atmospheric deformations.

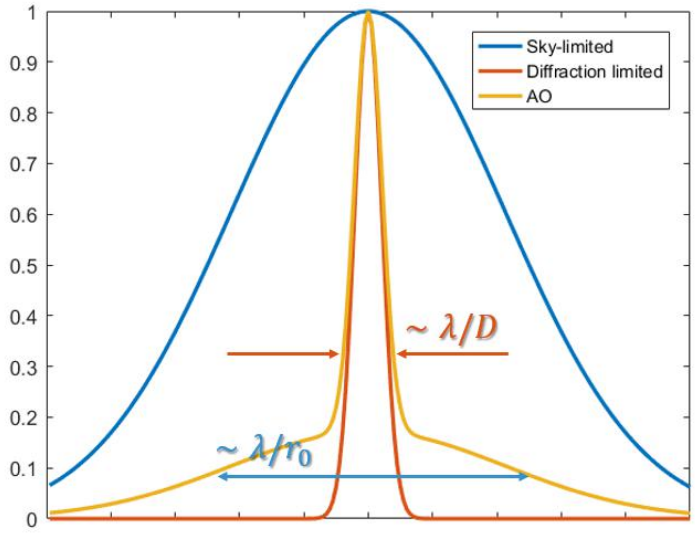

Figure 1.8: Illustration of the PSF obtained without AO correction (sky limited PSF), with AO correction and the ideal case (diffraction limited PSF)

The Strehl ratio is commonly used to assess the performances of an AO system: it is the ratio of the maximums between the Point Spread Function (PSF) obtained with the AO correction and the ideal diffraction limited PSF without atmosphere. The PSF of a system that is unperturbed by the atmosphere looks like the orange curve presented in Figure 1.8: its size depends on the diameter of the primary aperture D (here 37-m for the ELT). As it has been explained before, the larger the telescope, the thinner the PSF. On the contrary, for a system with un-corrected atmospheric perturbations, the PSF looks like the blue one in Figure 1.8. Way larger, the width of the PSF does not depend on the diameter of the aperture anymore. For an uncorrected system, a telescope with a diameter of 1 meter will have the same resolution as the ELT. For a partially corrected system, the PSF looks like the one in yellow in Figure 1.8: the center is corrected with a peak approximately as large as the diffraction limited PSF, while a halo with the width of the sky-limited PSF remains. The individual contributions of these two components (PSF_D and PSF_{r_0}) are linked to the Strehl ratio S by the approximate relation:

$$PSF = S \times PSF_D + (1 - S) \times PSF_{r_0} \tag{1.1}$$

Besides the resolution gain, one fundamental property that appears in this formula is the gain in sensitivity induced by a higher Strehl ratio. Let's say that the noise from instruments and sky background is important enough so that the only thing visible from a star is the central feature of the PSF (the halo is completely drowned into the noise). In that case, having a Strehl twice as important concentrates an emission two times stronger in the peak, which will reduce the integration time to obtain the same image. Having a high Strehl ratio is therefore not only crucial for the resolution performances of the instrument but also to minimize the integration time required when observing faint objects.

The main advantage of using the Strehl as performance criteria is that, under the Marechal approximation (Roddier, 2004 [64]), it is possible to dissociate the individual Strehl losses, and then multiply them together

to obtain the global Strehl ratio. The global Strehl ratio of the system therefore becomes the product of the individual losses:

$$S = S_{WFS} \times S_{fit} \times S_{\tau_0} \times S_{\theta} \times ... \tag{1.2}$$

The reason why it is impossible to make a "perfect" Adaptive Optics system are numerous. But the largest error contributions are mainly caused by (Hickson, 2014 [34]):

The WFS error: Created by the incapacity for the sensors to measure the WF accurately, since they have limited sensitivity. The brighter the guide star, the less critical the error since there will be less noise interference and false measurements. This error is therefore directly linked to the sky coverage of the system: being able to accept fainter NGS (higher magnitudes) will increase the sky coverage of the system, at the cost of a performances decrease. However, there is also a limiting sensitivity due to the internal construction of the sensor. The pupil plane is sampled by the WFS system, each location where the information is retrieved being called the sub-aperture. They have a given space d_s between them, which makes the AO system insensible for variations with spatial frequencies higher than $\approx 1/d_s$. There is a physical cut-off in the spectrum because of the WFS construction. The errors made during the sensing are then propagating along all the AO system, and must, therefore, be minimized in priority.

The fitting error: This is a consequence of the finite actuators number for the compensating part of the telescope's deformable mirror. Therefore, only a limited number of modes are compensated by the mirror. For example, the space between the actuators prevents the system from compensating all the modes. As for the wavefront sensors, modes with a spatial frequency higher than $\approx 1/d_a$ (where d_a is the actuator spacing) are impossible to compensate for the system. For this reason, the highest spatial frequency fluctuations are not corrected by the AO system. It is also important to consider that the correction made by the actuators is not perfect and depends on the geometry of the system with the influence function of the actuators. The mirror must also be static regarding the global AO system dynamics, but this is impossible to realize in reality. The dynamical behavior of the mirror shall then be taken into account and be limited at all cost.

The bandpass error: The system cannot perform the modifications sensed by the WFS at an infinite frequency. It requires some time between operations, mainly the exposure time T_0 for the WFS to gather enough light from the guide star to sense atmospheric perturbations and the system delay due to calculations τ. During this amount of time, the disturbance in the atmosphere will have changed, and the compensation from the system will be slightly maladjusted to the incoming wavefront. The higher the bandwidth (, the faster the system), the less critical this error will be.

The isoplanatism error: The natural guide star might not be in the same direction of the observation, and an angle θ exists between the guide and the object observed. Thus, the turbulences sensed from the bright source are different from the one in the light path of the target. This difference has a direct impact on the performances of the system since the correction provided will be for the atmosphere perturbations crossed by the guide star's light and not the science object light.

The Isoplanatism error becomes hugely problematic in the case of extra-galactic science. When observing exo-planet systems, the guide star is often the bright star companion and high-resolution can be achieved. However, for extra-galactic science, the sources are faint and the probability to find a star bright and close enough to the science object to allow good performances becomes very low. It is estimated that the sky coverage would be less than 10% in the galactic plane and 1% near the poles, which completely jeopardize the high-resolution observations for extra-galactic objects. The reason for this is that the NGS magnitude in the K-band must be below $m_K \approx 11$, which is a crucial constraint (Cantalloube et al., 2017 [18]). This is not compatible with the ELT/METIS extra-galactic expectations, where the high-resolution performances shall be achieved at any location in the sky. That represents the main problem that needs to be solved to create an Adaptive Optics system to perform extra-galactic science correctly.

1.4. The Single Laser Adaptive Optics system

When there is no NGS bright enough near the target, the best solution is to create this guide star artificially. The Laser Guide Star (LGS) is made by shooting a laser in the Earth's atmosphere at 90 km, tuned at 589.5 nm

so that it will excite the sodium atoms located in this layer. When the atoms go from their excited state to their ground state, they will release the surplus energy by emitting photons back to the emitter. This back emission can then be used as a guide star. This solution is already used on the Keck (Wizinowich et al., 2006 [81]) or VLT (Eisenhauer et al., 2003 [24]) telescopes (see also Figure 1.9a), and allows to use the AO system on a much larger portion of the sky.

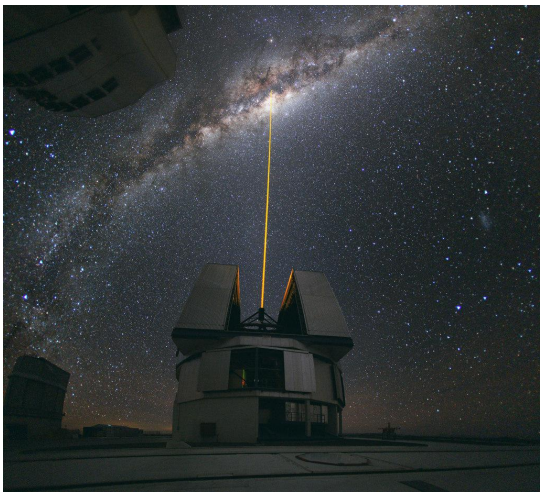

(a) The VLT Laser Guide Star system (ESO)

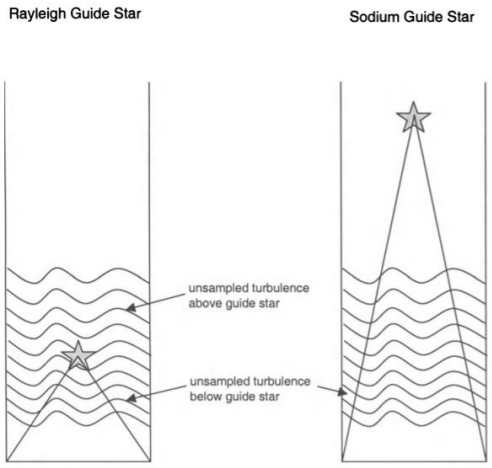

(b) The cone effect for Rayleigh and Sodium guide stars (Davies and Kasper, 2012 [21])

Figure 1.9: Principle error sources for the SLAO, and its implementation on the VLT

However, due to the nature of the guide star, some additional errors need to be taken into account compared to a "standard AO" (Hickson, 2014 [34]):

The cone effect: This effect is predominant in the case of SLAO since the guide star does not come from an infinite distance as it was the case for Single Conjugated Adaptive Optics but from a sodium excited layer at a finite distance. Therefore, a part of the turbulence is not sensed by the WFS since it is not even crossed by the light, which generates an imperfect correction. This imperfect correction results in an additional error called the Focus Anisoplanatism. This is the reason why Rayleigh guide stars are not used (cf Figure 1.9b) in the ELT system since the star would be created in the low-atmosphere and will thus limit considerably the amount of perturbation sensed. The principle of the Rayleigh guide stars was to use the energy back-scattered by the atmospheric molecules at any wavelength. Since no requirements on the wavelength are made, this is much easier to build powerful lasers that can create much important energy. However, the focus anisoplanatism discussed just before becomes so important that this solution is for the moment not operational. New systems such as Laser Tomography AO (LTAO) or Multi-Conjugate AO (MCAO) are recommended for ELT class telescopes to tackle this issue: using several guide stars, it is possible to reconstruct the global atmospheric perturbation from the measurements, and thus restrain the cone effect impact. However, these solutions are complicated to implement (Fusco, 2010 [28]) and the project for a global LTAO system for the ELT has been abandoned.

Beam elongation error: The beam created by the excited sodium layer is elongated since this layer has a thickness of about 10 km. Therefore, the LGS is not a point for the detector but rather an elongated object. This is even truer because the laser is launched from the Laser Launcher Telescope (LLT) located at a distance of 18.5 meter from the ELT center. According to Schreiber et al., 2009 [69], this problem must be considered very seriously for the conception of LGS WFSs on the ELT, using large FoV > 10" to limit the truncation of the spot. This problem is also linked to the Rayleigh scattering from the atmosphere, which is diffraction of the light from the laser and the LGS by the lower layers of the atmosphere. This scattering must be suppressed from the image so that it does not create any interference.

Furthermore, some additional problems created by the use of the LGS appear for the WF sensing. To understand these problems, it is essential to define the concept of modes in AO. It is common to decompose the perturbations from the atmosphere into polynomial modes, called the Zernike modes. These modes have

individual spatial and temporal dynamics: the low-order modes have less important temporal and spatial frequencies, while the high-order ones evolve faster with high spatial frequencies. Figure 1.10 represents the modal decomposition for the first order modes: the lower you go in the Figure, the higher the order of the modes. A global atmospheric distortion created by the atmosphere can be expressed as a sum of Zernike modes, as a Fourier modal decomposition can be used to describe a periodic signal.

The Piston (the lowest order mode, top of the Figure 1.10) is a global path difference applied to all the photons, so it does not create an additional path difference between them. It cannot be detected by the sensors since it is not introducing any local slope, but it has thus no effect on the global performances. The low order modes are named Tip and Tilt (TT, vertical and horizontal tilt in Figure 1.10) and correspond to a global slope of the wavefront in a direction. In the ELT/METIS case, the tip/tilt modes will be corrected by the tilted ELT's M5-mirror: they do not require any deformation of the mirror, only a global tilt in a direction. On the contrary, correcting the high-order modes will need to apply path difference locally, and will thus require a deformable mirror (see the shape of the high-order modes in Figure 1.10). The M4-mirror of the ELT will take care of this part. The reason behind the separation of the low and high-order correction devices lies in the amplitude required to correct the Tip/Tilt: it is often way more important than the one needed for the higher order modes. Thus, separating the correction devices into two components restrain the constraints on the M4-mirror amplitude.

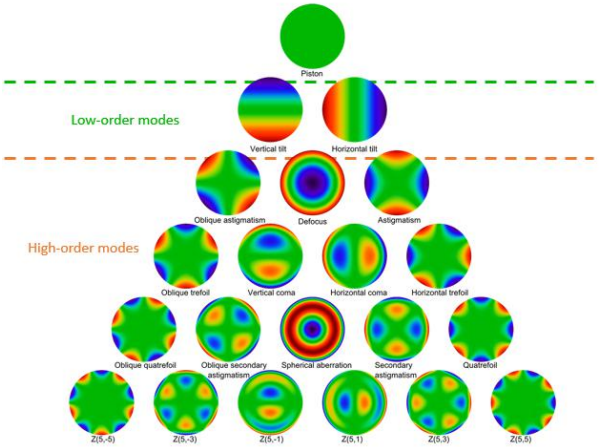

Figure 1.10: The Zernike Modes, arranged from the lower order one (top) to the highest one (bottom) (MathWorks)

The problem with using a LGS is that the Tip/Tilt is not sensed by the WFS, because the perturbations from the atmosphere are applied to both the up-link and downlink path of the laser. Thus, no tilt can be detected because there is no Tilt applied to the wavefront of the LGS light. Moreover, the sodium layer density distribution slowly evolves with time, which makes the WFS not focused on the guide star anymore. The system will try to compensate for this, interpreting this defocus as an atmospheric perturbation. Has a consequence a blurring of the science image.

Finally, spot truncation also has an impact on the WFS measurements, creating offsets. Has it can be seen on Figure 1.11, the field of view of the WFS (represented in green) is not big enough to completely include the LGS beam for a telescope such as the ELT. As it will be developed in Chapter 3, this creates some offset for the correction, as the LGS sensor is not able to accurately sense the atmosphere because of the loss of information induced by this truncation. These offsets can be observed in the LGS residual map of Figure 3: the color coding represents the intensity of the phase difference, dark blue being the reference and yellow the maximum difference. The pattern observed represent an optical path difference, created by the incomplete sensing of the system by the LGS WFS. As it has been shown before, a residual with important path differences will create a larger PSF (see Figure 1.12d), thus a lower resolution system.

To prevent these effects, a NGS is still required and used as a reference, for what is called the Truth Sensing. Since it is not biased by these elongation effects, the NGS WFS will be able to see and correct the residuals created by the LGS sensing, increasing the performances. Figure 1.11 shows that after the residual correction, the color of the residual is much more uniform: the phase difference of the wavefront is globally the same at any location. And it can be seen that the PSF also became more compact (see Figure 1.12c). The term "truth

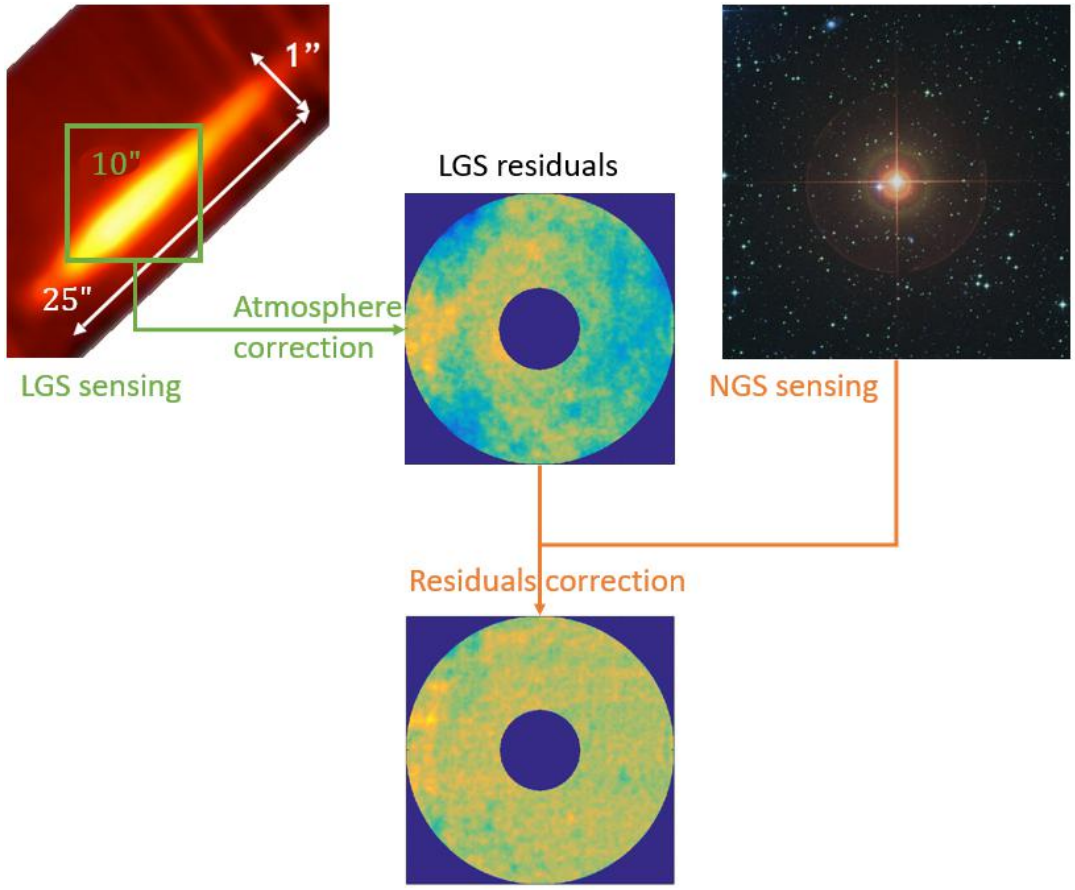

Figure 1.11: Illustration of the working principle of a SLAO system, with the Laser Guide Star in green and the Natural Guide Star in orange.

sensing" comes from the fact that the NGS sensor will see the same atmospheric perturbations as the one in the science object path, without being influenced by the focus anisoplanatism effect or the beam elongation. Since the residuals are a consequence of the incorrect sensing of the LGS WFS and not the atmospheric variations, there is no need to run them at a frequency $f_G >> 1/\tau_0$ or to use a high spatial resolution configuration as it is the case for the SCAO system: the constraints on the NGS magnitude are less important than for SCAO which will still allow a high sky coverage. This will be further developed in chapter 4 and chapter 8.

1.5. The SLAO system for the ELT/METIS

The goal of this Master Thesis is to design a working solution for the ELT/METIS SLAO system. It has been shown before that a SCAO system is not enough to compensate for atmospheric perturbations with a 100% sky coverage, because the level of constraints on the NGS magnitude is critical. As it has been explained, using a LGS could be the solution to avoid this limitation but will create additional complications. The thesis work will be used as a proof that a SLAO system is viable: a good Strehl ratio performances for a minimum cost, weight, and system complexity with a sky coverage of 100%. Precise requirements can't be put on the Strehl ratio, as there is for the moment no official request from ESO about this system.

The first thing to design is a solution to split the science beam from the LGS beam. The purpose here is to recover the information from both while minimizing the impact on the global system performances. Chapter 2 will explain the design that is currently foreseen for this beam splitter. Two possible solutions will be developed, with their advantages/disadvantages. Once the LGS beam recovered, the atmospheric perturbations need to be sensed. This problem will be developed more in details in Chapter 3. In this part, it will be explained how the beam elongation could be taken care of and what are the main consequences of the sodium layer variations on the Strehl performances of the system. The implementation of the LGS WFS will

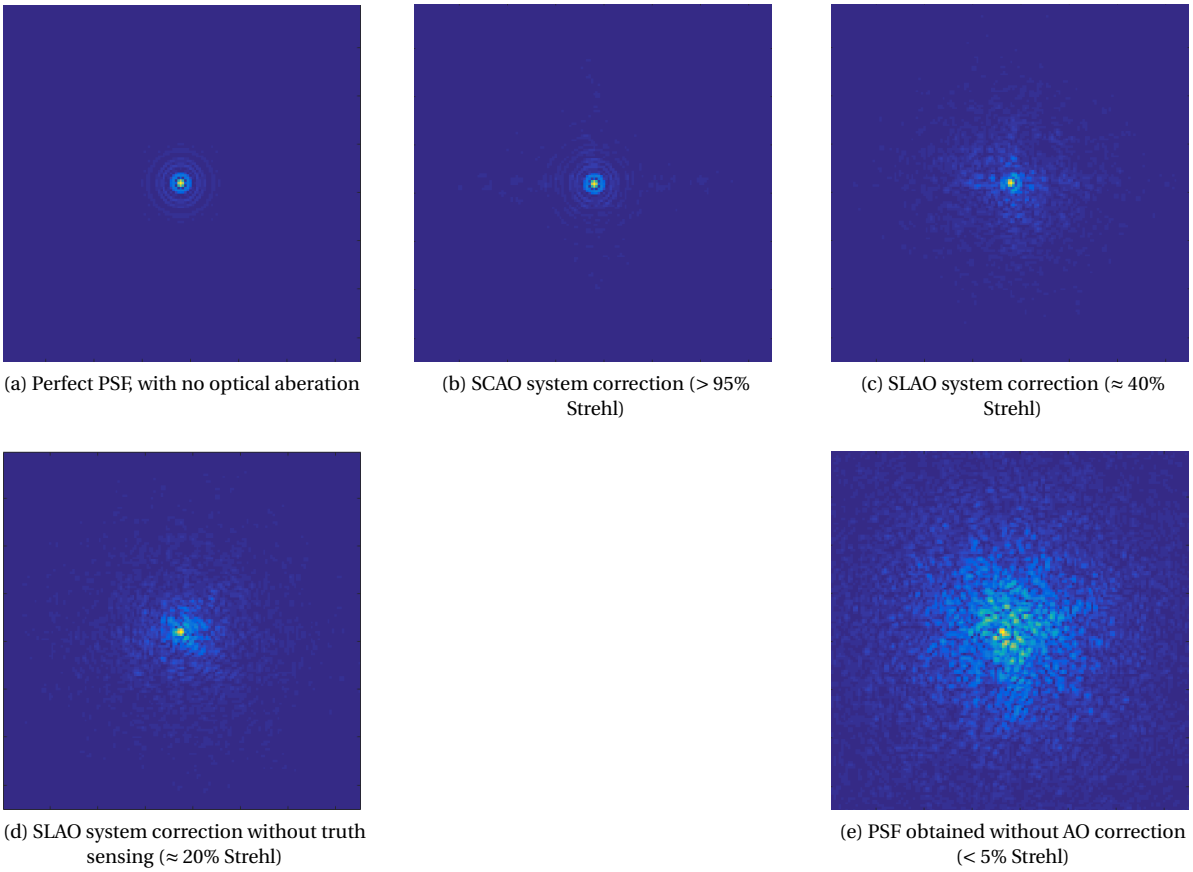

(a) Perfect PSF, with no optical aberation

(b) SCAO system correction (> 95% Strehl)

(c) SLAO system correction (≈ 40% Strehl)

(d) SLAO system correction without truth sensing (≈ 20% Strehl)

(e) PSF obtained without AO correction (< 5% Strehl)

Figure 1.12: Illustration of the Adaptive Optics correction on the aspect of the PSF, for Armazones atmospheric conditions.

leave some problems that cannot be only corrected by a so-called "truth sensor". Chapter 4 will detail the design of the low-order WFS that will be used for the truth and tip/tilt sensing. This chapter will present the simulator that has been made in MATLAB to correct the residual patterns created by the LGS WFS. The end of this part will provide constraints on the magnitude required from the NGS to apply these corrections. Chapter 5 will simulate the Strehl performances of the system, and look into the parameter space to find the best compromise between high Strehl performances and high sky coverage. It will present the simulation tools that have been used, in addition to a comparison between the performances obtained during the project and by ESO. Once the properties of the system defined, the WFS and the focus designed paired to it will be implemented in ZEMAX in Chapter 6. A realistic design will be presented, in addition to a first estimation of the cost, weight, and size required for this design to work. This part will be followed by a mechanical design draft in Chapter 7, where a first idea will be developed to show how the lenses used in the previous chapter could be hanged and the moving parts translated. Finally, the calculation of the sky coverage will be done in chapter 8. This part will include the process to estimate the sky coverage, in addition to a detailed analysis of the optimal wavelength that should be taken to optimize it. The final product of this part will be a graph with the expected performances for the METIS AO system, regarding the requirements on the NGS magnitude. The thesis will then be concluded in Chapter 8.2, summarizing the work that has been performed during this 7 months project.

In the Appendices, the Chapters A, B and C will present the work that has been performed at CEA-Saclay during a previous internship, dealing with the science that could be achieved with the ELT/METIS instrument. Although this part has not been conducted during the Master Project, it could be interesting for people that have astrophysical knowledge to have an idea of the ELT/METIS use.

Chapter 2

Investigation of focal plane options

The beam splitter will be used to separate the light contributions emitted by the Laser Guide Star and the science target in the instrument's focal plane. The light from the guide star, emitted at 589 nm (Na-D line) needs to be directed towards the high-order wavefront sensors while the science beam must be directed toward the instruments inside the cryostat. The beam splitter must be made so that there is no truncation for the science beam to keep high sensitivity performance while recovering the entire LGS beam for the high-resolution performances.

Contents

2.1. Presentation of the problem

2.1.1. The Anisoplanatism effect

The system is different from the LTAO system, where none of the LGS are located on the science target. Here, the LGS footprint will be directly located on the science object. There are several reasons for that. The first one is the anisoplanatism effect: this effect is the consequence of a miss-alignment between the science target and the guide source. The turbulences crossed by the science beam are thus slightly different than the ones crossed by the guide star beam, which has a consequence an AO system compensation not completely adapted to the incoming perturbed wavefront. Assuming the Marechal approximation and a Kolmogorov model of perturbations, the Strehl loss created by this effect can be written as (Hickson, 2014 [34]):

$$S_\theta = e^{-(\theta/\theta_0)^{5/3}} \tag{2.1}$$

with $\theta_0 = 0.314 \times r_0 \cos\gamma / \bar{h}$ being the anisoplanatism angle. Here r_0 represents the Fried's parameter defined in the introduction, $\bar{h}$ a physical constant depending on the atmospheric perturbations distribution and γ the zenith angle. It is equal to ≈ 32" in the L-band and ≈ 105" in the N-band at the zenith angle of 30°. For $\theta = \theta_0$, the Strehl becomes equal to $S_\theta = 37\%$. The Figure 2.1 represents the Strehl loss created by this effect in the L-band and N-band.

As it can be seen on the Figure 2.1, placing the LGS at the edge of the FoV will generate a critical loss of Strehl ratio in the L-band, in the order of $S_\theta = 0.65$. The effect is not present in the N-band when the loss

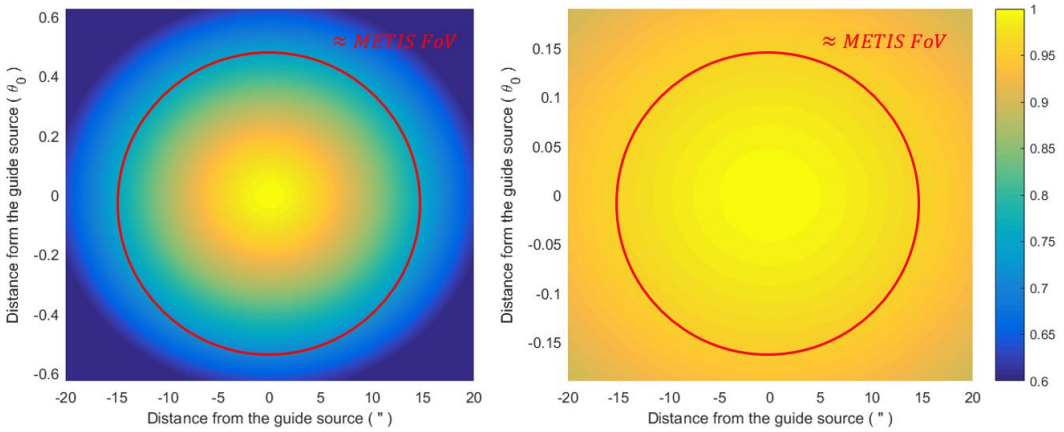

Figure 2.1: The spatial distribution of the Strehl ratio influenced by the Anisoplanatism effect in the L- (right) and N-band (left)

will be at the maximum of ≈ 95%. In any case, this effect should be limited as much as possible to optimize the performances. The second reason is that putting the LGS outside the METIS FoV will require to have a larger FoV at the entrance of the instrument. Having larger FoV means that all the optics must have a more important diameter, which can generate losses and more complexity since the design of the system has to be re-thought. To keep the system compact and straightforward, the science and LGS beams are thus on the same axis.

The consequence of this solution is that a global beam containing the science and LGS beams will both enter inside the instrument, where a system needs to separate the individual contributions to send them respectively to the imager and IFU and the WFS.

2.1.2. The LGS focal point

The SLAO system uses a guide star at a finite distance, while the telescope has its focus made for a light source coming from an "infinite" distance. The Figure 2.2 illustrates the problem: the light coming from the LGS, in green, will focus at a larger distance than the light coming from the science object in red. The black double arrow represents the ELT system, assimilated here as a paraxial lens.

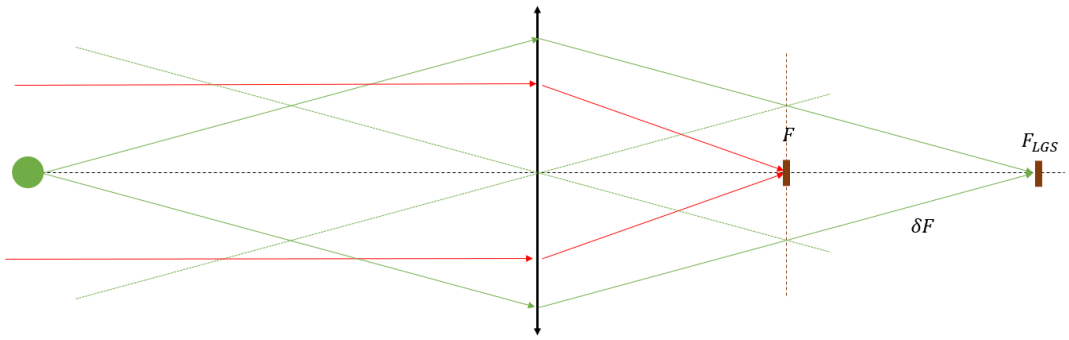

Figure 2.2: Illustration of the focus problem for an SLAO system

The distance between the LGS focus and the telescope focus changes relatively to the distance between the sodium layer and the telescope. To be able to observe a sizable percentage of the sky, the zenith angle of the telescope will vary between 0 and 60°. Which therefore changes the distance between the telescope and the layer. This distance can be easily computed as:

$$d_{LGS} = \frac{z_{LGS}}{\cos\zeta} \tag{2.2}$$

where $z_{LGS} \approx 90\ km$ is the sodium layer altitude and ζ is the zenith angle. The height and width of this sodium layer can vary with daily scales (Pfrommer et al., 2009 [58]) and year scales (Lewis C. et al., 2007 [47]). Although

these variations induce minimum effects compared to changes in zenith angles, they also need to be taken into account by the system.

Assimilating the telescope to a lens with a focal length of $f_0 = 17.48 \times D \approx 687\ m$, it is possible to calculate the distance at which the focus will be made for a LGS at a given zenith angle. Using the basic relation of optic, the focal distance for the laser guide star can be obtained:

$$F_{LGS} = \frac{1}{\frac{1}{f_0} - \frac{1}{d_{LGS}}} \tag{2.3}$$

From F_{LGS} (the focal point of the LGS) and its difference $\Delta F = F_{LGS} - f_0$, by applying the Thales theorem, it is possible to compute the obscuration size for the laser guide star at a given distance Δx from the focus point of the telescope (see Figure 2.3). This obscuration represents the image of the pupil on the LGS beam and will be unused by the system. The pupil shape is created because of the light that cannot enter the telescope since it is blocked by the central-obscuration of the telescope, made by the tower sustaining the M3, M4, and M5 mirrors and the M2-mirror itself.

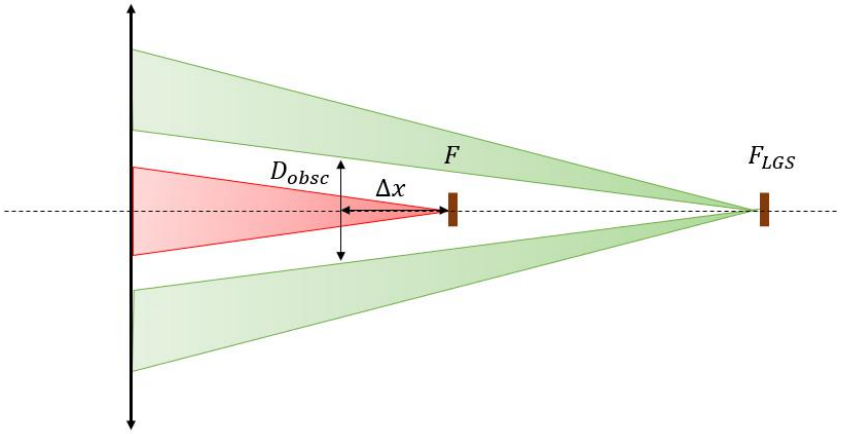

Figure 2.3: The obscuration of the telescope with the science beam (red) and the LGS beam (green)

Now that the layout of the problem has been presented, the possible solutions to split the beam are going to be detailed.

2.2. The dichroic solution

The first solution is to split the beam by using an optic that behaves differently relatively to the wavelength of the incoming beam. The LGS-WFS wavelength range is entirely different from the one for the science instruments: the light for the WFS is concentrated around the sodium emission ($\approx 0.589\ \mu m$) while the science beam (that might also contain the NGS) use the infrared bands ($\approx 2-20\ \mu m$). The dichroic used here would let the infrared wavelength (in the K-band for the low-order AO system and the L- and M-band for observations) go through it, while the optical wavelength from the LGS will be reflected and send toward the WFS.

One problem with this solution is that the dichroic will have to be placed outside the cryostat, and will, therefore, be (relatively) warm. For this reason, the science beam that will go through the dichroic will be considerably influenced by this. The thermal emissions emitted will add lots of noise, decreasing by several order of magnitudes the sensitivity of the instrument. Thus, such a solution could jeopardize the possibility of N-band observations at high resolution.

Another thing that needs to be taken into account is the slight defocus that will be created by the dichroic. Even though the rays will go through it without reflection, the change in the index will generate refraction that will modify the propagation speed of the rays. Therefore, a system with and without dichroic will not have the same focal point. An optical system must be put after the beam splitter to compensate for it. Moreover, since the dichroic is tilted, the optical axis of the system will also be different.

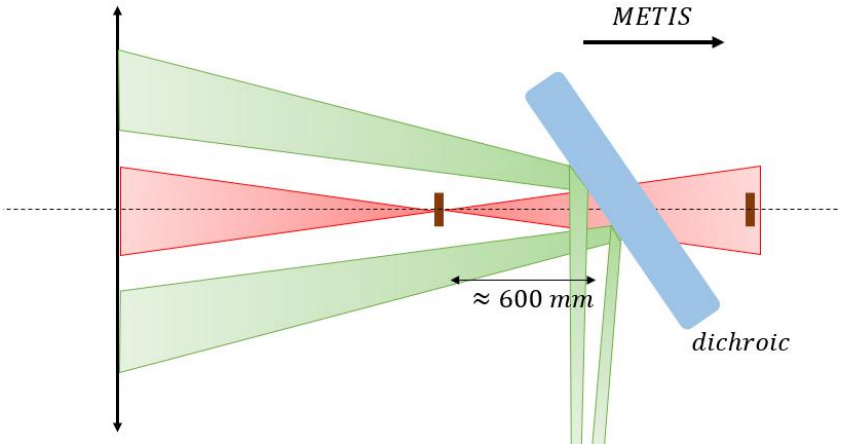

Figure 2.4: The obscuration of the telescope with the science beam (red) and the LGS beam (green)

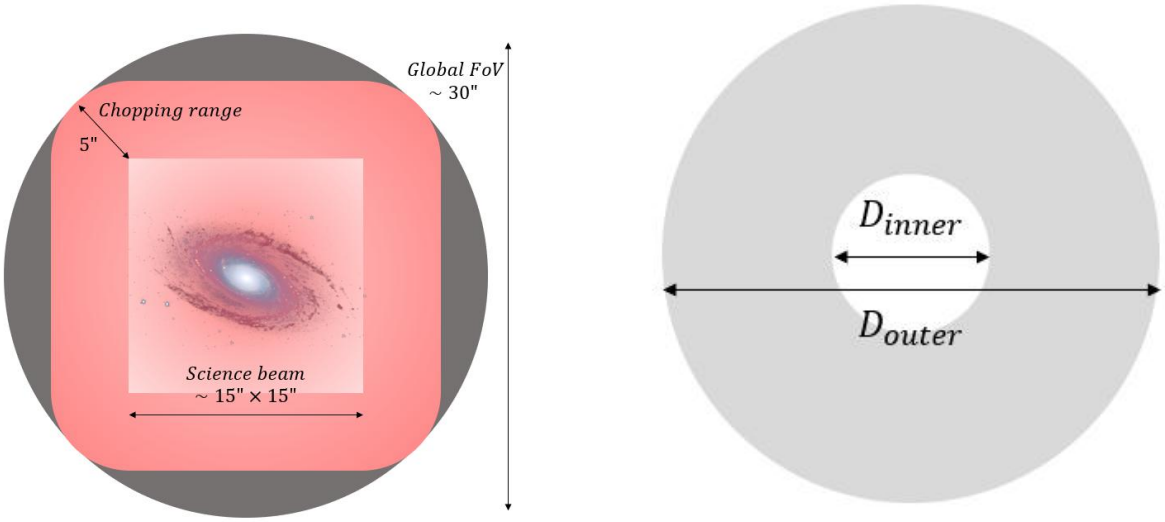

(a) The ELT/METIS science beam and field of view

(b) The annular mirror

Figure 2.5: The annular mirror solution, and the constraints on its inner diameter.

The actual idea for the dichroic would be to add it to the existing chariot, with the hole and the mirror that direct the ray from the Warm Calibration Unit to the METIS instrument. As it can be seen in Figure 2.4, it shall be placed 600 mm after the focal point of the telescope, to reduce the impact of dust on the surface of the dichroic. If the mirror is not at the focal point, the dust located at on the external surface of the mirror will have less impact on the final image. However, this can also be difficult for stability purposes, as the chariot will already hold the mirror for the warm calibration unit.

This solution seems to be very problematic for the system, by the complexity it adds to the system but also the risk for the N-band observations. Another solution needs to be found.

2.3. The annular mirror solution

2.3.1. Principle of the solution

This other solution could be to put an annular mirror at the focal point of the system. The idea here is to use the difference of focus between the science beam and the LGS one, due to the finite distance of the LGS. The conditions for this annular mirror to work are presented in the Figure 2.6: the inner diameter has to be large

enough not to reflect the science beam, but small enough to take all the light coming from the LGS. The idea here is to adapt the inner diameter of this mirror so that it is more or less the obscuration diameter at the mirror location.

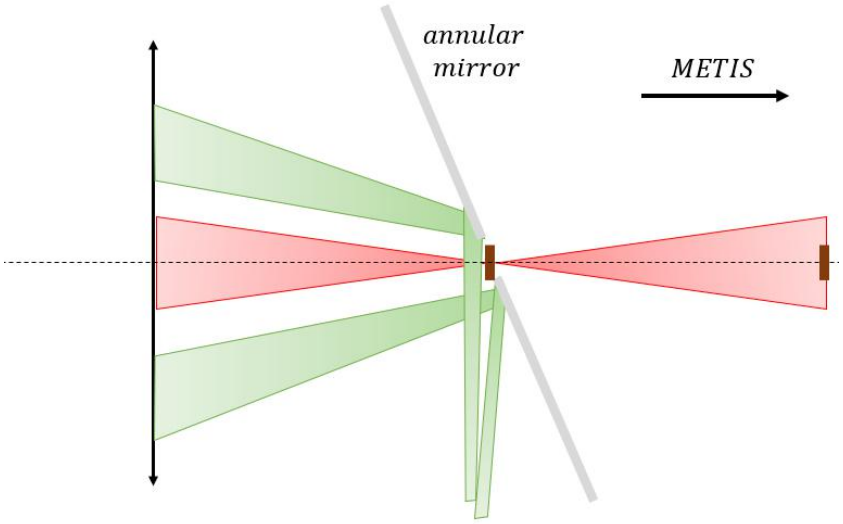

Figure 2.6: The schema for the second solution: the annular mirror

A trade-off has to be made to adapt the size of the mirror:

- On one hand, the larger the inner diameter will be, the less interference with the science beam. The heat generated by the mirror, which impacts the performances for MIR observations, needs to be corrected. Furthermore, if the inner diameter becomes bigger than the obscuration diameter, the mirror loses a part of the information coming from the LGS, which means that the wavefront will not be measured there. Has a consequence a loss in the performances for an AO system.
- On the other hand, the smaller the inner diameter, the higher the AO performances. However, if this diameter becomes too small, it might reflect a part of the light coming from the science beam; the outer portion of the science beam being mandatory for the chopping of the instrument. Having a less important beam means that the chopping cannot be made as efficiently, and the background subtraction necessary in the MIR might be jeopardized. The other possibility for such a system would be a smaller science beam, which could become a problem for some observations. However, the majority of the observations that would be conducted with the SLAO system would be extra-galactic ones, where the target is most of the time few arcseconds large. Thus, the FoV required will not be too important.
- However, one last thing to take into account is that the SLAO system will require a Natural Guide Star in its FoV (see Chapter 4). Thus, the science FoV has to remain as large as possible to increase the sky coverage of the system.

2.3.2. Calculation of the optimal inner diameter for the mirror

To calculate the optimal inner diameter of the system, the size of the science beam and the obscuration diameter around the focus point of the telescope needs to be known. The problem here is that since the obscuration diameter changes in an inversely proportional way relatively to the zenith angle, an optimal configuration of the inner diameter at the zenith might not be optimal at $\zeta = 60°$. The Table 2.1 represents the variations of several parameters relatively to the zenith angle, and how they affect the obscuration diameter. The point is here to evaluate the width of the science beam and the obscuration size at the focal point of the telescope. The science beam is as small as possible. It can be approximated that the footprint of the science beam at a distance Δx from the focus point F will be, for an optical system with an f-number of f:

$$D(\Delta x) \approx D_F + \frac{\Delta x}{f} \tag{2.4}$$

For the LGS obscuration size, a simple Thales law allows to express it as:

$$D_{obsc}(\Delta x) = D_{pupil} \times \frac{\Delta F - \Delta x}{F_{LGS}} \tag{2.5}$$

Here ΔF represents the distance between the focus point of the telescope and the focus point for the LGS.

Table 2.1: Obscuration size for different zenith angles

ζ (deg)	d_{LGS} (km)	F_{LGS} (m)	ΔF (mm)	D_{obsc} @ focus (mm)
0	90.0	692.2	5 283.9	84.7
5	90.3	692.2	5 263.6	84.4
10	91.4	692.2	5 203.1	83.4
15	93.2	692.1	5 102.7	81.8
20	95.8	691.9	4 963.2	79.6
25	99.3	691.7	4 785.9	76.8
30	103.9	691.5	4 572.0	73.4
35	109.8	691.3	4 323.2	69.4
40	117.5	691.0	4 041.6	64.9
45	127.3	690.7	3 729.4	59.9
50	140	690.4	3 388.9	54.5
55	156.9	690.0	3 022.9	48.6
60	180.0	689.6	2 634.2	42.4

Assuming a constant plate scale of 3.31 $mm/"$ at the focus point of the telescope but also at ±1% of it, the physical diameter of the science beam is $D_{sc} \approx 100\ mm$ for a Field of View (FoV) of 30" at the focus point, and $\approx 134\ mm$ at 600 mm from the focus point. From the Table 2.1, it can be noticed that even at zenith angle the science beam is larger than the obscuration size.

However, the science beam does not contain only the science information. As it can be seen in Figure 2.5a, there is also the chopping zone. The Table 2.2 represents the size of the science beam for different configurations at 600 mm from the focus point. These values can be compared to the ones given in Table 2.1.

Table 2.2: Science Field of View dimensions for different configurations

Mode	FoV (")	FoV @ 600 mm (mm)
L-band	14.0	80.7
L-band 2.5" chopping	24.8	116.4
L-band 5" chopping	29.8	133.0
N-band	10.0	67.4
N-band 2.5" chopping	19.1	97.5
N-band 5" chopping	24.1	114.1

The Figure 2.7 represents the difference between the obscuration beam diameter and the science beam diameter at the focal length, a function of the FoV considered for the science beam. When this value is positive, it means that the annular mirror can be placed directly in the focal point, reflecting the LGS beam and leaving the science beam alone. However, if this value becomes negative, it means that the science beam needs to be cropped for reflecting the entire LGS beam. At the bottom, the bands represent the normal FoV of the METIS instrument presented in Table 2.2. If for example the annular mirror is used up to a zenith angle of 60°, the science beam has to be truncated to 5", with a chopping throw of only ≈ 2.5" in each direction. This corresponds to a global FoV of ≈ 13", which directly translates to an inner diameter for the mirror of 42.9 mm. However, if the observations are made up to a zenith angle of 30°, science FoV of 7" could be used, even with a full chopping range.

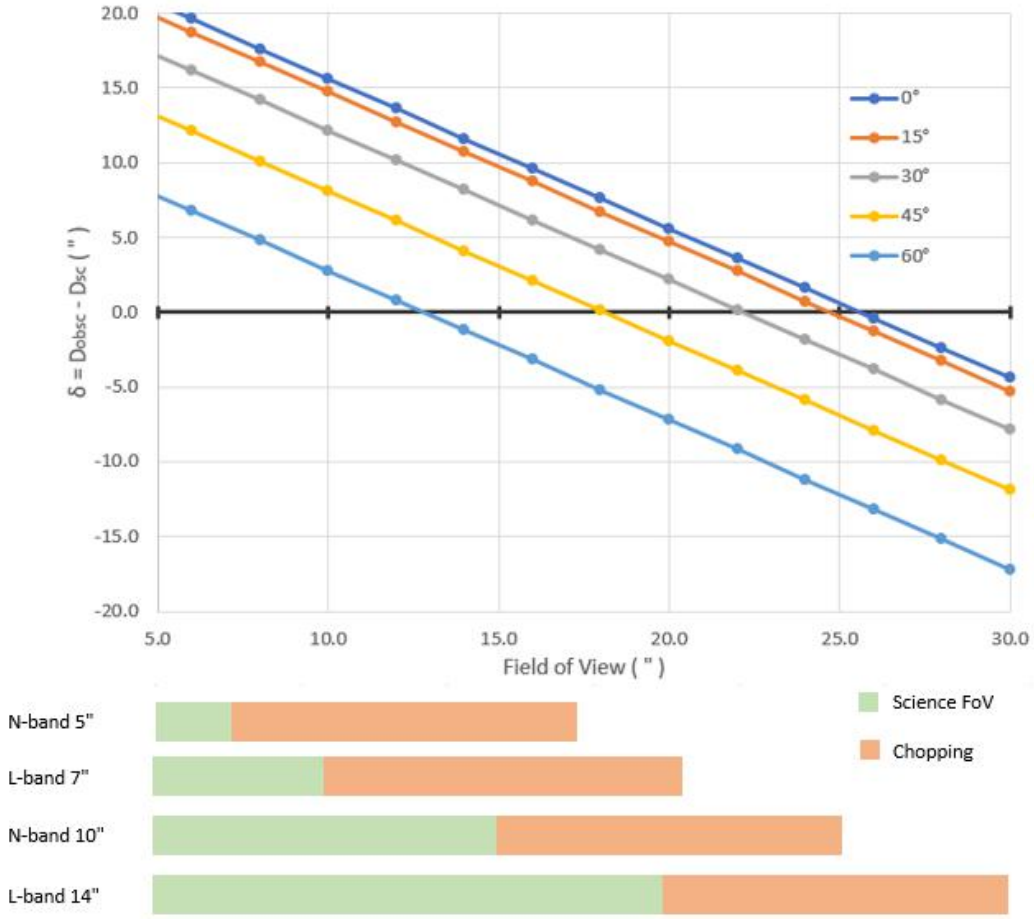

Figure 2.7: Difference between the obscuration diameter D_{obsc} and the science beam diameter D_{sc} at the ELT focal point VS Field of View of the science beam, for several zenith angles. The bands at the bottom of the image represents the FoV taken for a given configuration.

Conclusion

Both solutions have their advantages and disadvantages. The annular mirror, contrary to the dichroic, would still allow N-band observations at the expense of a smaller science FoV. It also does not require a re-focus system, and this solution is therefore much easier to implement. However, the emission from the edges of the mirror directly in the focal plane needs to be taken care of by a field stop so that they do not interfere with the observations. Furthermore, a compromise has to be looked at carefully by the scientist for the inner diameter of the mirror so that the optimum solution for science and performances can be found.

Chapter 3

Preliminary investigation of the High-order Wavefront Sensor

The design of the high-order WFS will be explained further in details into this chapter. This sensor will observe the LGS created in the sodium layer to infer the perturbations generated by the atmosphere. The disturbances will be re-constructed and then sent to the control computer of the ELT to deform the mirror to compensate for them. Here, the high-order refers to all the perturbations that can be sensed by the LGS WFS, except the Tip/Tilt that cannot be detected by a LGS and the truth sensing that will be developed in the Chapter 4.

Contents

3.1. The Shack-Hartman Wavefront Sensor

The current solution decided for the high-order WFS is a Shack-Hartman wavefront sensor. The main reason is that these sensors are already well-known and used in many SLAO solutions (La Penna et al., 2014 [42]), and thus are cheaper and simpler to implement. The cost of this choice is a slight decrease in the performances for low luminosity stars (Bertram, 2017 [8]), which will not be the case for a LGS. Moreover, the MAORY sensor used for another instrument of the ELT using LGS will also be a SH-WFS (Diolaiti et al., 2016 [23]). This sensor is based on a principle that is similar to the Pyramid Wave Front Sensor(see Chapter 4), except that the sampling is done in the pupil plane and the measurements in the image plane. The purpose of the SH-WFS is to measure the local slope of a wavefront created by atmospheric perturbations by analyzing the displacement of the figure on detectors put in the image plane.

Figure 3.1a shows the schematic principle of this WFS, and Figure 3.1b shows an example of detector. A lenslet array is used to subdivide the pupil plane into sub-apertures. Each lens in the lenslet array produces an image of what the telescope observes, the LGS. This image is projected on detectors where the slope will be measured by comparing the relative intensities on the pixels. For example, on the detector represented on Figure 3.1b, the slopes in the X- and Y-direction will be computed as:

$$S_X = \frac{I_2 + I_4 - I_1 - I_3}{I_{tot}} \tag{3.1}$$

$$S_Y = \frac{I_1 + I_2 - I_3 - I_4}{I_{tot}} \tag{3.2}$$

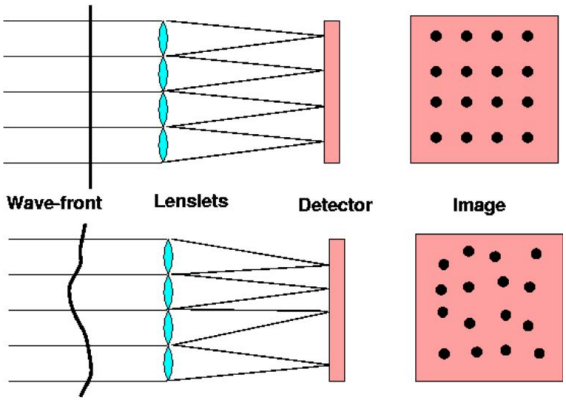

(a) The Shack-Hartmann wavefront sensor with a non-perturbated signal (up) and a perturbated signal (down)

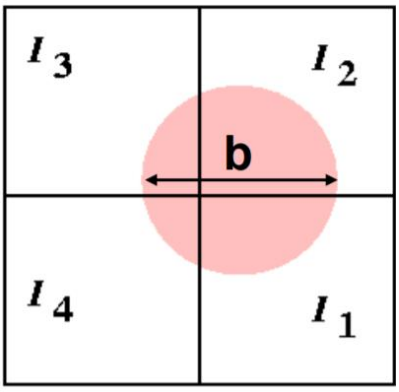

(b) The pixel array detector, here a bi-cell

Figure 3.1: The principle of the Shack-Hartman wavefront sensor (Tyson and Frazier, 2012 [78])

where $I_{tot} = I_1 + I_2 + I_3 + I_4$. When no perturbation is made by the atmosphere (the wavefront is flat), the beam is supposed to be located in the middle of the detector array. The resulting intensity difference is then equal to 0. However, when the wavefront is distorted, the spot will be slightly translated by an amount directly proportional to the local slope of the wavefront.

From these slopes, it is then possible to reconstruct the complete wavefront error by processes such as the CURED algorithm. The implementation of the algorithm will be explained more in details in Chapter 4. Once the wavefront reconstructs, the actuators of the M4 ELT's mirror can be translated to apply the principle of phase conjugation.

3.2. The Laser Guide Star elongation and Spot truncation problem

As it has been seen before, the SH-WFS is a technology that is mature and ready to be used. However, its use with the SLAO system for the ELT/METIS adds additional problems that have never been encountered in the previous applications on the VLT for example. The major stake for the design of high-order wavefront sensor is to take care of the spot elongation of the laser. Thus, instead of a point source as it is the case for a Natural Guide Star, the LGS will be an elongated source, as it can be seen in Figure 3.2a. The elongation has direct consequences on the slope computations. For example, in the parallel direction of the LGS spot, the slopes cannot be computed as precisely as for points since the intensity is more homogeneously distributed. The signal is also more scattered, which makes it more difficult when noise becomes too important since the signal to noise ratio per pixel will decrease. Finally, truncating a part of the obtained spot can have disastrous consequences for the computation of the slopes, since a part of the information is not available for the centroiding algorithm. This can lead to the appearance of patterns observed in the wavefront's residual (see Figure 3.2c). The factors that influence the spot elongation are numerous:

- First, the Laser Launcher Telescope (LLT) is located on the size of the telescope, which means that the distance between the center of the aperture and the LLT is 18.5 m compared to the 4 m for a VLT. The further away from the LLT, the more important the elongation effects. The relation between the effective elongation in the sky and the location of the LLT can be written:

$$\epsilon = \frac{d \times \Delta z}{z_{LGS}^2} \approx 0.24" \times d\ [m] \tag{3.3}$$

  Which gives an elongation of ≈ 5" for the ELT, compared to the ≈ 1" for the VLT.

- Second, since the diameter of the ELT is larger than the VLT one, the sub-apertures located at the opposite side of the LLT see a much more extended LGS than the ones found at a closer distance (see Figure 3.2b). The sensors on the opposite direction of the LLT cannot sense the wavefront as well as the one located close to it, because the elongation becomes much more critical. And this absence of determination leads to a substantial decrease in the Strehl ratio.

- The atmosphere thickness creates a spot elongation on the WFS because it is a 2D-projection of the excited column of the sodium layer. The sodium column density profile assumed in most simulations is similar to a Gaussian, but a profile with two local maximums, for example, could have very damaging consequences for the Strehl. Based on (Blanco, 2017 [9]), the Strehl performances in the K-band can decrease as much as 30% between ideal and worst conditions for the same configuration of the SLAO instrument.

It could be inferred that the zenith angle has an impact on the spot elongation since it increases the length of the path Δz for the beam through the sodium layer: $\Delta z(\zeta) = \Delta z_0 / \sin\zeta$. On the one hand, $s \propto 1/\sin\zeta$. However, considering that the atmosphere layer is further away when increasing the zenith angle $d(\zeta) = d_0/\sin\zeta$ (with $d_0 = 90\ km$) and having the size of the beam $s \propto 1/d(\zeta)$, there is also $s \propto \sin\zeta$: the global size of the beam also shrinks by the same amount. Thus, the elongation can be assumed independent from the zenith angle: $s \propto cte(\zeta)$. However, the distance of the sodium layer increases with the zenith angle, which means that the photon flux received is less important.

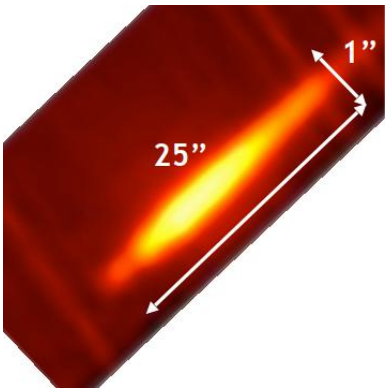

(a) Spot elongation picture, with the main dimensions (Schreiber et al., 2009 [69])

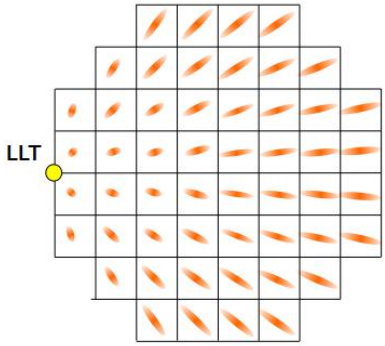

(b) Distribution of the elongation relatively to the Laser Launcher Telescope, located on the right part of the telescope (Pfrommer and Hickson, 2014 [57])

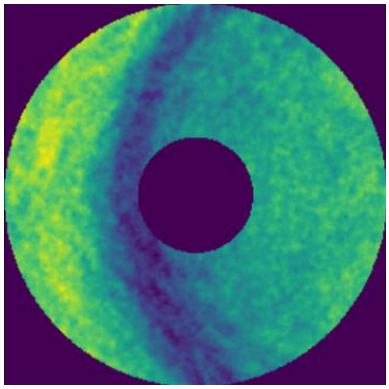

(c) Residual wavefront observed because of the LGS beam elongation (YAO). The color coding of the figure represents the difference of path, from blue to yellow.

Figure 3.2: Illustration of the elongation problem for an ELT-size telescope

To mitigate these effects, the idea is to truncate the signal as few as possible while still being able to sample it and performs the operations at 1,000 Hz. Thus, there are three major constraints on this WFS:

- The Field of View of the WFS has to be as large as possible, to mitigate the truncation effects. Typical size for an ELT LGS seen by a subaperture is ≈ 25" × 1" as it can be seen on Figure 3.2a. Ideally, the FoV of the SH-WFS should be of 25" × 25".

- The pixel size of the WFS has to be small enough so that the short dimension of the LGS is still sensed. Here, if the pixel size becomes larger than 1", the information is lost on the transverse direction of the PSF. It has a consequence a loss of precision for the slopes computation. Thus, a minimum pixel size of 1" is required for these sensors. In practical, it has been shown with simulations that a pixel scale equal to 1" creates a direct loss in the Strehl ratio. Thus, pixels of 0.5" will be used for the simulations. Smaller pixel scales such as $0.25"/pix$" were not bringing significantly better results in the simulations.

- Finally, the information has to be processed and applied in real time. The current baseline design for the ELT SLAO is a ≈ 40 × 40 sub-apertures SH-WFS. Thus, having a 25" × 25" FoV with a pixel scale of 0.5" requires 50 × 50 pixels per subapertures, which makes in total 2000 × 2000 pixels. Currently, the maximum configuration enabled with the current hardware/software is the processing of 800 × 800 pixels at 1 kHz, which decrease in that case the FoV at 10" × 10". The final configurations retained because of this is a 40 × 40 SH-WFS, with 20 × 20 pixels per sub-aperture with a pixel FoV of $0.5"/pix$, which makes a total FoV of 10".

Even if these effects are mitigated by the design of the high-order WFS, they still influence the behavior of the SLAO system. For this reason, truth sensing is required to compensate for these effects.

3.3. The Sodium layer profile

As it has been seen before, the Laser Guide Star is created by exciting the sodium layer of the mesosphere at 90 km by a laser tuned at the right frequency. However, the profile of the sodium layer evolves with time, on hours and daily scales. The purpose of this part is to present the effects created by the sodium layer profile and the influence of its variations on AO system performances.

3.3.1. The influence of the sodium layer

To be able to understand and correct the influence of the thickness of the sodium layer properly, several simulations have been conducted with the YAO simulator (see Chapter 5). The configuration taken is a SLAO system, with SH-WFS for the LGS sensing and PWFS for the TT sensing. The parameter that changes here is the sodium layer thickness, to understand its influence on the simulation performances. The SH-WFS is a 40×40 sensor, with 4×4 pixels. The individual pixel FoV is 0.5". The results can be found in Figure 3.3, as a plot of the Strehl evolution relatively to time for 1,000 iterations of 1 ms. Base on what has been presented just before, the FoV of the system is not large enough to sense properly the 25" beam. The purpose here is to see what are the consequences on the system performances.

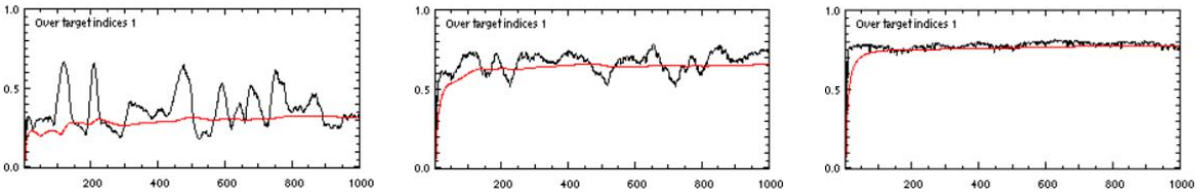

(a) $\Delta z_{Na} = 10\ km$ (realistic thickness) (b) $\Delta z_{Na} = 5\ km$ (c) $\Delta z_{Na} = 2\ km$ (Na thickness scaled to the VLT)

Figure 3.3: Evolution of the Strehl ratio relatively to the number of iterations, for SLAO configuration with SH-WFS 40×40, 4×4 pixels and 0.5" pixel FoV (YAO)

The main result is the one expected: the thicker the sodium layer, the more unstable and the less the performances of the AO system. For a realistic thickness (cf Figure 3.3a), high instabilities in the instantaneous Strehl ratio (black curve) can be seen. On the other hand, for a thickness of $\Delta z_{Na} = 2\ km$, the system is almost perfectly stable. This 2 km width scales to the one seen by a telescope such as the Very Large Telescope, where the diameter of the telescope, $\approx 8\ m$, is 5 times less important than the ELT one. The Figure 3.3c shows indeed that the problem of truth sensing was almost absent in the case of the VLT since the elongation was not significant enough for the sensors to be perturbed while they measure the wavefront.

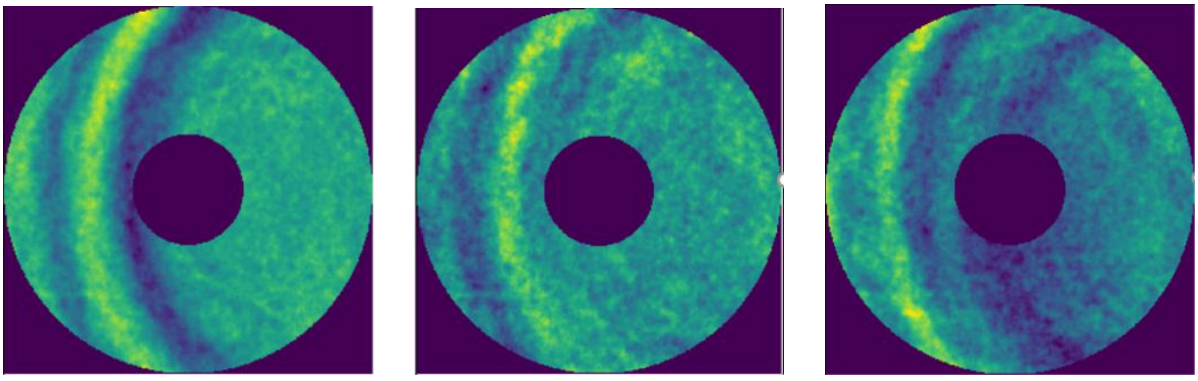

(a) $N_{iter} = 600$ (b) $N_{iter} = 800$ (c) $N_{iter} = 1{,}000$

Figure 3.4: Evolution of the residual over the iterations

The direct consequences of the beam elongation are the appearance of residuals after the mirror correction: since the system is not able to sense the slopes of the wavefront correctly for some locations, the wavefront is not well corrected there. More precisely, it can be seen in Figure 3.4 that some patterns appear in the residual,

corresponding to offsets created by the LGS WFS. Even if the wavefront is entirely flat, because the sensing is not done correctly, the WFS still see a deformation that needs to be corrected. This deformation is not real; it is created by the incapacity for the system to see the entire LGS beam, which thus infers an erroneous slope with the centroiding. Let's imagine for example a profile such as the "Very Wide" presented in Figure 3.5. If the beam is cropped at some point, it means that the outer peaks might not be detected for some local atmospheric distortions. This effect creates the false measurements on the LGS WFS, even if there is no perturbation at all at the beginning. The LGS WFS then sends information to the M4 mirror to compensate for these "imaginary" perturbations, which distort the wavefront for nothing.

Has a consequence the appearance of residual patterns as the ones in Figure 3.4 that decrease the system performances. If the patterns are fixed, it is possible to correct them with a Truth Sensing system, as it will be explained in chapter 4. It means using a Natural Guide Star to observe these patterns for an extended period. When these patterns are a consequence of the beam elongation, they are supposed to change as fast as the sodium layer variations, which have timescales of several minutes or hours. Therefore, a long exposure time can be used to limit the constraints on the NGS magnitude. However, the instabilities observed in Figure 3.3a mean that the residual is changing over time. The Figure 3.4 shows how the patterns observed are not fixed over 400 ms. To compensate the low order instabilities by truth sensing, the residual patterns created by the WFS have to be constant. If the patterns change too fast, the truth sensing will not have time to correct it properly. The primary goal of the SH-WFS for the LGS is, therefore, to provide a stable correction under any circumstances, mostly regarding any sodium profile.

3.3.2. The different sodium profiles

The work of Pfrommer and Hickson, 2014 [57] illustrates the variations of the sodium profile, and how they could impact a LGS AO system. Figure 3.5 shows the main profiles that have been identified during their observations, and how these profiles are sampled to be incorporated into the YAO simulator.

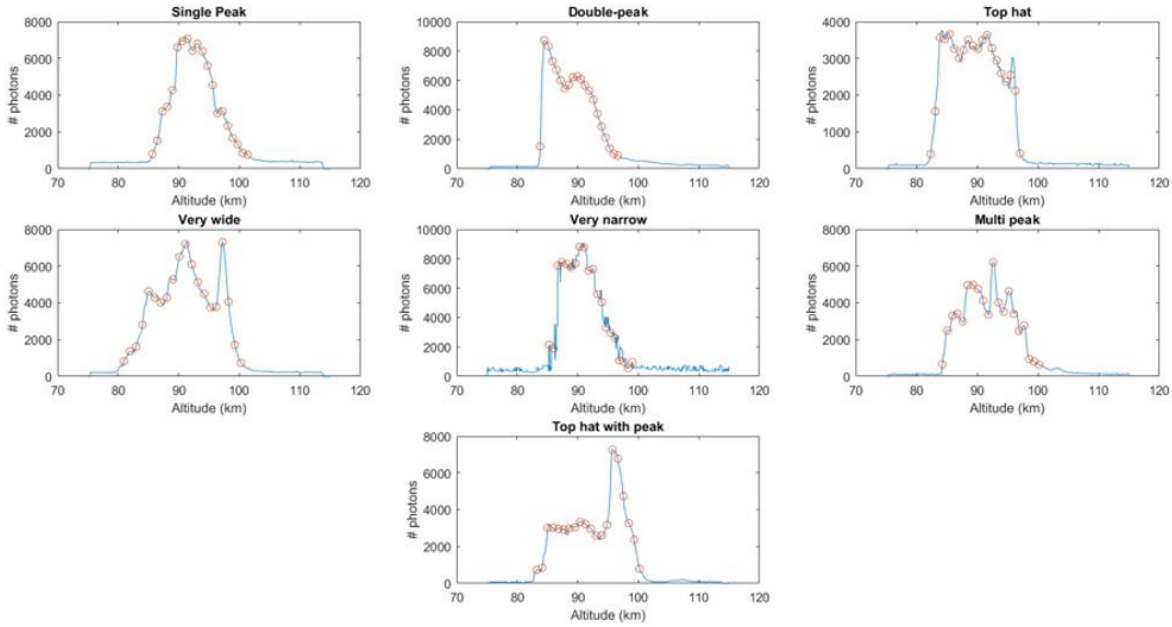

Figure 3.5: Distribution of the sodium concentration regarding altitude. The blue curve represents the actual data (Pfrommer and Hickson, 2014 [57]), the orange dots the points used in the YAO simulations.

These profiles are numerous, and all have approximately the same probability of appearance (≈ 15%). It can be considered that these profiles represent a type of profile: a given sodium profile at one moment will look like one of them, while still having its components (altitude of the peaks, relative concentration, ...) changed. It is important to note that the residual patterns discussed before will highly depend on the type of profile. The impact of these profiles on the Strehl ratio performances are illustrated in Table 3.1, where the Strehl ratio of an SLAO simulation (optimal configuration, see 5) without truth sensing has been made.

For half the profiles, the performances are already good, and the truth sensing would sometimes not even be

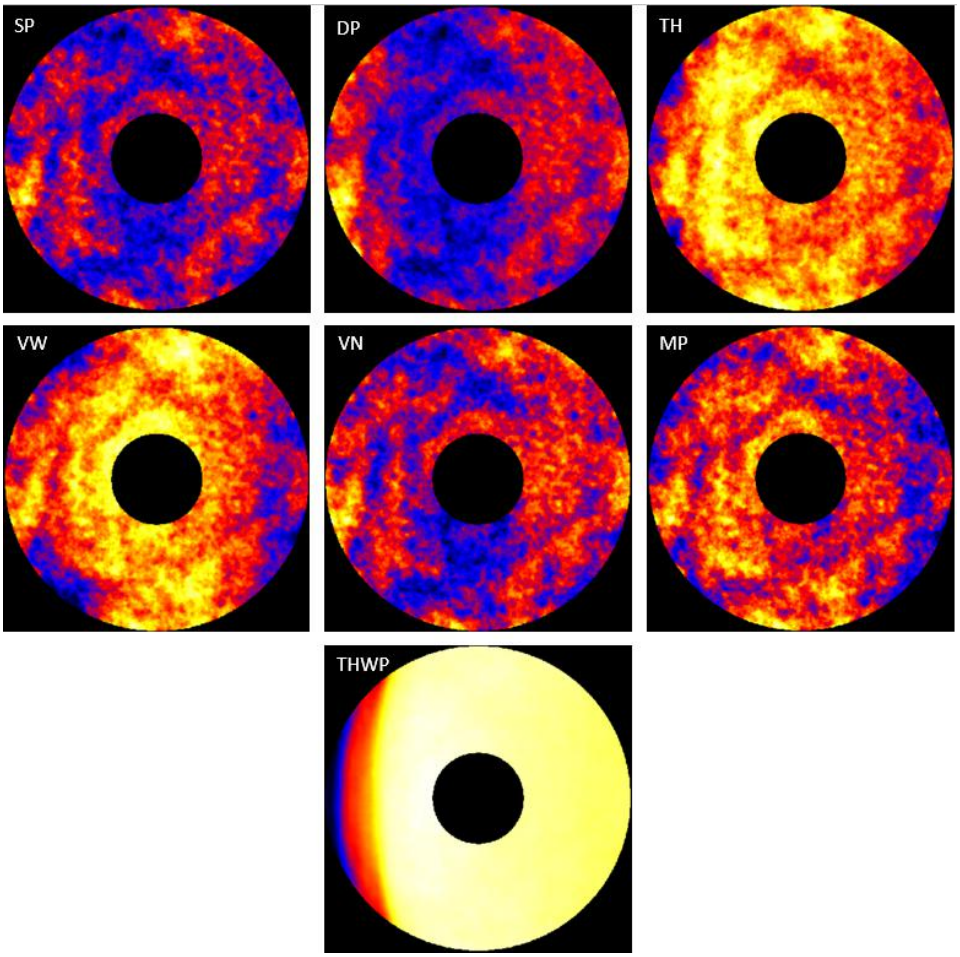

Figure 3.6: Residual screens obtained with YAO simulation without truth sensing. Each image corresponds to the profile from Figure 3.5

Table 3.1: Strehl ratio performances obtained with different types of profiles, without truth sensing

Profile	Single Peak	Double Peak	Top Hat	Very Wide	Very Narrow	Multi Peak	Top Hat With Peak
Strehl Ratio	53%	37%	40%	27%	50%	50%	12%

required to correct the residuals. However, the other half shows decreases in the Strehl ratio. It is important to notice that the shape of the residual did not change over the iterations, which means that the SH-WFS provides a stable correction. The residuals can be seen in Figure 3.5: some of them have very diffuse patterns (like SP, TH, VN, and MP) where only a small central feature can be seen. However, for others the features are way more pronounced, the worst example being the top hat with peaks where the Strehl ratio is the lowest. The remaining offsets can be easily corrected by truth sensing: it is not possible to show it here, but the residual patterns are constant in time and not changing. These results have been obtained with the configuration discussed before, which means a 10" FoV with $0.5"/pix$ sampling for a 40×40 sub-apertures system.

From this part, the critical thing that can be remembered is that without Truth sensing that will correct the fixed patterns (see chapter 4), the performances of the SLAO system are directly linked to the shape of the sodium profile in the sky.

3.4. Recommendation

The main recommendation from this part would be to create a MATLAB WFS system for the LGS sensing. The SH-WFS behavior has been studied at the beginning of the thesis: the pixel size, FoV, weighted methods for the pixels play an essential role on the sensibility of the system. The possibility to create a system from scratch (as it is the case in the next Chapter) will allow testing precisely the best configurations to tackle the elongation effect, and better understand the reason behind the offsets created. It will also allow having more control on the LGS beam created, and reduce considerably the computation time.

Conclusion

This part has clearly illustrated how difficult it is to perform adaptive optics with a single laser for a telescope with the ELT's size. The main limitation is the elongation created because the laser which is creating the LGS is launched from one of the ELT side, 18.5 *m from its center. This elongation is considerable, generating an elongated source that can have dimensions such as* 25" × 1". *However, the WFS that needs to infer the atmospheric perturbations from the LGS cannot have a FoV larger than* 10", *for a pixel size sufficient to correctly sample the LGS. Which crops the LGS, losing by this operation information that could be used for the local slope determination. The consequence of this information loss can be seen by the appearance of fixed patterns in the correction's residual, decreasing the Strehl performances of the system. These performances seem to be highly related to the sodium profile of the atmosphere: while in some cases a Strehl of* 60% *seems to be reached, some profiles display more important losses.*

Chapter 4

Preliminary investigation of the Low-order Wavefront Sensor

As it has been explained before, any LGS-based AO system requires a Natural Guide Star (NGS) for the low-order sensing (Tip/Tilt). It will also be used as a reference for the focus of the instrument since the sodium layer altitude is varying with time, and also to correct the high-order WFS offsets created by the spot elongation: the Truth Sensing. Since the Pyramid WaveFront Sensor (PWFS) is used for the SCAO system, the same sensor would be used with a lower resolution, so that it can sense the tip/tilt modes. Although a NGS is still required, the possibility to bin the subapertures and to use a longer exposition time decrease the constraints on the star brightness, thus increasing the sky coverage.

Contents

4.1. Pyramid Wave Front Sensor for the truth sensing

4.1.1. The principle of PWFS

Pyramid Wave Front Sensors (PWFSs) have similar behavior as a SH-WFS with a bi-cell configuration. However, the analysis is made in a different plane: the image plane for S-H WFS and the pupil plane for the PWFS. The principle is illustrated in Figure 4.1.

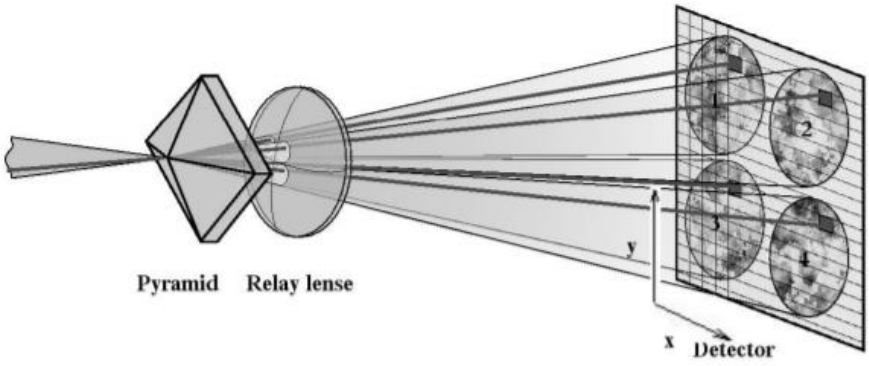

Figure 4.1: The principle of the PWFS (Davies and Kasper, 2012 [21])

The beam coming from the Natural Guide Star (NGS) is split in 4 sub-beams in the pupil plane. Each of these sub-beams is then imaged on a detector. For a given pixel on the detector (the dark one of Figure 4.1), the slope is calculated with the formula used for bi-cell SH WFS (cf Equation 3.1 and Equation 3.2) with the pixel values on the other detectors. The local slope can, therefore, give the information about the amount of perturbation by the atmosphere. However, to obtain correct measurements, the beam has to be modulated to increase the linearity range of the instrument. In practice, it means slightly rotating the beam around the middle point to create an extended annular source rather than the punctual one. This increase in linearity is made at the expense of sensitivity, but the possibility to control this modulation makes the system very adaptable to different situations.

The main advantage of using this technology is that PWFSs give better performances in K-band than SH-WFSs for faint guide stars (Bertram, 2017 [8]). This is a consequence of the resolution used for the sensor: in the PWFS, there is no binning in the pupil plane, which means that the resolution of the system is the same as the telescope resolution. If D is the telescope diameter and $d = D/N_s ub$ the sub-aperture diameter in the SH lenslet array, then the resolution for PWFS is $\approx \lambda/D$ while for the second case it is λ/d. For example, the resolution of the 40×40 SH-WFS on the ELT will be the same as a $37/40 \approx 1\ m$ telescope. The PWFS seems to be the ideal sensor for extending the sky coverage as much as possible for the SCAO system. Similarly, it will be used here to decrease as much as possible the required brightness for the system for Truth and Tip/Tilt sensing.

4.1.2. The Tip-Tilt correction

The Tip/Tilt from the atmosphere has no immediate consequences on the instantaneous Strehl ratio since its immediate effect is just a displacement of the PSF in the atmosphere by a fraction of the corrected PSF FWHM. This "beam wandering" will decrease the long exposure Strehl: the short exposure PSF are combined by "stacking" the images, which means adding them together to decrease the noise and increase the signal. But if the PSF is not precisely at the same place at every frame, it has a consequence a scattering of this PSF, thus a diminution of the long-term Strehl ratio. The difference between the high-order mode detection, as it is the case in SCAO, is that the number of subapertures can be reduced to only one, the size of the telescope. It means that the magnitude of the star can be much higher (flux lower). The temporal variations of the signal are also supposed to be slower (not verified in simulation yet), which might enable a longer integration time: the frequency of the Tip/Tilt sensing does not have to be $1,000\ Hz$, but maybe 500 or 100 Hz. Something that also needs to be taken into account is that the system will need to compensate for the perturbations created by the telescope vibrations. Such a large structure is moved by the atmospheric winds in the Armazones. This part represents the most important correction that needs to be brought by the system, estimated as 70%.

4.1.3. The Truth sensing

The Truth sensing correction is the second type of correction that would be brought by the SCAO PWFS. The NGS sensing will be used as a reference, to correct the effects created by the LGS sensing.

LGS WFS patterns correction

As it has been discussed in section 3.2, the spot elongation becomes a real problem for LGS AO systems in the ELT case (Schreiber et al., 2009 [69]). The solution is to use the truth sensing: using a Natural Guide Star to measure the constant offset created by the LGS WFS and subtract this offset directly from the measurements of the LGS WFS. The NGS sensing is not biased by the elongation effects: if it is assumed that the exposure time is long enough, the atmospheric perturbations can be considered as approximately equal to 0 (the mean of the perturbations in the sky is null). What remains in the measurements after the exposure time is the residual patterns created by the LGS WFS, that are evolving much slower in time. Since the NGS is basically a point for the sensors, there is no need to use large FoV, to crop the LGS.

Focus for the LGS WFS

Another application of Truth sensing is the monitoring of the sodium layer altitude. As it has been illustrated in Pfrommer et al., 2009 [58], the sodium density distribution can change with daily scales. Since the focus of the LGS WFS is made directly on the layer, a slight change in altitude creates a defocus of the WFS. It will interpret this defocus as an atmospheric deformation and will distort the mirror accordingly, to re-focus the LGS WFS. However, since the science object observed is at infinite, this deformation of the mirror will not compensate any focus changes: the quality of the image will be even more degraded. Using a NGS will help to decrease this effect, as the focus variations measured by the LGS WFS can be monitored and compared to the ones observed by the NGS. If only the LGS WFS measures focus distortions, it means that the sodium altitude has changed and the focus needs to be done on the LGS WFS.

Using a Natural Guide Star will decrease the sky coverage, but the truth sensing is done at a rate much lower than the high-order sensing (10 Hz instead of 1,000 Hz). Which means that the integration time can be much longer, and so is the magnitude since more time is allowed to gather light.

4.1.4. Using the SCAO PWFS

As it has been explained before, the truth and tip/tilt sensor used will be the PWFS located inside the cryostat that will already be used for the SCAO system. The main advantage of this solution is that the system does not require the installation of another instrument, using the existing one. It is both cheaper and more straightforward, going with the requirements of the SLAO.

The SCAO sensor is an 80×80 PWFS, whose beams are projected on a SAPHIRA detector (Selex, 2014 [71]), and can run at 1,000 Hz. To transform it into the truth sensor required, the idea would be to use numerical operations on the system to turn it into a 10×10 for truth sensing or 1×1 for the tip/tilt sensing. This binning is done by numerically adding the values of each pixel. Since the noise is uncorrelated for each pixel, this considerably decreases the read-out noise and dark current one (see after). The system will need to be run at the tip/tilt frequency, which will be probably equal to 1,000 Hz or 500 Hz. For adapting it to the truth sensing and increase the exposure the time, it requires to store the information of every pixel at every iteration and send the data to the controller every 0.1 sec.

For these reasons, the simulator of this part has been built to simulate the PWFS performances, whose pixels have been binned together to reach the desired configuration. The only difference here is that to save computation time, the system is considered to have an integration time of $T_0 = 0.1$ sec instead of adding 100 frames with $T_0 = 1\ ms$. This is not supposed to have any consequences for the first estimations provided. However, a more developed system will have to do as the first case, at the expense of 100× more important computation times.

4.2. The simulation of the PWFS

Truth sensing is a problematic of LGS-based Adaptive Optics that is relatively new. As it has been seen in chapter 3, the elongations problems mainly come from the diameter of the telescope, which will be 5× larger in the case of the ELT class. For this reason, the simulator YAO has no implementation of truth sensing. This part will present the simulator build in MATLAB during the Master Thesis to apply the truth sensing correction on the residual created.

4.2.1. The MATLAB simulator

This simulator has appeared as mandatory for several reasons:

- The first one was because the truth sensing could not be implemented directly into YAO. This simulator has been created for older AO simulations, where the truth sensing was not mandatory. The language used in YAO is mainly in *yorick*, which is difficult to master for just the period of the project, with some scripts in *C* to accelerate some parts.
- The second reason deals with the stability issues of the system. Typically, the truth sensing and the LGS sensing are made in real time at different frequencies. The gain for both has to be chosen very carefully, as the stability of the system highly depends on these choices. A discussion with one of the specialists of automatics at Leiden University highlighted how sophisticated the control could be. Having an independent simulator working with the residual created by YAO allows removing these dynamic effects. For an in-depth analysis, this assumption will not be valid anymore. However, for this project, this is enough for having a first estimation of the SLAO system performances.
- The third reason lies in the computation time. As it has been explained in chapter 3, a large field of view is required to deal with the beam elongation. This increase in the FoV is made at the cost of a larger pupil sampling for the simulation, which has a direct impact on the computation time for the simulations. For the "optimal" configuration, 1 sec of simulation takes $24h$ to be performed. Using a different, less complicated system with a lower sampling (see explanations in 5) allows performing Truth sensing simulations much faster, with 1 sec truth simulations computed in less than a minute.
- Finally, creating a MATLAB simulator allows to much more improve the control of the variables. This is particularly true for the noise implementation, that is made obscurely in YAO. Here, the guide star spectrum, atmospherics transmissions (see chapter 8) can be completely changed and perfectly adapted to the problem, leading to more precise results for the sky coverage estimation.

The algorithm that has been used can be summarized in Figure 4.2. The blue and orange rectangles represent the functions used by the loop and the calibrator. These functions will be described more in details in the following chapter.

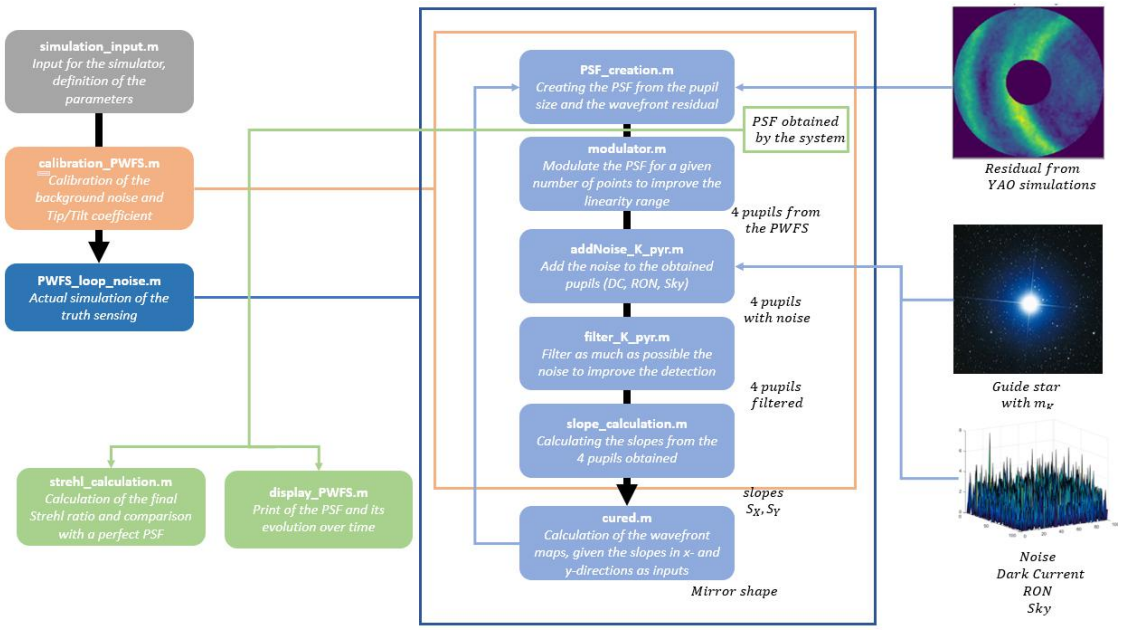

Figure 4.2: Summary of the truth sensing algorithm implemented in MATLAB

As it can be seen here, the simulator uses the residual patterns created by the YAO simulation. The YAO simulation takes into account the effects of the LGS WFS and the Tip/Tilt correction at 1,000 Hz, and delivering residuals every 100 iteration so the truth sensing can be performed at 10 Hz.

4.2.2. The Fast Fourier Transform

The transformation of an optic system from the pupil plane to the image plane (or the opposite) can be generated mathematically with the Fast Fourier Transform. Because of this property, this function will be used very often in all the simulator. This mathematical function can be represented in one dimension as:

$$\mathscr{F}\left(f\right)(v) = \tilde{f}\,(v) = \int_{-\infty}^{+\infty} f(t).e^{-2\pi i.tv}\mathrm{d}t \tag{4.1}$$

In two dimensions, the formula is slightly different, but the principle remains the same.

$$\mathscr{F}\left(f\right)(u,v) = \tilde{f}\,(u,v) = \int_{-\infty}^{+\infty}\int_{-\infty}^{+\infty} f(x,y).e^{-2\pi i(x.u+y.v)}\mathrm{d}x\,\mathrm{d}y \tag{4.2}$$

For an image, this formula changes since there is only a finite number of elements in it. For an image with dimensions $M \times N$ it becomes:

$$\mathscr{F}\left(f\right)(m,n) = \tilde{f}\,(m,n) = \sum_{j=1}^{M}\sum_{k=1}^{N} f\left[j,k\right].e^{-2\pi i\left(\frac{j.m}{M}+\frac{k.n}{N}\right)} \tag{4.3}$$

The result of a 2D-FFT with the original image can be found in Figure 4.3:

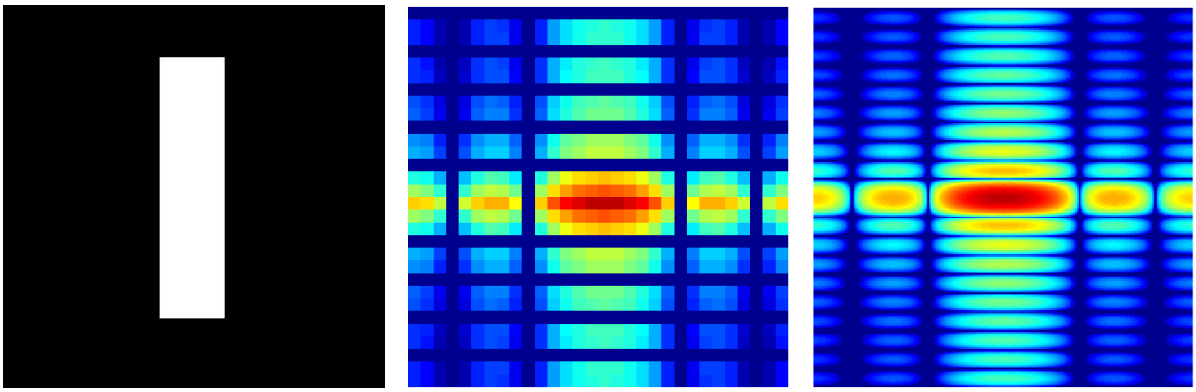

(a) Original object (b) FFT with no padding (c) FFT with padding

Figure 4.3: Illustration of the FFT for a simple object

What can be understood from this image is that the FFT shows the main frequencies that appear in the picture. The frequencies in the x-direction are along the x-axis, and the ones in the y-direction along the y-axis.

The FFT is a very efficient algorithm. However, one needs to be careful about its parameters, because this algorithm is sensitive to the numerical noise created. The first thing to do is to padd the image, which means centering the image in a table with only zeros. The reason for that lies in the theory of FFT: the multiplication in the frequency domain corresponds with a circular convolution in the spatial one. If the image is not padded properly, the results from one side of the image will wrap around to the other side of the image. It might have a consequence interference with the signal, and additional noises. The Figure 4.3b illustrates well this problem, especially when it is compared with the padded Figure 4.3c. When padded, the spectrum is smoother with a higher resolution, enabling a reduction of the noise. The second will be to deal with an even number of pixels to make the algorithm faster. Indeed, the algorithm used the principle of "Dividing the Realm to Govern": the image on which the FFT needs to be done is subdivided in images with half the size until it is not possible to divide the image anymore. Thus, to take the padding into account, the size of the images will be set to 2^N where N is found with the MATLAB function *nextpow2* so that the dimensions are both a multiple of 2 and big enough to pad the image. Here in Figure 4.3, the original figure is 30 pixels large, and the padded one $256 = 2^8$.

Something fundamental that needs to be kept in mind is that, although the implementation of the FFT is quite fast, the complexity of the algorithm is scalable to $n.\log n$. Therefore, using very large FFT by over-padding, for example, can considerably increase the calculation time. A good compromise needs to be taken between the limitation of the noise and good computation time.

4.2.3. Simulation of the atmospheric effects and PSF creation

By extracting the residual after the higher-order correction by the ELT M4 and TT correction from M5 mirror, it is possible to simulate the Truth sensing with a MATLAB algorithm. To produce the residuals, the YAO simulator has been used in a SLAO configuration. The residuals are directly extracted in ".fits" format. The time between two images is set to 100 ms, which corresponds to the baseline of the truth sensing (10 Hz, 100× slower than the global AO loop).

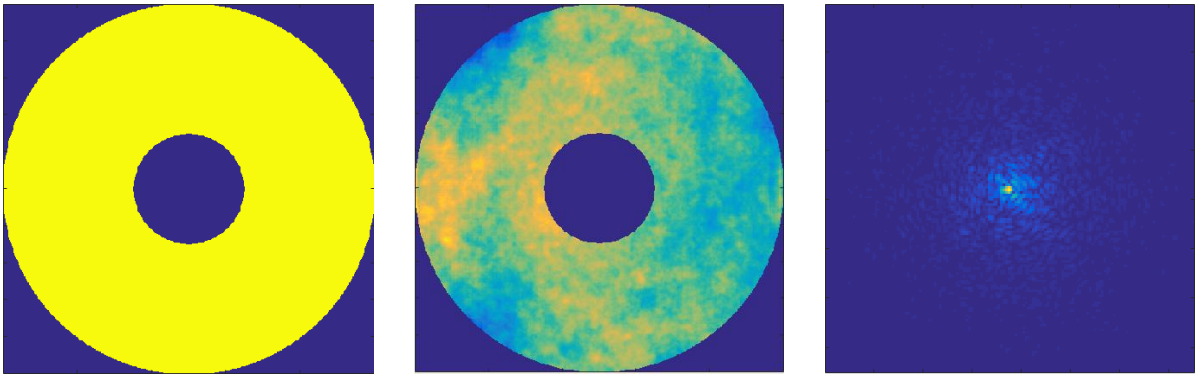

(a) Pupil of the telescope

(b) Residual from the atmosphere

(c) PSF low Strehl (< 20%) obtained from the pupil and screen

Figure 4.4: Pupil, screen created by atmospheric effects and the resultant PSF

The pupil is also generated with this residual, by setting to 1 every value that is different from 0 (see Figure 4.4a). The pupil consists of a figure with only 0 when the pixels are outside the telescope diameter or inside the hidden zone and 1 otherwise. It is important to note that the pupil has been cropped exactly at the dimensions of the primary mirror, whereas the residuals are at the beginning are already padded. Since the simulations made in YAO require a high number of points for the pupil diameter (< 3,000, see chapter 5), the pupil images have been re-scaled to a smaller size (500). Here the sensing is done mostly in the J/H/K-band so at a wavelength $\lambda \approx 2\ \mu m$. The field of view simulated is 2", which means that the field stop diameter must be equal to:

$$pupildiam = D/\lambda \times FoV = 123\ pixels \tag{4.4}$$

In practical, a larger number of pixels will be taken, since the resolution of the system is not exactly equal to λ/D. The simulations have been made with a pupil diameter of 500 $pixels$. However, a field stop has been implemented, which size is equal to the desired FoV.

The units in the phase screens are in μm: it represents the path differences created by the atmosphere perturbations. The path differences can be converted to phase differences with the formula:

$$\phi[m,n] = 2\pi \times \frac{screen[m,n]}{\lambda} \tag{4.5}$$

where λ is the wavelength of the observation. Something important here is that the wavelength of the observations will be different from the WFS wavelength. For this reason, two PSFs have to be created, at respectively 2.2 μm for the sensing and 3.7 μm for the PSF that will define the performances. Once the phase screen obtained with the displacement error per pixel, the PSF can be defined as (neglecting padding):

$$PSF[m,n] = pupil[m,n] \times e^{i\phi[m,n]} = pupil[m,n] \times e^{2\pi i \times screen[m,n]/\lambda} \tag{4.6}$$

The PSF obtained (see Figure 4.4c) at 3.7 μm is stored and will be used at the end to calculate the Strehl ratio and represent its evolution along the iterations. The PSF estimated at 2.2 μm will be used to determine the slopes created by the atmosphere.

4.2.4. Modulation of the signal and pyramid splitter

Once the PSF created by the system, the next step is to simulate the influence of the modulator and the pyramid on the incoming light beam. This will create the 4 pupil images that can then be compared to calculate the slopes.

The modulation of the signal

The goal of the modulation is to create a signal more extended than the PSF received. Physically, the modulator is drawing circles at the tip of the PWFS at a frequency that is a multiple of the acquisition time T_0. In practical, some points are defined, in addition to an amplitude that represents the radius of this circle. The way this modulation has been implemented is by translating the PSF in a given direction. For example, given the amplitude R and the number of points N, it is possible to define N angles θ_k such that $\theta_k = 2\pi k/N$, so that the coordinates of the translation can be written as $[x_k, y_k] = [R\cos\theta_k, R\sin\theta_k]$. For every coordinate, the whole PSF is translated with the MATLAB function *imtranslate*. As a result at the end, N PSFs that are arranged in a circle. The Figure 4.5a gives a graphical representation of what will be seen by the system. This is not exactly what the system sees since every point on the PSF are seen individually at several epochs.

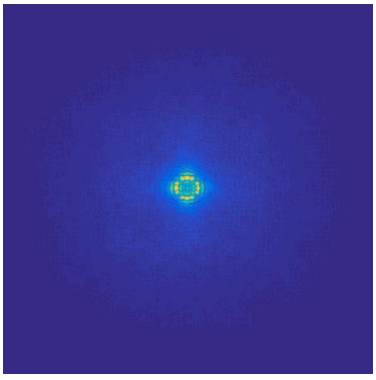

(a) Modulation of a high Strehl (> 95%) PSF with $N = 16$ and $R = 4 \times \lambda/D$

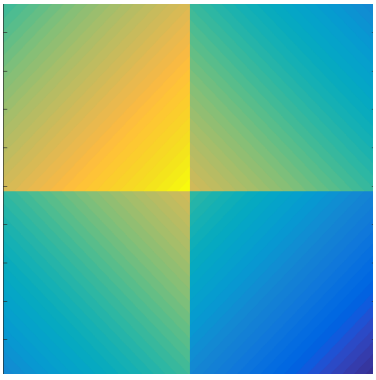

(b) The rotation matrix used to generate the sub-beams

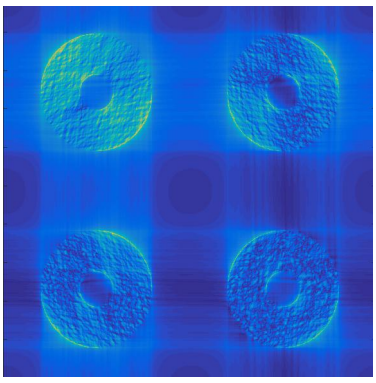

(c) The four pupils generated with the rotation, corresponding to the four sub-beams created by the pyramid

The Pyramid optic

The PWFS has an import optics, which is the Pyramid beam splitter. Coupled with a relay lens, this object will create 4 images of the telescope pupil. The way to simulate this pupil is to apply an inverse FFT on each of the N PSF translated by the modulator, and add them together at the end. To split the image in 4, a rotation matrix α_{mat} is used (see Figure 4.5b). This matrix will be put as a phase for the inverse FFT. Thus, the Figure 4.5c is obtained with the following formula:

$$pupil_4 = \sum_{k=1}^{N} iFFT\left(PSF_k \times e^{2\pi i \alpha_{mat}}\right) \tag{4.7}$$

Since the detectors are unable to see the phase of the light ray, the modulus of the complex number is taken: the phase information is lost in the process.

4.2.5. Normalization of the signal and noise addition

Once the four sub-beams created, noise can be added to the signal. To add it, the pixel size has been changed by re-binning the image, so that the number of pixels is equal to the 80 sub-apertures for the METIS SCAO system. Since the WFS of the system will be used for the truth sensing, this choice felt completely logical. The re-binning from a 500×500 image to the 80×80 image is done with the function *imresize* of MATLAB. Now each

pixel represents a real pixel in the SCAO system. The following part will describe the noise implementation, but the values used to implement the noise will be described later in the Sky Coverage part in chapter 8. The noise implementation is in reality much more difficult, since the spectrum, sky emission and transmissions of the system are wavelength dependent. This part explains the basic concept.

Normalization of the signal

The signal needs to be normalized so that the pixel intensity distribution on the pixels represents the one that would be expected from a star of a given magnitude m_K. From this magnitude in the K-band, it is possible to retrieve the flux received by the detector in photons I, given the exposure time T_0, the flux at zero magnitude $F_K = 2.19 \times 10^9$, the diameter of the primary aperture $D = 37\ m$ and the optical transmission of the system $\eta \approx 0.5$:

$$N_{ph,K} = F_K.10^{-m_K/2.5} \times \frac{\pi D^2}{4} T_0 \eta \tag{4.8}$$

The 4 sub-beams that have been created can then be normalized. This is the normalization formula for the sub-beam intensity I_k with $k \in [1..4]$:

$$I_k[m,n] = \frac{I_k[m,n] \times N_{ph,K}}{\sum_{k=1}^{4} \sum_{i=1}^{N} \sum_{j=1}^{N} I_k[i,j]} \tag{4.9}$$

As it will be explained more in details in Chapter 8, the calculation of the signal emitted from the star is, in reality, more complicated if calculations need to be performed for large bands (JHK for example). What is used in the final algorithm is a value N_{ph} that corresponds to a number of photons emitted from the star in the given bands. The normalization will then be performed directly with this value.

Photon-noise

This noise is the consequence of the finite value of photons: there could be for example 21 photons on a given pixel but not 21.2. Has a consequence an additional noise that can be assimilated as $\approx \sqrt{N_K}$. To respect the randomness of the noise, the Poisson distribution is used. The parameter λ for the distribution will be set as $\lambda = N_K$. This noise is directly added with the MATLAB function *poissrnd* to the 4 pupil images created. Every pixel will be set to a Poisson random value so that the pixel value is the parameter λ of the distribution.

Sky-noise

The sky is emitting in the background, creating a random signal. The randomness of this signal can be assimilated to a Poisson Distribution with a mean value of $m_{sky,K} = 12.9\ mag/"$. It will be explained later in Chapter 8 that the noise value changes relatively to the wavelength, so this value will slightly change according to the waveband used. To add the sky-noise to the 4 pupils, the method is to generate an 80×80 array of random values with a Poisson distribution centered around $N_{sky,K}$. What will be done is similar to the signal normalization. A given number of photons N_{sky} will be calculated based on the sky spectrum and atmospheric/instruments transmission (see Chapter 8), and will be directly put as noise with the method described here.

Read-Out Noise

The RON is a consequence of the uncertainty while reading the number of electrons that have been impacted by photons. This noise is random and can also be assimilated to a Gaussian distribution. To compensate for this noise, Avalanche Photo Detectors (APD) amplify the received signal, weakening the impact of the RON. This is illustrated by the presence of a gain G. For the SAPHIRA detectors used for the SCAO WFS, the standard deviation is equal to $\sigma_{RON} = 1\ e^-$ and the gain $G = 30$ (Selex, 2014 [71]). The noise is added with a Gaussian function *gaussrnd*, which amplitude is equal to σ_{RON}/G.

Dark Current noise

The DC noise represents the current falsely measured by the detector even if there is no signal. If no light at all is hitting the sensors, it will still measure a faint random current per pixels. For the SAPHIRA detectors, the dark current is 430 $e^-/pix/s$. This value, multiplied by the integration time T_0, gives the mean of the DC

noise, randomly distributed again with a Poisson shape. The implementation of the noise is the same as for the sky noise, with the generation of random 80×80 arrays of values.

The final signal can thus be obtained with the following formula:

$$PSF_{noise} = (PSF + SKY_{noise} + PH_{noise} + DC_{noise}) \times G + RON \tag{4.10}$$

The noise filtering

After adding the noise to the image, the noise filtering needs to be simulated. Usually, frames of the sky without any light are taken to measure the mean sky intensity on a given location. The value of the sky is then removed from the signal obtained. The way to estimate the atmosphere emissions from a frame is a complicated task and will not be described in this work. It is here assumed that the sky emission is uniform for the FoV considered and that the noise is correctly estimated and removed during the data processing with the chopping. Once the mean value of the sky and dark current noise removed, what remains is similar to a Gaussian shape centered around zero with a standard deviation equal to the square root of the Poisson distribution mean value. This assumption is important, especially for the sky as it assumed that the sky could be measured very precisely. However, the chopping method used to estimate and remove the sky value is not perfect, and some additional errors can subsist.

4.2.6. The slope sensing

With the four images obtained, it is possible to calculate the individual slope per pixel. But before that, the pixels need to be binned together to increase the signal to noise ratio of the system. Here the baseline for the truth sensing is with a 10×10 sub-apertures configuration, which is a good compromise between enough spatial resolution to compensate for the LGS WFS offsets and binning enough to increase as much as possible the sky coverage.

The image is for this reason separated into N_{sub}^2 subapertures, and the illumination is computed for each pixel. It represents the fraction of pixels that have a signal in the sub-aperture. If this fraction is lower than an illumination fraction f_{illum}, the whole subaperture will be ignored (the values are set to NaN for all the sub-aperture). A mean of the pixels slope is made per subaperture: the value of one subaperture intensity is the sum of all the valid pixels $S_X[m,n]$ contained in it, divided by this number of valid pixels N_{pix} (the ones inside the pupil):

$$I_{k,sub} = \frac{1}{N_{pix}} \sum_{[m,n] \in sub} I_k[m,n] \tag{4.11}$$

To avoid the edge effects and use a clear re-binning, the number of sub-apertures used has to be a multiple of 80. It might be possible to use the function *imresize* provided by MATLAB, to tackle this issue.

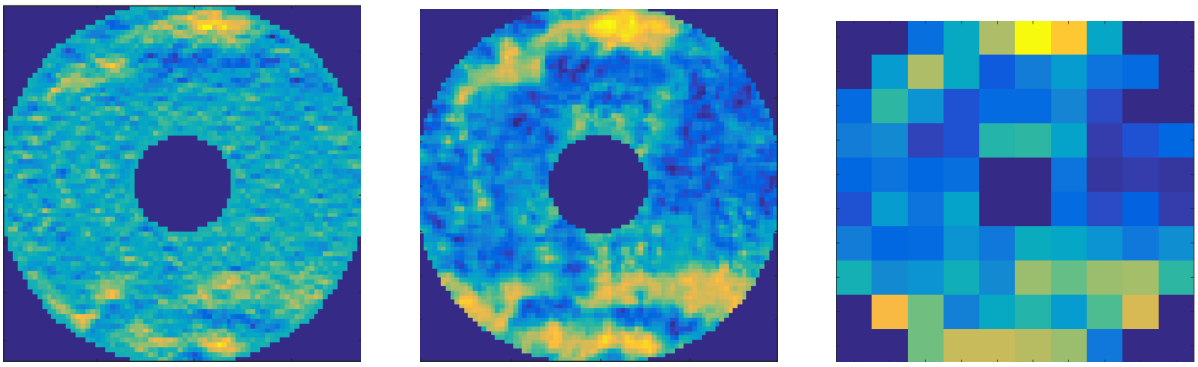

(a) True slope calculated directly from the atmospheric screen for verification

(b) Slope in the X direction computed with 80×80 sub-apertures

(c) The slopes in the X-direction computed with 10×10 sub-apertures

Figure 4.5: Generation of the sub-apertures and comparison to the real slope

Once the pixel intensity calculated, the slope can be obtained. As it has been explained before, the consequence of a local distortion of the atmosphere in a direction will create a local difference of intensities. The sampling is here made by the sub-apertures, and the slopes for a given pixel $[m,n]$ can be computed as:

$$S_X[m,n] = \frac{I_2 + I_4 - I_1 - I_3}{I_2 + I_4 + I_1 + I_3}[m,n] \tag{4.12}$$

$$S_Y[m,n] = \frac{I_2 - I_4 + I_1 - I_3}{I_2 + I_4 + I_1 + I_3}[m,n] \tag{4.13}$$

The Figure 4.5c represents the slopes in the X-direction on a 10×10 sub-apertures configuration, that can be compared to the slopes for 80×80 sub-apertures in Figure 4.5b. It can be seen on the graph that the slope determination is working, although the smallest features are not well detected.

4.2.7. The Wavefront reconstruction with the CURED algorithm

Once the slopes per sub-apertures retrieved, it is possible to reconstruct the phase screen from these slopes. The three possible reconstructors are the CURED algorithm, the Zernike decomposition for an annular mirror or the only tip/tilt compensation by a tilting mirror. The tip/tilt reconstructor can immediately be removed as it will considerably the correction, only able to correct for the global tip/tilt of the system. For the Zernike decomposition, something that needs to be taken into account is that this decomposition is very good to reconstruct atmospheric perturbations. However here the disturbances come from the offsets generated by LGS WFS. Therefore, the use of the decomposition might not be adapted to the system.

The CURED algorithm, developed by the Linz University (Rosensteiner, 2012 [66]), aims at reconstructing the wavefront precisely as fast as possible. The current reconstructors scale in complexity with $O(n^2)$ where n is the number of sub-apertures. This becomes a problem with the increasing number of actuators for the ELT, where $74 \times 74 = 5476$ will be used. The reconstruction process will take too much time and is not adapted to the desired frequency of the system $\approx 1kHz$. Some solutions have been found, with for example FFT-based reconstructors that have a complexity degree that scales with $O(n \log n)$ or the CURE reconstructor that scales with $O(n)$. This is the current reconstructor that is planned for the ELT, mainly because in addition to the decrease complexity compares to a vector-matrix-multiply reconstruction, it still allows parallel operations (which is not the case for the FFT-based reconstructor for example). Let's describe the principle of the CURE algorithm (Rosensteiner, 2011 [65]). The basis of this algorithm is, starting from the initial wavefront phase of 0, to propagate the state in one direction and compute the trending line in the other direction. The trending lines can be considered as the mean of the values in the other direction, which defines the "global" value the object will have. In the end, the trending lines are added to the phase obtained with propagation, to create the chains in the x- or y-direction. A mean of these two chains is then made to compute the global phase map.

So first, propagating the state starting from $I_x[0,:] = 0$, the initial point:

$$I_x[i+1, j-1/2] = I_x[i, j-1/2] + S_X[i, j-1/2] \tag{4.14}$$

Then, the trapezoidal mean values can be computed from this state:

$$w_x[j-1/2] = \frac{1}{N_{sub}} \left(\sum_{k=1}^{N_{sub}-1} I_x[k, j-1/2] + \frac{1}{2} I_x[0, j-1/2] + \frac{1}{2} I_x[N_{sub}, j-1/2] \right) \tag{4.15}$$

And this mean can be removed from the state propagated so that the mean of the state is equal to 0. The interest here is that the mean value will then be set to the desired value, here set by the trending lines.

$$I_{x0}[i, j-1/2] = I_x[i, j-1/2] - w_x[j-1/2] \tag{4.16}$$

Now the trending lines can be computed, with the first trending line equal to 0:

$$t_y(j) = t_y(j-1) + \frac{1}{N_{sub}} \sum_{i=1}^{N_{sub}} S_Y[i, j] \tag{4.17}$$

Once the trending line computed on the points, the intermediate points can be computed by doing the mean between the other points:

$$t_y[j+1/2] = \frac{1}{2}\left(t_y[j] + t_y[j+1]\right) \tag{4.18}$$

Finally, the phase ϕ_x can be computed, so that the mean value of every chain is the trending line:

$$\phi_x[i, j-1/2] = I_{x0}[i, j-1/2] + t_y[j-1/2] \tag{4.19}$$

The same method can be applied for computing ϕ_y, using the slopes S_Y for the expansion and S_X for the trending lines. The finale phase map is calculated by doing the mean sum of the two.

$$\phi[i, j] = \frac{1}{4}\left(\phi_x[i, j-1/2] + \phi_x[i, j+1/2] + \phi_y[i-1/2, j] + \phi_y[i+1/2, j]\right) \tag{4.20}$$

The significant drawback of the algorithm is the strong increasing noise propagation in case of large apertures, which will be the case with the ELT. The improved algorithm CuReD that includes a domain decomposition deals successfully with this (Rosensteiner, 2012 [66]), as the cost of a slight decrease in computational speed. The principle of the algorithm is to split the phase screen into sub-divisions (cf Figure 4.6b) and apply the CURE algorithm on every sub-divisions.

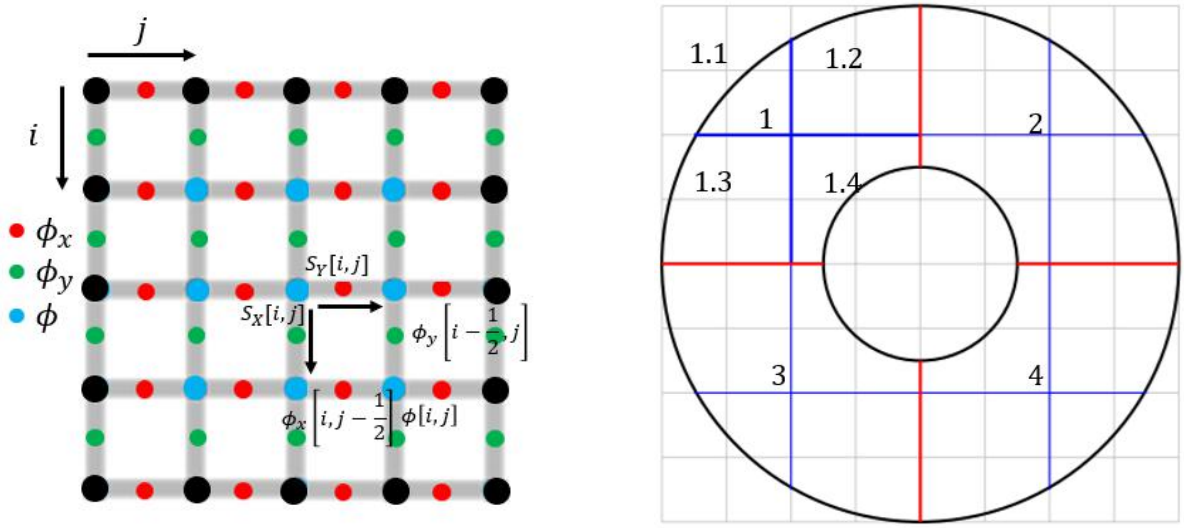

(a) Layout of the phase and slopes for the CURE algorithm

(b) Sub-division made by the CURED algorithm

Figure 4.6: Schema of the CURE and CURED algorithm

Once the CURE algorithm applied on the subdivisions, these subdivisions can be linked together by computing the link:

$$d_{ij} = \|\phi_j[*, first]\| - \|\phi_i[*, last]\| \tag{4.21}$$

And these links can then be added to the phase computed on each subdivision:

$$\phi_2 = \phi_2 + d_{12} \tag{4.22}$$

$$\phi_3 = \phi_2 + d_{13} \tag{4.23}$$

$$\phi_4 = \phi_4 + d_{12} + d_{24} \tag{4.24}$$

This algorithm can be applied recursively, so that each subdivision can be again sub-divided, and reconstructed in a similar process. The more subdivisions, the highest performances for the system. The number of subdivisions used in the algorithm has been set to 2, like what is presented in Figure 4.6b. A higher number

n would decrease the computational speed and put too many constraints on the number of subapertures, which will have to be multiples of 2^n. The final result of the reconstruction process can be found in Figures 4.7b and 4.7c.

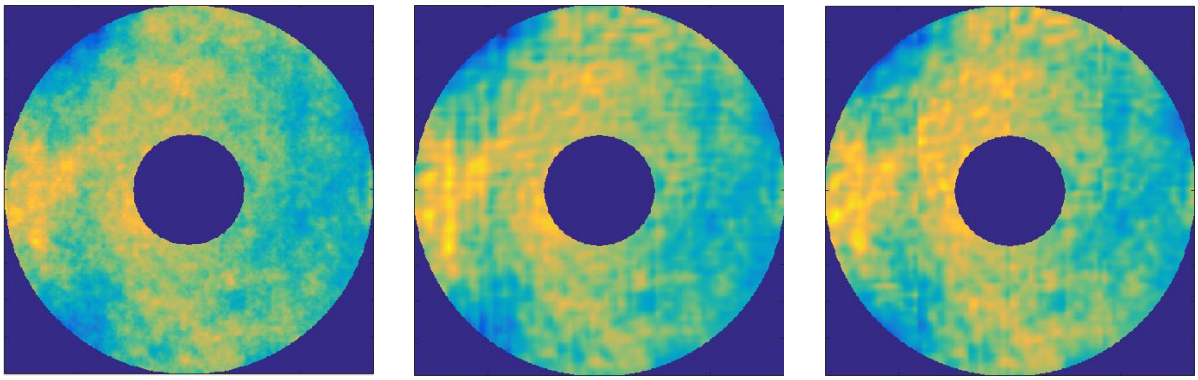

(a) The original wavefront screen (b) CURE algorithm (c) CURED algorithm

Figure 4.7: Comparison between the original wavefront screen and the reconstruction found with the CURE and CURED algorithm (for 80×80 subapertures)

As it can be seen, the difference between the algorithm is tiny, the CURE algorithm being even more precise than the CURED one for real cases. The main advantage of the CURED algorithm lies when the noise becomes more important. Although measurements in some location are not precise, the property of dividing the pupil in sub-division limits the propagation of this noise, so the global trending lines are less affected by the problem. However the results are not convincing here, and the CURE algorithm has been used for the simulations. The implementation might be erroneous, or the number of sub-divisions taken not important enough.

4.3. Results

Now that the algorithm has been explained, some results can be found in this section.

4.3.1. The determination of the NGS magnitude

As it can be expected, the noise implemented will have a direct consequence on the limitation of the guide star magnitude. When the noise is too significant, the wavefront estimation becomes impossible, and the system starts not only to not correct the atmospheric perturbations, but also adding more errors. This limiting magnitude has a direct consequence on the Sky coverage, as it will be explained in 8.

The calculation of the limited magnitude for the natural guide star can only be done by complete simulations, but throughout the project, it has been noticed that a signal to noise ratio of at least 1 is required to perform the correction. With analytic formulas, it is possible to asses a first estimation of the magnitude range. The reasons for these are:

- A verification of the truth sensing system. If the SNR is supposed to be very high for a given NGS magnitude and if the system does not provide a stable correction, it might be the consequence of implementation errors inside.
- This method allows to analytically asses which configuration is the most constraining for the NGS magnitude, between the truth sensing and the Tip/Tilt sensing.

Let's see for example how the SNR evolves over the magnitude range. The global signal to noise ratio can be expressed as (Gonzalez and Woods, 2008 [30]):

$$SNR = \frac{\sum_{i=1}^{N}\sum_{j=1}^{M} \hat{I}^2[i,j]}{\sum_{i=1}^{N}\sum_{j=1}^{M} \left(I[i,j] - \hat{I}[i,j]\right)^2} \tag{4.25}$$

Here I represents the signal with noise while $\hat{I}$ represents the signal without noise. To plot the graphs in Figure 4.8b, the signal to noise ratio taken is the one from the comparison between the slope in the X-direction and the same slope but with the noise added. The data used come from the direct measurements of a residual, with a NGS brightness that is adjusted relatively to the simulation's needs. The noise implementation is the same as the one for the loop, in addition to the filtering performed at the end to remove the constant sky background noise. The results for the Truth Sensing can be found in Figure 4.8a. The two configurations that are interesting us are the Tip/Tilt configuration and the Truth sensing one. It could be interesting to determine which one is the more demanding for the NGS brightness.

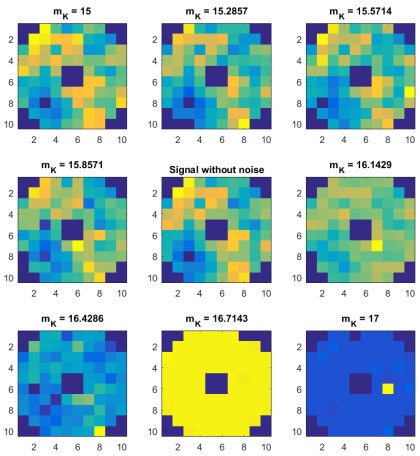

(a) Signal S_X measured by the Truth Sensing for several magnitudes. The reference image is located in the center.

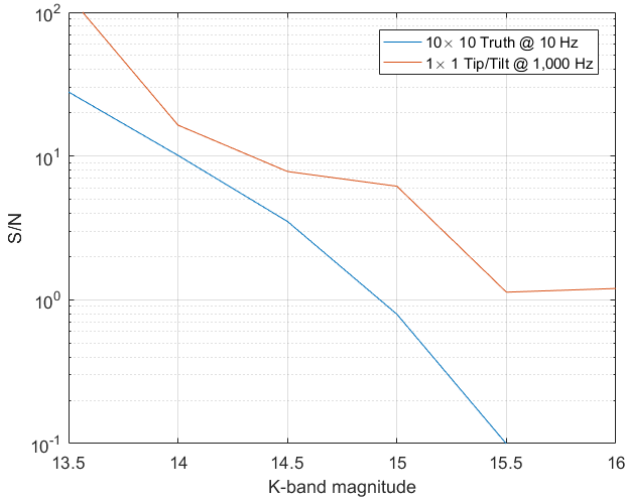

(b) Representation of the Signal to Noise Ratio for different configurations for the PWFS

Figure 4.8: Representation of the noise impact on the slopes measured and the Signal to Noise Ratio

With the SNR calculated as in the Equation 4.25, by doing Monte-Carlo simulations with 1,000 iterations, the Figure 4.8b can be created. The interpretation from the plot is that the truth sensing is more demanding than the Tip/Tilt sensing regarding NGS magnitude. However, the estimation of the SNR is not very precise, even for 1,000 iterations. The tendency remains the same, but the differences between the two might be less than the one observed in the figure. About the limiting magnitude, an observation of the Figures 4.8a and 4.8b reveals that the limiting magnitude might be between 15 and 16 mag_K. The limiting magnitude refers here to the maximum magnitude at which the system remains stable.

4.3.2. Performances estimations

As it has been stated before, the number used to measure the resolution performances of an instrument commonly used is the Strehl ratio. To be able to estimate the performances of our system, a Strehl estimation has been created in the simulator. The two solutions that have been foreseen are presented here. To accomplish this, diffraction limited PSF is generated by the same procedure described before, except that the atmosphere is completely flat in that case (no phase variations). This PSF is then normalized to its total so that the total amount of energy in the perfect PSF and the long exposure one is the same. The long exposure PSF is created by adding the short exposure PSFs generated by the algorithm at every iteration by the algorithm. It is possible to skip a certain amount of frames at the beginning to increase the Strehl ratio (waiting for the system convergence).

Calculation by maximum comparison

The first possibility would be to compare the maximum of the PSFs, as it is stated in the Strehl ratio definition (Roddier, 2004 [64]). This technique has a major disadvantage: the maximum for a PSF highly depends on the resolution at which it is sampled, especially for comparing high-Strehl PSF. It was not uncommon to obtain Strehl ratio higher than 1 when testing the system with this method. However, for medium/low-Strehl ratios (typically below 90%), the estimations become closer to the reality. To completely calibrate the estimation,

the Strehl ratio is calculated on both the corrected and uncorrected PSF. The uncorrected Strehl ratio is given by the YAO system. So the final Strehl ratio of the system can be found as:

$$S = S_{corr} \times \frac{S_{YAO}}{S_{uncorr}} \tag{4.26}$$

In that case, the Strehl ratio can be compared to the one obtained with YAO, as it is "normalized" by this factor.

Comparison of areas

This one comes from an approximation of the Strehl ratio based on the shape of the PSF, which is:

$$A_{tot} = S \times A_{dif} + (1 - S) \times A_{atm} \tag{4.27}$$

where A_{dif} represents the area for the PSF of the diffraction limited PSF, while A_{atm} the one for the seeing limited one. The principle is simple: the image of the PSF is cut in the X-direction for example, at the location of the maximum intensity for the Y-direction. Then the position of the first and last points whose values are a N^{th} of the maximum is determined. The number N can be modified; it is for the moment set to 1/2. The area is then calculated inside these points and outside, which gives respectively A_{dif} and A_{atm}. For A_{atm}, the atmosphere between the points x_{min} and x_{max} is approximated as $(x_{max} - x_{min}) \times max(PSF)/N$. While being a small under-evaluation of the real value, this remains relatively accurate since the seeing limited PSF is spread over a large number of pixels.

4.3.3. Atmospheric correction by the truth system

The system presented before can correct for the residual provided from YAO, for almost any sodium layer profiles:

- For the profiles that were already giving a Strehl ratio of 60%, the benefit of the truth sensing is minimal as a 10×10 subapertures at 10 Hz configuration is not able to provide sufficient correction to obtain a Strehl high than that.
- For the THWP profile, the problem is that the main Strehl loss was caused by the total loss of wavefront information for the sub-apertures located in the opposite side of the LLT. For this reason, the truth sensing was not able to correct for this effect

For the other cases, the correction brought by the system is quite good. It is difficult to quantify the improvement appropriately, as the performances estimation defined earlier does not seem to work. However, a visual comparison is still possible and clearly shows that improvement has been made.

In Figure 4.9, both PSFs contain the same amount of energy, and it can be seen that the maximum for the corrected on is almost twice as important as the maximum for the uncorrected one. The Strehl ratio has been here approximately been doubles, which means that the final Strehl can be estimated as 50%.

On the Figure 4.10, it can be seen that the residual is adequately corrected by the system. The remaining residual is homogeneous, meaning that there are no more residual patterns created by the sensing.

4.4. Recommendations

Some recommendations can be made after this work:

- First of all, it seems that the performances estimations are more complicated than what it seems. The three methods presented give completely different results, and it is, therefore, hard to evaluate the performances of the truth sensing. A visual analysis of the PSF, as it can be done with Figure 4.10, tends to show that the performances are indeed improved by such a system. But hard numbers would still be required, ones that can be compared to end-to-end YAO simulations for example.

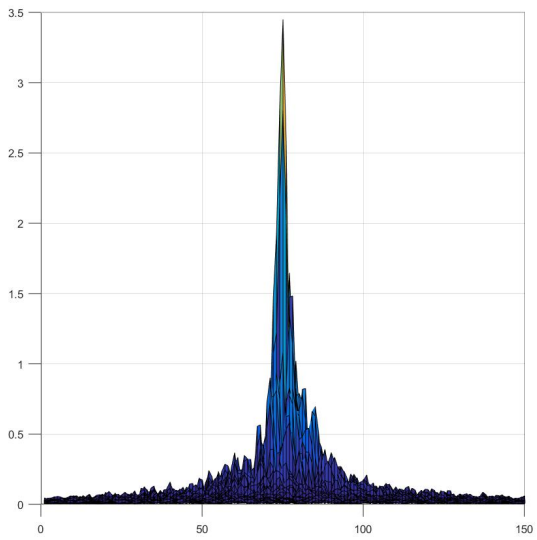

(a) PSF recovered from the YAO simulations

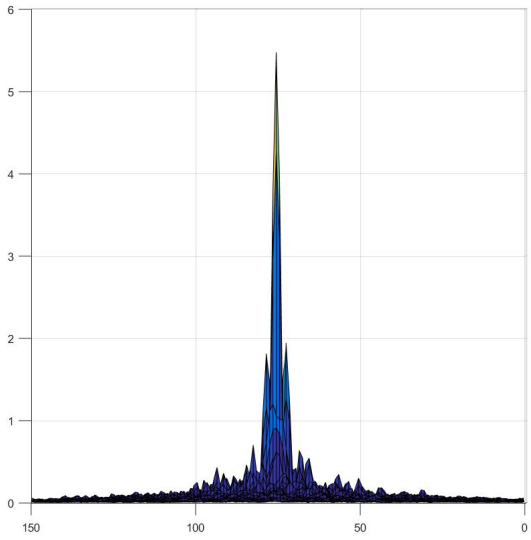

(b) PSf obtained after the residual correction in MATLAB

Figure 4.9: Comparison between the PSF obtained before and after correction for a VW sodium profile, correction by a 20 × 20 truth sensing at 10 Hz

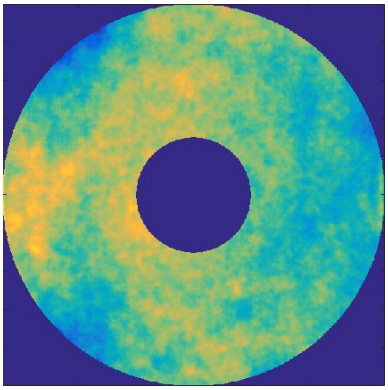

(a) Residual map imported from YAO

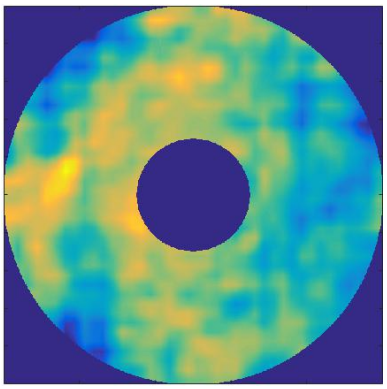

(b) Wavefront correction brought by the mirror (20 × 20 sub-apertures)

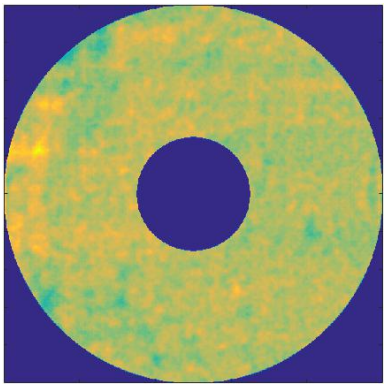

(c) Residual from the subtraction between the mirror and the residual

Figure 4.10: Correction brought by the MATLAB AO system on the residuals

- Second, some assumptions has been made that might not be entirely true. For example, the sky median value is directly used, instead of the simulation of the chopping. This leads to an underestimation of the sky noise, which makes the results found a little bit optimistic.

Conclusion

The purpose of this part was to demonstrate that the features created by the sodium profile could be corrected by what is called the "Truth Sensing." The principle of this method is to use the SCAO PWFS already integrated into METIS to correct for these fixed patterns. The possibility to run the PWFS at a much lower frequency (10 Hz*) and to bin them together (* 10 × 10*) will considerably decrease the requirements on the NGS brightness. An algorithm has been written in MATLAB, simulating the behavior of a PWFS acting as this truth sensing, using the residuals that have been generated by the simulator YAO. This part has proved that the configuration described before would be able to correct partially for the residuals, increasing the Strehl ratio substantially. However, the estimation of this increase is difficult to determine, because of the lack of precise performance assessors.*

Chapter 5

Simulation of the ELT/METIS performances with the SLAO system

AO systems are incredibly complex, and lots of parameters need to be taken into account to obtain realistic results. Some codes have been provided by NASA, ESO or even Caltech to try to simulate the performances of a given AO system. It is important to note that the codes need to be in constant evolution, as new systems such as Laser Tomography AO or Multi-Conjugate AO appear and require new operations and optimization to be run in a reasonable time. This part will detail the specifications of these codes and explains how they have been used during the project to simulate the performance of the SLAO system for the ELT/METIS.

Contents

5.1. The YAO, COMPASS and OCTOPUS simulations

This part will briefly present the characteristics of the simulation to underline the main reasons why the results obtained from them could be different.

5.1.1. YAO

The Yorick Adaptive Optics simulation is a Monte-Carlo simulation tool that has been developed in YORICK. This language is similar to MATLAB or IDL. The core of the program is coded in C to increase the speed. This simulation is in open-source. The software is using custom functions for the several parts of the AO system such as the WFS or the DM. For this reason, it is easy to use a custom set-up for the software that completely fits the characteristics of the system that is simulated. The fact that it is in open-source is also an advantage since it is still under development as new features are added to fit the unique requirements of the new AO systems.

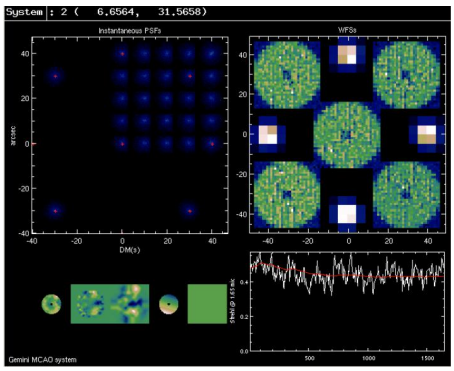

(a) YAO layout for a standard simulation

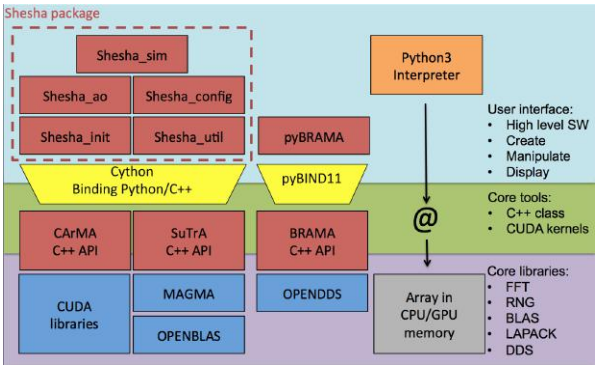

(b) The COMPASS architecture: the upper layer with the Python interface, the medium one with the C++ and CUDA softwares for the velocity and the lower layer that controls the GPU.

Figure 5.1: Presentation of the common simulators used for AO simulations

5.1.2. COMPASS

The COMputing Platform for Adaptive optics SystemS has been developed to provide a full-scale end-to-end AO development platform to simulate the future performances of the ELT. The core can be used as a test and integrated on a real system later. The system is also used to develop a prototype that will be used for high speed, low latency, image acquisition and processing system dedicated to AO systems and fully integrated into the simulation framework. The primary investigators of this project are the PHASE (Partenariat Haute Résolution Angulaire Sol et Espace) that gathers the most important French AO community. It includes LESIA, the Paris Observatory, GEPI, ONERA, LAM, IPAG or the "Maison de la simulation." The system's interface is based on the Python language, which relies on several layers of software. The architecture of the software can be found in Figure

This simulator has quickly been abandoned because of its incapacity to deal with PWFS and SH-WFS at the same time, which is mandatory here for the SLAO simulations. Moreover, the access to the system was more obscure, as it has been created by a single entity and not by several persons as it is the case for YAO. However, the first SCAO simulations have used this tool to confirm that results were similar between YAO and COMPASS.

5.1.3. OCTOPUS

Finally, the OCTOPUS simulator is an end to end AO simulation tool that has been developed by ESO, the European Southern Observatory. The simulation respects the process of an Adaptive Optics system: the input is created by passing it through evolving random phase screens, sensed by the WFS that calculates the amount of correction needed to compensate for this distortion. The Deformable Mirror(s) (DM) shape is changed relatively to the command. The output is the PSF obtained, with relevant parameters such as the Strehl ratio, encircled energy. This method follows the physic of what happens in a real AO system, which makes the simulation accurate but also slower. To accelerate the simulation, the operations are fully parallelized and run in several clusters at ESO.

This software was not accessible directly during the project. However, ESO only believes in performances from simulations that have been conducted by Miska Le Louarn with OCTOPUS. To confirm the results ob-

tained during the first months, the set-up of the simulations performed in YAO have been written and sent to ESO to compare the results.

5.2. Setup for the simulation in YAO

The input parameters are stored in a '*.par' file. This file is then read by the YAO algorithm for the simulation, with the command *aoread*. The initialization of the system is then done (interaction matrix computation) with *aoinit*. Finally, the number of iterations *loop.niter* is selected and the loop launched with *aoloop* and *go*. The simulations that will be presented here has the architecture that can be found in Figure 5.2.

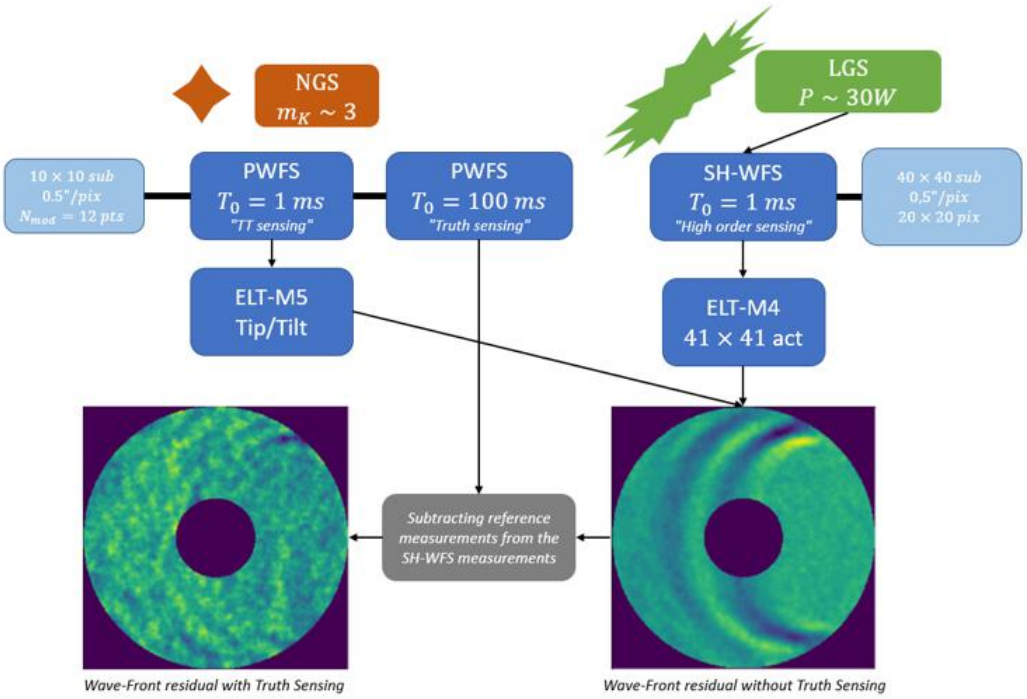

Figure 5.2: Architecture of the YAO simulation

The simulations with the LGS and the tip/tilt sensing have been made directly in YAO. Here, the SH-WFS presented in Chapter 3 will correct for the high-order perturbations, whereas the PWFS will adjust for the tip/tilt. However, the correction made on the wavefront residual with the truth sensing ("subtracting reference ...") is not made directly in the software, but with a MATLAB simulator that has been presented before.

It is important to emphasize that the parameters found here are a consequence of hundreds of trials and errors. Every choices made will be justified or have already been in Chapters 3 and 4.

5.2.1. The simulation structure

The simulation structure contains the pupil diameter*pupildiam* in pixels. This value has been chosen so that it samples well the turbulence structure. For example in the L-band, $r_0 \approx 1.33\ m$ thus it has to be sampled MINIMUM 3-4 times per r_0, with a pixel size of $\approx 0.3\ m$. Since the telescope diameter is 37-meter large it means that the number of pixels for the aperture can be approximated as $pupildiam = 37/0.3 \approx 160\ pix$ in case of good seeing. For a bad seeing, the pixel size could be doubled to 320 pix. However, in that case, the FoV of the simulation will only be enough to sample well the PSF, and not the one desired. And in most of the AO simulations, the FoV considered is extremely important for the system performances. This FoV directly depends on the number of pixels in the pupil diameter. Which means that for simulating large FoV, the *pupildiam* parameter will be very high which will considerably increase the computation time of the simulations.

$$FoV = \lambda/D \times pupildiam\,(rad) \tag{5.1}$$

In this case $\lambda = 0.5892\mu m$ for the LGS sensing, $D = 37\ m$. If a FoV of 10" is required for the system (see chapter 3), it means that the $pupildiam \approx 3080\ pix$. Since the computation time of the simulation is directly linked to this parameter (the FFT scales $\propto n\log n$ where n is the size of the image on which it is applied for example), increasing the number of pixels will increase the computation time of the system. A tentative was made to use the $extendedfied$ keyword provided by YAO. This function was supposed to be a tool for simulating large FoV without having to use large numbers of pixels for the pupil sampling. Several hours have been spent to try to make this work (the reward would be a computation time divided by ≈ 4), but they have been unsuccessful. The main reason is that this method convolutes the Kernel created in the small FoV (2") to adapt it to the extended one. However, the beam is so elongated (and therefore cropped by the 2" FoV) that the result of the convolution is completely erroneous. Several tries have been made with larger FoV, up to 7.5" for the small one and 10" for the extended one. However, the results were still not as great as for a 10" FoV without using the extended field, and this has been abandoned.

Since the system will also use Pyramid WFS, the number of pupil diameter pixels must be a multiple of the sub-aperture number. In the case of the SLAO simulations, the Truth sensing is made by the 74×74 PWFS of the SCAO, binned into a 10×10 PWFS. The Tip/Tilt sensing is made by binning the PWFS entirely into one single sub-aperture.

5.2.2. The Atmospheric model

The atmosphere's phase screen is already created and can be found under the name *screen*. The creation of these phase screens needs to be done very carefully: it is important to take the same parameters as the one globally used by ESO and for the METIS SCAO system so that the results found during the simulations are comparable. To create these screens, the outer scale L_0 must be specified in pixels. Under the Armazones conditions (Marchetti, 2015 [49]), the outer scale is estimated to $L_0 = 25\ m$. If for example the 37-meter pupil's diameter contains 3080 pixels, it means that the outer scale will be $L_0 = 3080 \times 25/37 = 2081$ pixels. The seeing conditions can be modified by the telescope diameter to Fried's parameter ratio $D/r_0 = dr0at05mic$, in addition to its altitude, speed and fraction *layeralt,speed,frac*. The Fried's parameter taken is $r_{0,0.5\mu m} = 0.157\ m$ corresponding to a seeing of ≈ 0.64" (Marchetti, 2015 [49]), which makes $dr0at05mic = 235.7$. This corresponds to standard seeing conditions. Finally, something essential is the number of layers that will be used to simulate the atmospheric perturbations, and their relative contribution, altitude, and speed. The data that have been taken is the one for median seeing conditions. The wind distribution and the relative importance of the layers can be found in Figure 5.3.

The high layers, although not very important in terms, are the ones that have an impact on the "cone" effect since they are not well sampled by the LGS signal. Assessing precisely the performances of the system thus require to know well the behavior of the atmosphere at high altitude. For this reason, the ESO model is composed of 35 layers at a maximum height of 26.5 km.

5.2.3. The Wavefront Sensors

The wavefront sensor structures represent the solutions that have been found for sensing the incoming perturbations in the ELT/METIS. For a simulation with an SLAO system, three types of sensors are required for the low and high order modes sensing:

High-order sensing For the high-order modes, the LGS will be used with the associated SH-WFS. Here the wavelength of data acquisition is equal to $lambda = 0.5892\mu m$. The magnitude of the LGS can be computed with the $laserpower = 30\ W$ and the $lgsreturnperwatt = 22\ phot/cm^2/s$. The laser will be launched from the side of the telescope, so the corresponding parameter has been set to $LLTxy = [18.5, 0.]$. The values put here are standard and represent what can be expected from such a system. The sky magnitude in the V-band is set as 21.83 $mag/"^2$, which is also something common that can be found in normal seeing conditions per Marchetti, 2015 [49]. The noise from the detector has been set to $ron = 1\ e^-$, $darkcurrent = 500\ e^-/s/pix$ and optical transmission to 0.56. Finally, since it is impossible to detect the Tip/Tilt (Tyson and Frazier, 2012 [78]) with a LGS, the parameter *filtertilt* is set to 1. For the input specifics to the SH-WFS, the *shmethod* chosen is the *geometric*. The number of subapertures in telescope diameter is equal to $shnxsub = 40$. Something fundamental to consider

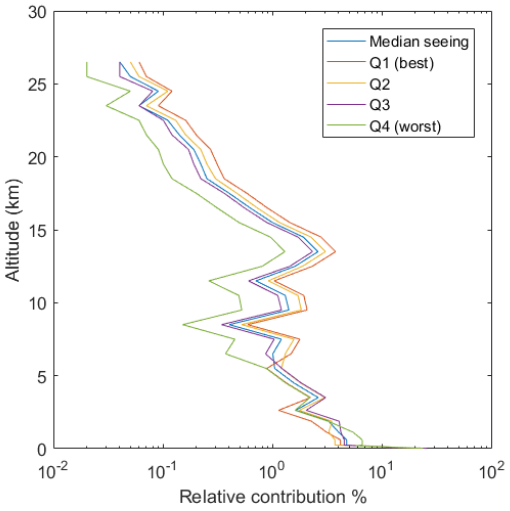

(a) Distribution of the atmospheric layers relative contribution

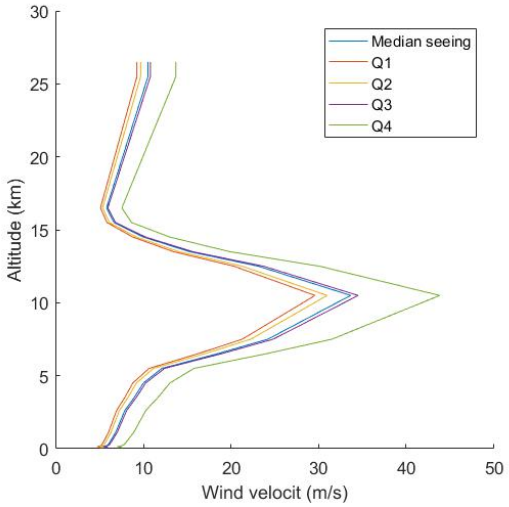

(b) Distribution of the wind velocity

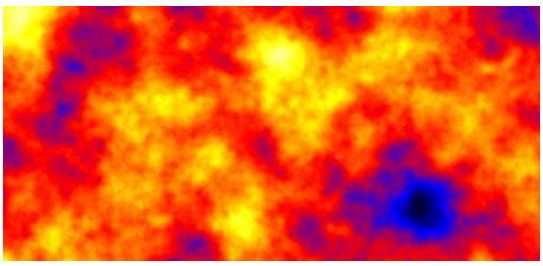

(c) An atmospheric screen generated by YAO. Color code represents the difference in path generated by the atmosphere

Figure 5.3: Atmospheric parameters considered in the YAO simulation (Marchetti, 2015 [49])

is the spot elongation because of the Laser Launcher Telescope located at one edge of the ELT. The recommendation discussed in chapter 3 for the size of the sensor is to use a 40×40 SH-WFS, with a pixel size in the focal plane equal to $pixsize = 0.5"/pix$ and a number of pixels per subaperture $npixels = 20$. That makes the total FoV of the system equal to 10", as it has been explained before. As it has been seen before, the sodium layer distribution is also crucial for the performances. The guide star altitude is set to $gsalt = 90\ km$, its depth to $gsdepth = 10\ km$ and its position to $gspos = [0", 0"]$ since the LGS will be directly on the science object to limit the anisoplanatism. These two parameters would generate a Gaussian function, with the peak located at the guide star altitude and a full width of half maximum close to the depth set. However, Pfrommer and Hickson, 2014 [57] have shown that this is a very optimistic case, only true $\approx 30\%$ of the time. Some profiles have thus been created in MATLAB from the graphs given in Pfrommer and Hickson, 2014 [57] and added directly to the YAO file by setting the lgs_prof_amp and lgs_prof_alt.

Tip/Tilt sensing For the low-order modes, the idea is to use the SCAO Pyramid WFS with the pixels binned together. However, since the binning is not possible in YAO, the idea is to set a PWFS directly with the desired number of subapertures. The performances regarding the NGS magnitude might be affected by this. However, the magnitude simulations will mainly be done with the MATLAB simulator, so this assumption remains valid for bright NGS. This sensor will be directly linked to the TT mirror. The number of subapertures along the pupil diameter is set to $shnxsub = 10$. The number of pixels per subaperture is configured so that $pupildiam = npixpersub \times shnxsub$. The wavelength of sensing is in the K-band, so that $lambda = 2.2\mu m$. The Natural Guide Star magnitude will be set to a standard value for TT sensing, which is $gsmag = 10\ mag_K$. The sky magnitude in the K-

band is equal to $skymag = 12.9\ mag/"^2$. The Read Out Noise is set to $RON = 1\ e^-$, the dark current $darkcurrent = 430\ e^-/s/pix$ according to the characteristics given in Selex, 2014 [71]. The position of the guide star is set in the FoV's center, so that $gspos = [0",0"]$. This assumption might be wrong in reality. However, since the anisoplanatism effect is very small for low order modes (especially Tip/Tilt sensing), the results remain valid. The guide star's altitude is at infinity, so that both*gsalt* and *gsdepth* are set to 0. For the modulation amplitude and number of points along the modulation circle, they are set to $pyr\_mod\_ampl = 4 \times \lambda/D = 0.05"$ and $pyr\_mod\_npts = 12$, with the location of the modulation *pyr_ mod_ loc* set to *"after"* the field stop, following the recommendation of the set-up for the SCAO simulations that has already been made (Cantalloube et al., 2017 [18]).

Truth sensing The implementation of the Truth sensing will be explained more in details later in the chapter. The configuration is the same as the TT sensing one since in reality the signal that will be used for Truth and TT correction will both come from the METIS-SCAO PWFS. However, because of software limitations, the SH-WFS had to be used in a 10×10 configuration with 2×2 pixels per sub-aperture. However, the value of noise, wavelength, guide star magnitude remains the same as for the TT sensing.

5.2.4. The wavefront correction structure

The correction structure is here composed of a deformable mirror and a tip/tilt mirror:

M5-Tip/Tilt mirror This steering mirror as the $type = "tiptilt"$. Its conjugation altitude is set to $alt = 0$ since it corrects relatively to the NGS sensing.

M4-DM This Deformable Mirror is in reality composed of void-call actuators, but they are not available in the simulation. Therefore the closest set up has been chosen, which is the "$stackarray$" type. The conjugation altitude of the mirror is set at $alt = 0$. The number of actuators for this mirror is one more than the number of sub-apertures for the high-order WFS, which is equal to 41.

Mat Once the wavefront slopes measured, it has to be converted to a consign sent to the actuators. It is important to separate the contributions of the different systems, which is by putting $mat.condition$ =&([15.,15.]). If only a single vector value is put inside, the system will not separate the contributions from the WFSs, and the information from the NGS will be used to "help" the LGS system.

5.2.5. Other properties

This represents the loop properties such as the loop frequency or the position of the guide star and the target.

Telescope In this part, the telescopes characteristics are entered. First the diameter, which is for the ELT of $diam = 37\ m$. The central obscuration/ telescope diameter ratio is also set, here equal to $cobs = 11.1/37 = 0.3$. Vibration parameters can also be added, which is not the case in the simulations presented here.

Target The science object that needs to be observed is also set. Here the simulation will be made in the L- and N-bands, so the wavelength will be equal to respectively $lambda = 3.7\mu m$ and $lambda = 10\mu m$. The target is assumed centered in the FoV.

Guide Star The natural guide star structure is set here. The photometric zero point magnitude is equal to $zeropoint = F_0 \times \pi D^2/4$, where $F_0 \approx 2.2 \times 10^{12} phot/s/m^2$ is the flux in photons for a $0-mag$ star in the K-band. The zenith angle is set to $zenithangle = 30°$.

Loop The loop properties can also be examined. The most important one is the gain of the loop, which as to be strong enough to be able to follow the atmosphere evolution and correct it but not too strong to prevent instabilities in the system. Following the recommendation from the SCAO system, the gain is set to 0.4. The number of iterations varies relatively to the purpose of the simulation. But the minimum set is 1,000 and the maximum 5,000 since 1,000 takes approximately $24h$ to be completed. The system has a loop frequency of 1,000 Hz, and 2 frames of delay. These frames correspond to the exposure time of the WFS, and the processing of the information recovered to apply them of the mirrors.

5.3. Implementation of the Truth Sensing directly in YAO

The chapter 4 was presenting an implementation of the Truth sensing simulator in MATLAB, because of the lack of such a tool in YAO or COMPASS. But wouldn't it be possible to create a Truth sensing directly implemented inside YAO? This solution might be time-consuming but could offer "real" simulations. This section presents the problematic, the solution that has been considered and the tentative of this implementation.

5.3.1. The conflict between Wave-Front Sensors

One of the reasons why this implementation might be way more difficult than the one created in MATLAB is the possible conflicts between the sensors. In the case of sensors for the M4 and M5 mirrors, the system can be split into two parts with the tip/tilt WFS linked to the M5-mirror, and the LGS WFS linked to the M4 one. The Tip/Tilt is already filtered from the LGS WFS signal (physically impossible to measure), while the M5-mirror is in any case only able to correct the Tip/Tilt modes. However, if a truth sensing on a 10×10 subapertures is implemented, the correction sent will be directly applied to the M4 mirror, as the LGS WFS correction. An attentive study about the stability of the system needs to be conducted, in particular the gain applied by the truth sensing on the mirror. Even in that case, this will not solve the problem completely. The reason why truth sensing is required lies in the offset created by the LGS WFS because of the spot elongation. Which means that for a flat atmospheric perturbation, the WFS will see a distorted wavefront and send the consequent consigns to the actuators. The correction brought by the truth sensing WFS must be applied directly on the measurements: the offset must be compensated directly from there. Another solution would have been to apply the corrections on a "virtual mirror" M4*, that will not be visible by the LGS WFS but will be for the global Strehl ratio. In that case, there would be no conflict and the M4* would have only corrected the WF after the M4 and M5 mirrors. Although not realistic (adding a mirror in the instrument at this design stage is entirely impossible), this solution would have allowed us to quickly access the performances of the truth sensing without having to modify the YAO simulator code. This function is possible in COMPASS, where it is yet impossible to use WFS at a different wavelength and different types. Unfortunately, it is not yet possible in YAO.

5.3.2. The WFS measurements in YAO

The idea is then to use measurements from the NGS WFS that quantify the offset created by the LGS WFS, and subtract them from the LGS WFS measurements to compensate for the offset. The first thing to consider is that the number of sub-apertures is different for the LGS WFS and the truth sensing WFS. Thus the values cannot be subtracted merely individually. Second, a WFS cannot be created without a mirror linked to it. Thus, a virtual mirror with a gain equal to 0 has been established. This mirror will have no impact on the behavior of the AO loop. Third, the software YAO is sorting the measurements in its way, which is difficult to predict. The sub-apertures that are "too much outside the pupil" are directly removed. After this, the illumination of the subapertures (percentage of the subaperture on which the beam is impacting) is looked at, and all the sub-apertures with an illumination lower than a defined fraction are removed. The final measurement vector looks like this:

$$S_{mes} = \left[s_{x,1}, ... s_{x,n}, s_{y,1}, ... s_{y,n} \right] \tag{5.2}$$

where the first index corresponds to the first sub-aperture listed, and n the total number of valid subapertures. The size of the measurement vector is thus $2n$. At this point, it is difficult, even impossible to determine the precise position of a given sub-aperture k since it depends on several parameters that can change during the iteration process. Therefore, no accurate subtraction on the LGS WFS measurement can be made directly like this.

The solution is to use the coordinates of the sub-apertures, stored respectively as i_{start} and j_{start} as an attribute of the wfs object. They represent the upper left corner of the WFS pixels. After small minor manipulations, it is easy to represent the location of the valid sub-apertures as a $N \times N$ array, where N can be respectively 10 for NGS WFS and 40 for LGS ones. The main advantage of this technique is that the number of sub-apertures can be changed directly without modifying the code. The only problem with this method is that it the parameters i_{start} and j_{start} are only available for SH-WFS. Thus the implementation of the Truth sensing in YAO has been made with a SH-WFS, while it should have been done with the SCAO PWFS. Once the 10×10 tables created with the WFS measurements (one for y-slopes and one for x-slopes), they can be expended to 40×40 tables and subtracted to the LGS WFS measurements to correct the offset. Since the Truth

Sensing has an integration time of 100 ms, which is one hundred time the integration time of the LGS WFS, the measurements from the sensor will be 99% of the time equal to 0. The best solution is here to use what is called in YAO the reference measurements for the WFS $refmes$. They are created during the system calibration, and are subtracted to the signal at every iteration. Therefore, every time the truth sensing measurements are made, they are updated as:

$$wfs.\_refmes := wfs.\_refmes - truth_{mes} \times G_{truth} \tag{5.3}$$

where G_{truth} represents the gain applied by the truth sensing. The gain must be adjusted to improve as much as possible the performances of the system.

This method did not bring any relevant results, as the correction performed by such a system was not visible in the YAO results. The implementation might be erroneous, or the gain not well adjusted. Given that every trial was taking one full day to be tested, the elaboration of the direct correction has been abandoned, changed by the one implemented in MATLAB from Chapter 4.

5.4. Results from YAO

Here the results of several types of simulations are going to be presented. The point is here to identify the source of the errors and the limit of the correction.

5.4.1. Configuration with only LGS, no elongation effect

This configuration is used a preliminary investigation of the cone effect, by assuming that the LLT is located in the middle of the first mirror. This is in reality not possible (the stabilization and weight addition on top of the ELT M2 mirror are critical), but it allows to dissociate the effects of the elongation of the beam from the other effects of the system, mainly the focus anisoplanatism so-called the "cone effect."

The system simulated is the one presented before, except that the laser launcher telescope coordinates are set to $LLT = [0.,0.]$. The sodium layer profile taken here was the one which produces the worst results with the effect of elongation, to emphasize that this effect is mainly caused by the location of the LLT.

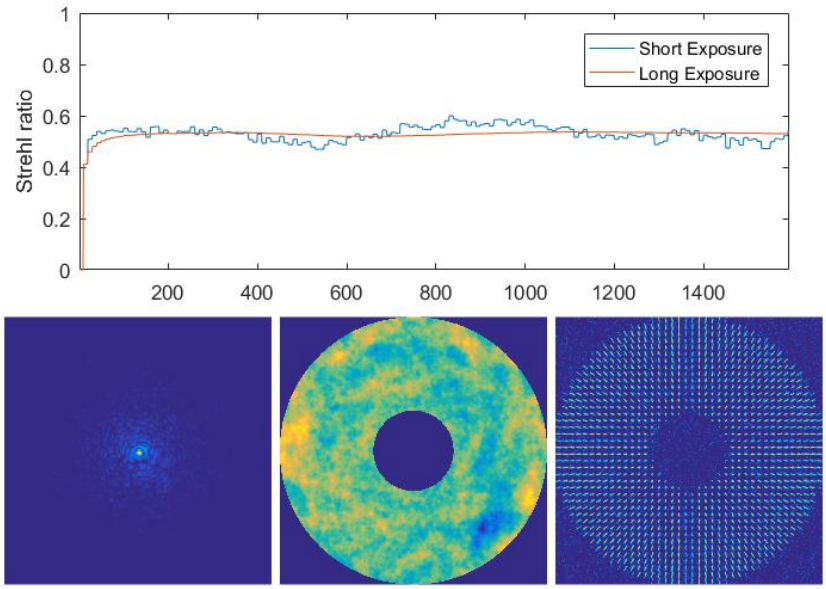

Figure 5.4: Results obtained with the YAO simulation: On the top can be found the Strehl evolution relatively to the number of iterations. Bottom left is the PSF obtained after all the iterations, bottom middle the residual phase and bottom right the WFS map for the LGS sensing.

The Strehl ratio obtained here is about 53% for the worst profile of sodium, whereas the optimal Gaussian profile provides performances of about 58%. These differences are way smaller than the ones when taking the elongation effects into account (cf Chapter 3). It means that the global loss can be attributed to:

- The cone effect, a consequence of the finite height of the LGS
- The fitting loss, because only a limited number of modes can be corrected for a 40×40 subapertures configuration.
- The temporal loss, because the atmosphere changes between two iterations, creating a delay between the correction and the actual wavefront.
- The tip/tilt error, created by the sensing and actuators.

What has been discovered during the literature study is that because of the outer scale L_0, it is almost impossible to estimate the effect of the focus anisoplanatism effect alone. End-to-end simulations are required, to take into account the structure of the atmosphere that is defined by this parameter. The formula found in Tyson and Frazier, 2012 [78] refers to the Strehl loss caused by this effect as:

$$S_\Phi = \exp(-\left(\frac{D}{d_0}\right)^{10/3}) \tag{5.4}$$

where $d_0 \approx 25$ refers to an atmospheric constant calculated with a formula found in Tyler, 1994 [76]. This leads to a Strehl ratio only by this effect of $S_\Phi \approx 10\%$, because the finite value of the outer scale has not been taken into account. The focus anisoplanatism effect seems to be in reality less important. Furthermore, this simulation also allows to clearly indicate that the use of 40 sub-apertures to sample the pupil is enough, as simulations with 80 have for example not shown significant improvements (since the focus anisoplanatism is dominating the wavefront errors anyway).

5.4.2. The LGS without truth sensing

These results have mostly been presented before in Chapter 3. The thing important to remember is that without truth sensing, the Strehl ratio seems to highly depend on the sodium layer profile.

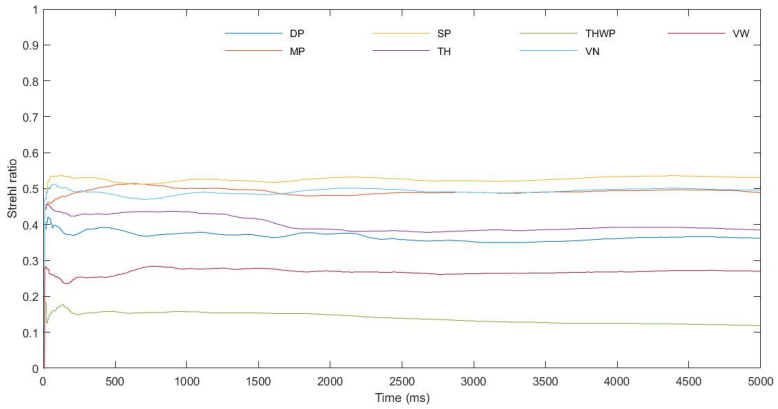

Figure 5.5: Evolution of the Strehl ratio according the the sodium profiles (see Figure 3.5)

As it can be seen in Figure 5.5, the results are quite stable. The only problem is that for "complex" sodium profiles, the global performances are below what could be expected, which is globally a 60% Strehl. Although the truth sensing seems not mandatory for profiles such as Single Peaks, Very Narrow or even Multi-Peaks (respectively SP, VN, and MP), other patterns such as Very Wide or Top Hat With Peaks (VW and THWP) create considerable losses in the Strehl ratio. Since the appearance probability of each profile is approximately 15%, the truth sensing appears as mandatory in $\approx 60\%$ of the time.

5.4.3. The LGS with truth sensing

As it has been stated before, the truth sensing implementation is YAO is hazardous. For this reason, the results presented here have been made with a combination of YAO and MATLAB simulation. Has it has been explained in Chapter 4, the YAO simulation has been used with a SLAO configuration, correcting the high-order modes and the tip/tilt at a frequency of 1,000 Hz. The residual wavefront has been saved every 100 iteration. From these residuals, MATLAB AO simulations have been performed with a homemade software to correct for the patterns remaining.

It has been difficult to assess the Strehl ratio performances with the simulation in MATLAB, as it has been explained in Chapter 4. However, based on the simulations that have been made, the fixed patterns seems to be corrected by the truth sensing, allowing a Strehl ratio around 60%. The reason why the Strehl cannot be further increased lies in the limit that has been discussed in the first configuration with no elongation effects: the focus anisoplanatism prevents the system from sensing some parts of the atmosphere, making the system blind for the upper layer turbulences. This limit is inherent to the SLAO configuration, and cannot be corrected with such a system. Several lasers would be required to obtain better performances, creating a tomography of the atmosphere (cf MCAO or LTAO).

5.5. Comparison with OCTOPUS

The European Southern Observatory will only believe results from simulations that they made on their own. Therefore, the configuration that was giving the best results in YAO was sent to their AO specialist Miska Le Louarn's so that the ESO's OCTOPUS simulator can be used.

The results from the simulations more or less agree with the results found with YAO. The configuration taken is identical to the simple configuration presented in the previous section. The information stated below are extracted from the ESO report that has been written for the project's review at ESO (Le Louarn, 2018 [46]).

- A SLAO system with no truth sensing and an ideal tip/tilt measured from the LGS. Even if in practice this setup is not possible because of the absence of tip/tilt in the LGS signal, this represents a first estimation of the cone effect, fitting, aliasing errors and temporal error. The Strehl obtained is 60,8%, which is similar to the one found in our simulation for this configuration. As it has been the case for the YAO simulations, the 40×40 sub-apertures configuration has been used. It has been noticed that increasing the number to 80×80 for example (as it is the case for SCAO) is not increasing the results. This has also been observed during the YAO simulations, leading to the optimal configuration presented.
- Then a simulation with the truth sensing has been added. For different reasons as for YAO, the pyramid WFS could not be used at the same time as the SH-WFS. Therefore, the study conducted is only relevant within the hypothesis of high NGS and LGS brightness, since a SH-WFS has been used instead. The reason is that PWFS and SH-WFS do not have the same behavior in case of low brightness signals, and differences might appear in these cases. The truth sensing is here running at 500 Hz, which is at the same frequency as the global simulation. The result is that the truth sensing is also partially correcting the cone effect since it is directly looking at the NGS. The correction provided by a 10×10 SCAO system has a Strehl ratio of 29%. The system is correcting for the low order modes, whereas the LGS system will correct for the high order ones. The Strehl ratio obtained with this configuration is slightly better than the previous one, 71.4%.
- Finally, the last configuration was obtained with a SLAO system with truth sensing, at a frequency of 10 Hz. This system represents the one that has been simulated with the combination of YAO and MATLAB. The performances observed at 60.8%, with a configuration that is stable for more than 4 sec (4,000 iterations).

These simulations, performed with another tool, show that the configuration and the simulations made at Leiden give realistic results. One might wonder why the performances of the system are the same with and without truth sensing. The reason is probably because the sodium layer profile used is idealistic: as it has been seen in Chapter 3, the profile of the layer used is a Gaussian. However, this profile only appears 30% of the time (Pfrommer and Hickson, 2014 [57]). The remaining profiles introduce offsets in the LGS WFS measurements, which are considerably decreasing the Strehl ratio. And that's where the truth sensing will be useful, as the MATLAB simulations made in Chapter 4 has demonstrated.

The results are of course not definitive, more precise simulations including the effects of bad seeing will need to be performed. Other things that are missing are a proper error budget since the WFS instruments will also display some errors that will need to be corrected. The value that is presented here can thus be considered as optimistic.

5.6. Recommendations for future simulations

Now that it has been established that the simulations performed during this project give approximately the same results as the OCTOPUS simulations made at YAO, several points need to be investigated more in details.

- The most important thing would be to implement a real truth sensing system in YAO, and not splitting it between a MATLAB and YAO independent corrections. The stability of the system is not tested at all here, mostly the relation between the LGS correction and the truth sensing. Although it seems that the solution was stable based on the OCTOPUS simulations, it could be interesting to launch the simulation for several minutes and see if the results remain the same.
- Something that also needs to be explored is the influence of the sodium layer variations with time. The problem here is that to simulate realistic changes, simulations of several tens of minutes are required, which would require with the current computation power 2 years for 10 minutes. More powerful computer or different set up could fix this problem. The present simulations made with a sodium layer changing 1,000 times faster than a real one displays considerable drops in performances. This part should thus be investigated more in details.
- The magnitude range is also something that needs to be tested in real time. The stability and performances found with the MATLAB algorithm might be only an estimation of the real ones. More precise values need to be found about the impact of the NGS magnitude with YAO full simulations, mostly the limiting magnitude. However, what is shown in Chapter 8 is that the wavelength range, transmissions, and emissions of the sky are not simple. Specific files need to be used for the calculation, which will require a YAO hacking to incorporate them, as the simulator is calculating everything within a particular band for now, with a flat transmission and sky emission.
- The telescope vibrations also need to be added in the system. In the case of the ELT, most of the tip/tilt influence will come from these vibrations. However, these errors are also slowly evolving, so their implementation and correction should not affect the performances of the system a lot.

Conclusion

This chapter summarizes the simulations that have been performed during the research project with the YAO tool. An optimization of the parameter space, coming from good knowledge about the physical phenomena to take into account, lead to a Strehl ratio of $\approx 60\%$*. This value is highly dependent on the sodium layer profile, but Chapter 4 has demonstrated that it would be possible to correct for the offsets generated, leading to overall performances of* 60% *Strehl. This value has been confirmed by the first ESO simulations. This first study has paved the way to more in-depth ones, with for example the investigation of the NGS magnitude influence on the performances.*

Chapter 6

Optical Design for the SLAO system

Now that the characteristics of the optical system have been described in Chapters 2 and 3, a first design has been elaborated in this Chapter. The primary purpose is to put first estimations on the size and required elements for the SLAO system, by creating a ZEMAX design. This design paves the way for further in-depth studies. However, although it might not be the best compromise, the way the system has been designed aimed to be as realistic as possible.

Contents

6.1. Preliminary design of the optical system

The purpose of this section is to define the characteristics of the SLAO system and its primary goal. These are the theoretical values, and they might be changed in the process.

6.1.1. Characteristics of the system

The characteristics that have been retained for such a system are:

- The number of subapertures will be equal to 40×40.
- The number of pixels per sub-aperture will be equal to 20
- The FoV used will be equal to 10", which means an individual pixel size of $0.5"/pix$.

Thus, the array used is similar to the LISA camera, which means a 800×800 pixels array with individual size of pixels of $24\mu m$. The total array size is thus 19.2 mm. Every subaperture will have a size of $20 \times 24\ \mu m = 0.48\ mm$. That represents a plate scale of $20.83"/mm$.

Considering that the primary aperture of the ELT is 37 m, one subaperture has a projected diameter of $37/40 = 0.925\ m$. Which means that the diffraction limit for such an aperture is $\theta = \lambda/d = 0.589\ \mu m/0.925\ m = 0.131"$. Since the pixel scale required is 0.5", it means that a pixel should be as large as $3.8 \approx 4$ diffraction limit. This is creating conditions on the focal length of the instrument. Since the pixel size will be approximately $4\times$ the diffraction limit, it means that the physical pixel size will be $4 \times 0.589\ \mu m \approx 2.4\ \mu m$. The required pixel size is

24 μm (see requirements of the SAPHIRA detector (Selex, 2014 [71])), so the f-number will be equal to 10. Since the entrance window of the object will be equal to 19.2 mm and there will be 40 sub-apertures, the lenslet size will be 0.48 mm. Which means a focal length of 4.8 mm for every lenslet.

Concerning the lenslet array, the size of the beam must always be the same. For 0° zenith angle, the size of the beam on the lens 500 mm after the folding mirror is ≈ 200 mm. At 60°, it is ≈ 65 mm.

6.1.2. Constraints for the pupil and LGS focus

To design the focus system and the SH-WFS properly, two things need to be well made:

- First of all, the system must be able to adapt itself to all the zenith angles. As it has been seen in Chapter 2, the distance between the telescope and the sodium layer changes relatively to the zenith angle. Since the SH-WFS lenslet array needs to focus the light beam coming from the LGS, the rays before this lenslet need to be collimated no matter the zenith angle.
- Another important part is that the measurements of the wavefront are made in the pupil plane. For this reason, the rays coming from the pupil need to be focused by the system directly on the lenslet array location, which will be able to image the perturbation. If the pupil rays would not be focused, the system will not be able to see the atmospheric perturbations since the "focus" modes will be considerably predominant. The pupil is represented by the first aperture of the telescope, which is the primary mirror.

Schema of the system

The specifications that have been presented before can be solved with a system such as the one shown in Figure 6.1.

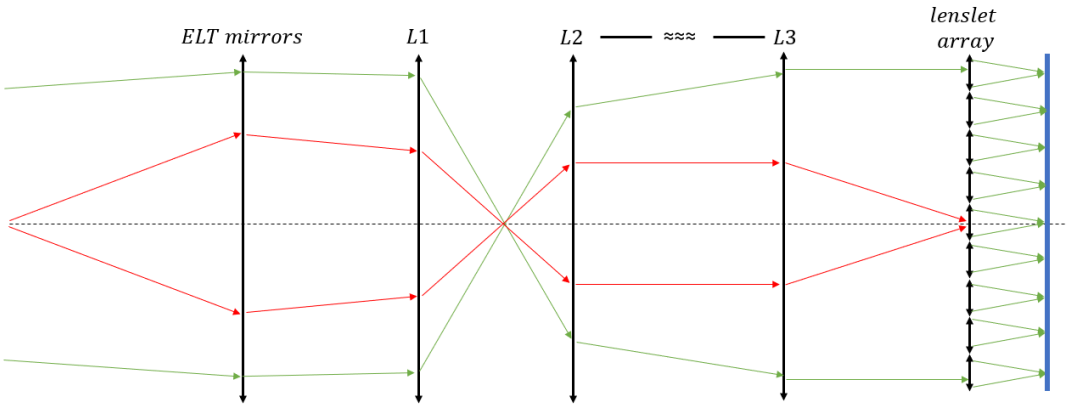

Figure 6.1: Schema of the focus and SH-WFS system that will be implemented. Red arrows represent the light coming from the pupil, whereas the green light comes from the LGS.

In this schema, the ELT mirror system is assimilated to a lens, as it was the case in chapter 2. After this, the lenses $L1$, $L2$ and $L3$ represent the zoom system. The lenslet array and the detector are the SH-WFS. The principle of the system is the following:

1. First, the $L1$ is focusing the system, so that the focus points of the LGS image and the pupil plane image become closer than before. As it has been seen before, the focal point of the LGS can change with a difference of ≈ 3,000 mm between the minimum and maximum zenith angle. "Accelerating" the system like this allows to reduce this difference to few centimeters. It also allows to decrease the difference with the pupil, that is only 37 m away from the first lens $L1$, whereas the LGS is between 90 and 180 km. This lens will accept the beam directly after the folding mirror so that it will be large enough (≈ 300 mm in diameter).
2. Then the $L2$ is placed in a position so that it is conjugated with the lens $L1$ for the rays coming from the pupil. The distance between the focus of the $L1$ and the $L2$ will be calculated so that the pupil rays are collimated at the end of the $L2$ lens.

3. Then the lens $L3$ will be used to focus the pupil beam on the lenslet array. Since the beam is parallel, the distance between $L2$ and $L3$ can change, and it will have no impact on the focus of the system FOR THE PUPIL. This allows accommodating for the light coming from the LGS at several zenith angles so that the lenslet arrays can effectively focus it on the detector. After this lens, the pupil beam is supposed to be focused on the lenslet array, while the beam coming from the LGS has to have precisely the same convergence angle no matter the zenith angle.
4. A telecentric lens is then placed, whose purpose is to convert the LGS beam directly into a parallel beam. Having a parallel beam is mandatory for the lenslet array so that all the sub-aperture will converge in the same plane. In this paraxial design, this lens is infinitely thin, so that focusing the pupil plane on it is the same as concentrating it on the lenslet array.
5. Finally, the light coming on the lenslet array will be focused directly on the detector. The distance between the lenslet array and the detectors and the distance between $L3$ and the lenslet array is fixed and will be equal to the focal length

6.2. Realistic Design in ZEMAX

Now that the principle of the system has been presented, a first design can be created using Optical Studio.

6.2.1. Presentation of Optical Studio: ZEMAX

ZEMAX is an optical design program, created to measure the performances of the instrument and create a new optical system. The principle is by ray tracing: from the source of emission, the software is calculating propagation of the rays through the optical system. It can be by applying the Snell-Descartes law ($n_1.\sin i_1 = n_2 \sin i_2$), and also the physical laws of propagation to measure the diffraction and interference effects on the system quality. The reason why this tool is widely used is for its capacity to optimize the system for a given criterion that can be defined by the user. The so-called "merit functions" allows defining for the system what is considered as a good design and what is not. During optimization, the goal of the system is to decrease this merit function as much as possible. However, this optimization tool is looking for local minimums of the merit function. Which means that if the original design is too different from the perfect one, there are few chances that the optimization will find it. The criteria on which the merit function is based are now going to be presented, and how they can be used to optimize the system.

The Spot RMS criteria

This criterion is the most widely used in the design, as it allows to know if a system is in focus or not directly. This criterion is using an array of rays propagating through the system. The beams are chosen so that they fill the entire surface of the system, from the edges of the aperture to the center. Once all the rays traced in the system, their image at the end is plotted to create what is called the spot diagram. Based on the shape of the plot, it is possible to assess the width of the spot. Aberrations play a vital role in this criteria, as an ideal system would have a spot elongation equal to the Airy disc, which is the diffraction limited spot created by the aperture. To optimize this, the values of the spot are set to 0, and the system aims at reducing as much as possible this spot size.

The Parallel ray criteria

This criterion asses whether the rays send to the image plane are parallel or not. This criterion could also be achieved by putting a paraxial lens with a given focal length and converge the beam, using then the spot RMS criteria to assess the performances. However, it can be practical (and faster !) to directly use this criterion. The way to set it is to put no weight in the X-direction, and only in the Y-direction. Thus, the system is calculating how the beams are equally spaced in the image plane in this direction.

The pupil location and size

The final and most important criterion that has been used in the design is the pupil location and size. This criterion allows to constrain the size of the pupil and to force the system to make it on a given surface. It is also possible, using the same criteria, to asses of the pupil plane quality. The pupil of a system has a unique characteristic: this is the only plane where all the rays coming from the different location of the object FoV

are crossing. In ZEMAX, this can be easily recognized by the change of the color of the rays (see Figure 6.2), where the color coding represents the different FoV. Although this is not very precise, as a first approximation it allows to locate the pupil position in a system, and its quality. The pupil position can then be constrained more precisely by setting a given surface to be the pupil.

6.2.2. First Design with Paraxial Lenses

The paraxial lenses are infinitely thin lenses, which means that they do not suffer from the chromatic or geometric aberrations that will be described in the next section. Thus, it is the perfect tool to start a design and evaluate its efficiency.

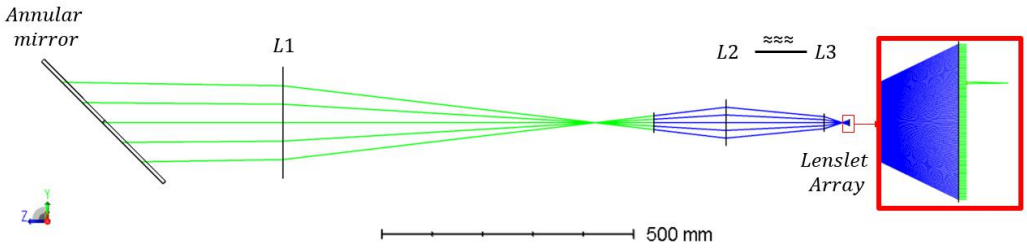

Figure 6.2: Paraxial Design created with ZEMAX

This design (see Figure 6.2) is exactly as the principle design that has been described before in this chapter. The change of colors between $L2$ and $L3$ It seems to perform exactly as it should be, as the Figures 6.3a and 6.3b show it. For the 5 zenith angles tested (between 0 and 60°), the system can accommodate perfectly with the translation between $L2$ and $L3$. The red box on the right is a focus on the lenslet array, to clearly illustrate the color changing at the lenslet's location (pupil plane that is made on the lenslet), in addition to the sub-aperture created.

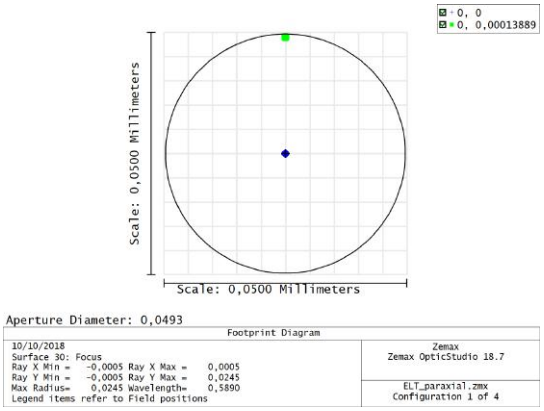

(a) Footprint diagram

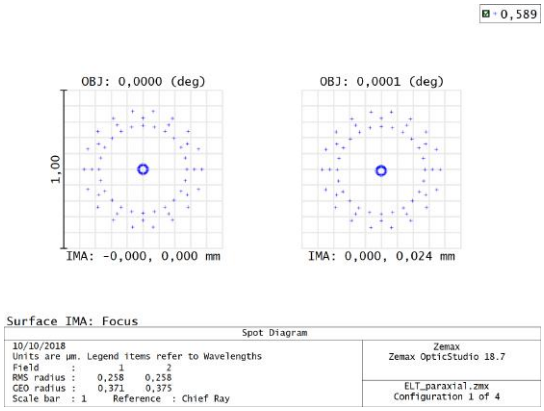

(b) Spot diagram

Figure 6.3: Performances diagram obtained at the focus of the lenslet (detector). The two fields used have an angle difference of 0.5" (= 1.3899×10^{-4} deg) relatively to the ELT M1 mirror.

Figure 6.3a shows that the distance between two light beams coming from infinite (the blue and green dots) separated by 0.5" have a physical distance on the detector of $24\mu m$, which is exactly the scale desired. Figure 6.3b also shows that the spot diagram of the system is as small as possible: given that the scale on the detector is 24 mum/0.5", the diffraction limited spot for a subaperture is supposed to be 0.131" $\rightarrow 6.3\mu m$. On Figure 6.3b it can be seen that the diffraction spot is way smaller. This result is not surprising, as for the moment only paraxial lenses have been used in the design.

Finally, Table 6.1 refers to the characteristics of the paraxial lenses used in the system. The critical part remains the f-number, noted as f/#. It is equal to the ratio between the focal length of a lens and the lens diameter. Basically, the higher the lens f-number, the more aberrations will be introduced by this optic in the global system. A compromise needs to be found, between low f/# systems that remains compact because of

the lower focal length, or higher f/# systems that will introduce fewer aberrations. It is commonly accepted in optics that a system with an f/# lower than 1 will introduce too much aberration.

Table 6.1: Initial lenses characteristics from the paraxial design

	Entrance beam diameter (mm)	Lens diameter (mm)	Focal length (mm)	f/#
L1	300	350	1000	2.8
L2	130	150	200	1.3
L3	13	20	60	3.0
Lenslet	0.48	0.48	5	10.4
Array	40×0.48	19.2	//	//

6.2.3. From the paraxial lenses to the real ones

The design presented before has been made with paraxial lenses, which is the first approximation of glasses with a thickness equal to zero. However, in reality, the lenses have a given width and a curvature radius that allows them to distort the light. These characteristics have a direct impact on the system performances, mostly because they add optical aberrations.

Common aberrations found in optical systems

These aberrations can be classified into two categories:

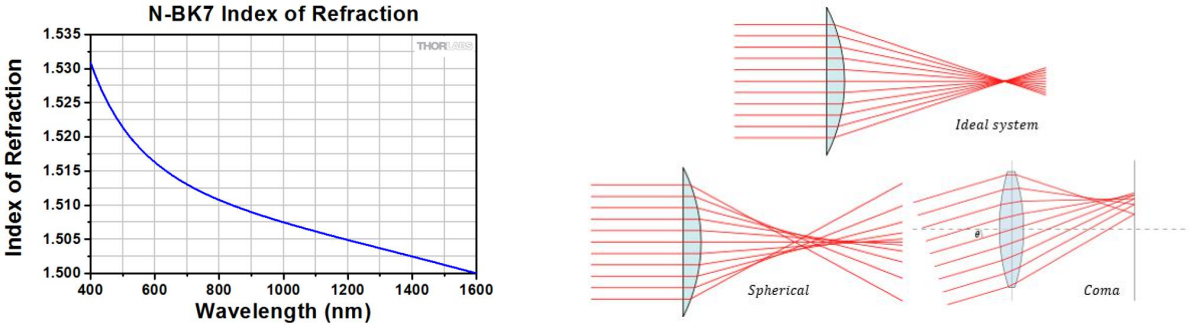

(a) Fluctuation of the BK7 index (Thorlabs)

(b) Effect of aberrations compared to an ideal system

Figure 6.4: Presentation of the main optical aberrations for a system

- The chromatic aberrations are a consequence of the variability of the refraction index of the lenses regarding the wavelength. The Figure 6.4a shows for example the fluctuations for the N-BK7. It is one of the most used materials for visible and near-infrared wavelengths because it is easy to manufacture while still having an important transmission. The consequence of these fluctuations are crucial for poly-chromatic systems, as the focal point will change as the refractive index of every lens is different. However, the light emitted by the LGS can be considered for our study as monochromatic, as it is created by the excitation of the sodium layer in the atmosphere. The rays received are centered around 598.5 nm. Although the variations of the N-BK7 are quite important for the whole wavelength range, for this case it can be considered as constant. Therefore, this aberration will be neglected here.

- The geometric aberrations are the consequences of the thickness, curvature of the lenses, in addition to micro-imperfection that can deviate the light from its optimal path. These aberrations also affect the quality of the images recovered by the system. To be able to measure the atmospheric distortions produced by the atmosphere, these aberrations need to be less important. Reducing them is a key point for the system. The geometrical aberrations are often divided into several categories that are briefly described here:

  Spherical This aberration is the consequence of the spherical shape of the lenses. This shape is easier to manufacture, but the consequence is that the marginal rays (the one coming from the edges of

the system's aperture) will have a different focal point from the paraxial focal point predicted by geometrical optic. The Figure 6.4b illustrates this: the rays that traverse near the edges of the lens are not focused at the same location as the one near the center. This issue can be minimized by creating an aspheric lens, that is going to considerably reduce the effect. If this is not corrected, there will not be a unique focal point, but several, and the diffraction pattern will be larger. In the LGS system, the asphericity will be introduced by adding a conic constant to the shape of the lenses in ZEMAX, to reduce this effect as much as possible.

Coma The Coma is created by the fact that rays parallel between them but not parallel to the optical axis will not converge toward the same focal point. As it can be seen in Figure 6.4b, the focal point will be displaced in the focal plane, created what is called a cometary coma. This effect is particularly visible for large FoV systems since the angle between the rays and the axis can be more important. For the LGS system, this effect is thus essential to correct, to not add more elongation to the LGS for example. The solution is the same as for the spherical aberration and consists on using aspherical objects.

Astigmatism The manufacture of a lens cannot be perfect: small default is introduced, which change the curvature radius and refraction index locally. This non-homogeneity created a local variation in the focal distance, astigmatism. In practical nowadays, the imperfections are considerably decreased thanks to high-precision manufacture thanks to lasers. However, to be able to quantify them, existing lenses with the astigmatism properties will be used in ZEMAX. Moreover, a system with two lenses will be used to replace one paraxial lens: the two lenses can compensate each other's astigmatism aberrations, creating a system almost perfect from this point of view.

The optics catalogs

To be able to compensate these aberrations, the realistic design will use standard lenses that have already been built by constructors, mostly on the Thorlabs and Edmund Optics catalogs provided by ZEMAX. However, the two first lenses have a size that is not standard, and no lens like this can be found on the archives. The goal here is to use an existing doublet (two lenses put together) with a radius of curvature $R1$, $R2$, $R3$ and thickness $t1$ and $t2$ so that they can be multiplied by a correction coefficient K to give the desired lens. The idea is to use lenses with the same $f/\#$, which means that the ratio between the focal length and the diameter must be the same. Using similar $f/\#$ means that the lenses found in the catalog have already been "optimized" for similar behaviors, the only difference being that they are smaller than the one required for the system. This coefficient can be found by comparing the required focal length of $L1$ f' with the focal length of the one provided in the catalog f. Then the diameter of the lens from the catalog D has to be equal to D'/K. The radius and thickness parameter of the system found can then be multiplied by this factor K to obtain the desired lens.

Optimization of the system for high performances

A working system for the LGS WFS needs to have two important characteristics:

- First, the system shall provide an image quality sufficient to allow an efficient centroiding of the LGS beam. It means that the beam project on the detector must have a PSF with an RMS width lower than the diffraction limit of the system, which is equal to:

$$1.22 \times \lambda/d \times 0.5"/pix \tag{6.1}$$

  Here the pixel size is set to $24\mu m$, while the sub-aperture diameter is equal to $d = 1\ m$ and the wavelength of observation $\lambda = 0.589\ \mu m$. Which means that the spot size must be lower than $\approx 7\ \mu m$. In practical, the beam will never be completely diffraction limited, and this value can thus be greater. A value similar to the pixel size is the goal of this optical design. More elaborated ones might be able to reach higher performances, but the lack of expertise in this domain prevents me from doing it.

- Second, the system shall introduce as small aberrations as possible on the wavefront in the pupil plane. The point of the system is to measure the wavefront error in the pupil plane, and for this reason, the errors created by the system must be less important than the one brought by the atmosphere. If this is not the case, the system might start to correct for these errors in addition to the atmospheric ones, since it will interpret the optical aberrations created by the instrument as an atmospheric aberration.

To be able to optimize the system, these criteria can be set to what is called in ZEMAX a "merit function." The optimization can then be made on the parameters, mostly the asphericity of the surfaces for example that can considerably reduce the aberrations created by a given system. The strategy that has been used is the following:

1. Starting from the paraxial optical design, the first paraxial lens is changed into a real doublet. The parameters of this doublet are adjusted so that the pupil plane located between $L1$ and $L2$ has aberrations as small as possible. This has been done by changing the 8 first aspheric polynomial coefficients of the first lens of the $L1$ doublet.
2. From this part, the second and third lenses can be added. The system has to be adjusted so that the pupil is collimated at the end of $L2$, and the pupil is projected on the lenslet thanks to $L3$. Again an optimization is made on the asphericity of the lens $L2$ and $L3$ to reduce the geometric aberration of the system.
3. Then a telecentric lens is added to the design: the point of the lens is to make the spot beam collimated on the lenslet so that the focus of the lenslet array will always be located in the same plane. Moreover, the distance between the lens and the $L3$ has to be chosen so that the pupil plane is directly on the lenslet array, located just after the telecentric lens. This lens was not required for the former design, as the paraxial $L3$ was taking care of the focus of the pupil beam and the telecentricity of the LGS beam. However, in a real system, more freedom degrees need to be added to such a system. Which is the reason why the telecentric lens is used.
4. After this, a global optimization has been made to try to improve as much as possible the characteristics discussed before. The optimization is made very carefully, by slightly changing some of the parameters.
5. Finally, adjustments can be made on the lenslet array to optimize the image scale, and make it such that two rays coming with an angle of 0.5" are separated by 24 μm on the detector.

The location of the subaperture, in addition to the zenith angle, have a critical impact on the system performances. For this reason, to optimize the system correctly, 9 configurations have been set up. Three configurations correspond to the three zenith angle range, which are here 0°, 30° and 60°. For each of these angles, the subaperture is located at a different pupil location (in the upper edge, the middle, and the lower one). Thanks to this, the optimization can be made for all the subapertures and all zenith angle, allowing decent performances for all these configurations.

6.2.4. Presentation of the final "realistic" design

Now the final design that has been made during the project can be presented in Figure 6.5.

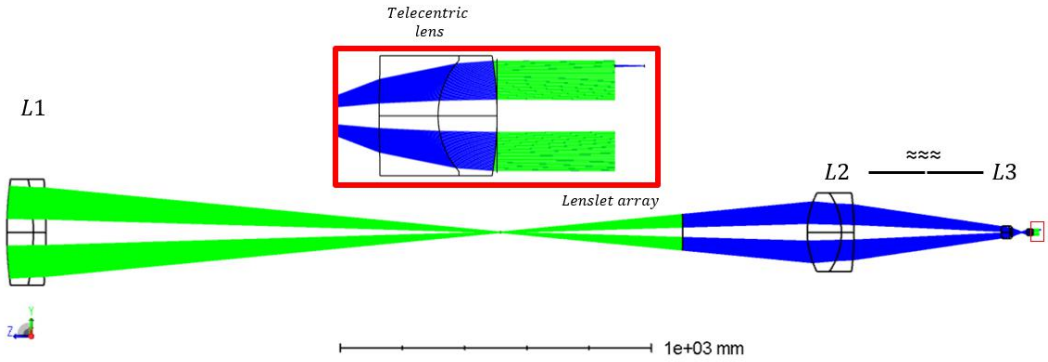

Figure 6.5: Real design realized with ZEMAX

The layout of the system remains the same. A distance has been added between the telecentric and lenslet array, which seemed to decrease the constraints on the merit function and allows to reach a more optimal configuration.

The performances are quite good and in line with what could be expected from such a system. The pixel scale on the detector is indeed equal to $0.5"/pix$. The only issue in the design is that the system was complicated to

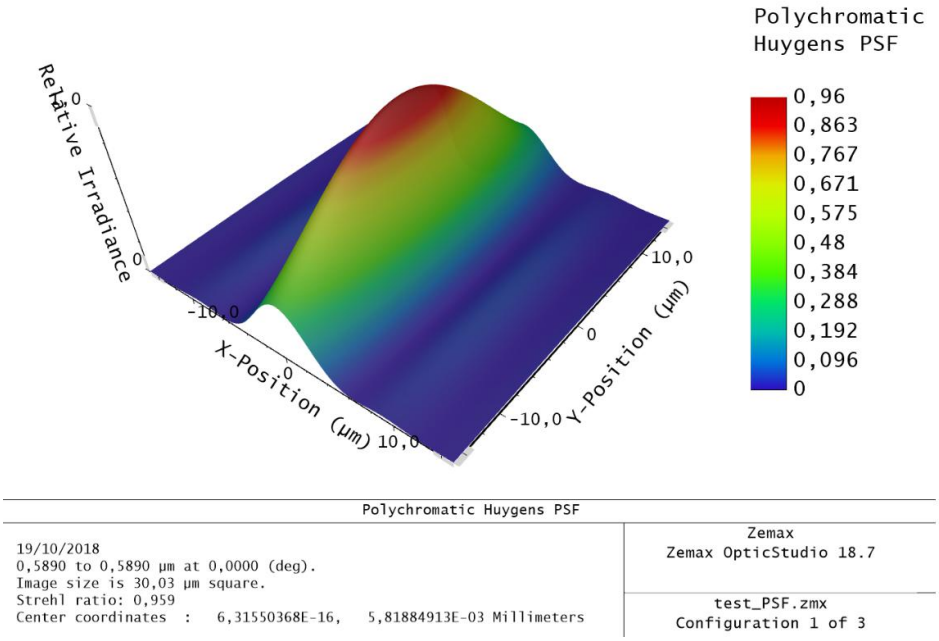

Figure 6.6: PSF obtained for the worst conditions (zenith-angle/sub-aperture)

adapt in real because it was too "fast." For this reason, the system has been slightly changed, with for example $L2$ that has been made two times slower, with a focal length of 400 mm. The principle of the system remains the same.

To compensate for this increase of length added to the system, folding mirrors have been used to make it more compact (see Figure 6.7). The mirrors have been placed between the lens $L1$ and $L2$, and the performances of the system remain the same as the one presented before. The light on the top right is coming from the pre-focal station and then bounce on the annular mirror represented by the surface on the top right. The science light can propagate in the same direction without bouncing on this mirror, and reach the cryostat that is located directly after the annular mirror.

Conclusion

This Chapter 6 presents the optical implementation of the system. The solutions that have been found to tackle the major issue of the system, which is creating a SH-WFS that works for any zenith angle between 0 *and* 60 °*. A paraxial design has first been created, using ideal lenses to illustrate the principle of the solution and find the first estimations of the optical components. Then, using lenses adapted from Thorlabs catalogs, a real system has been found with performances that fall within the requirements.*

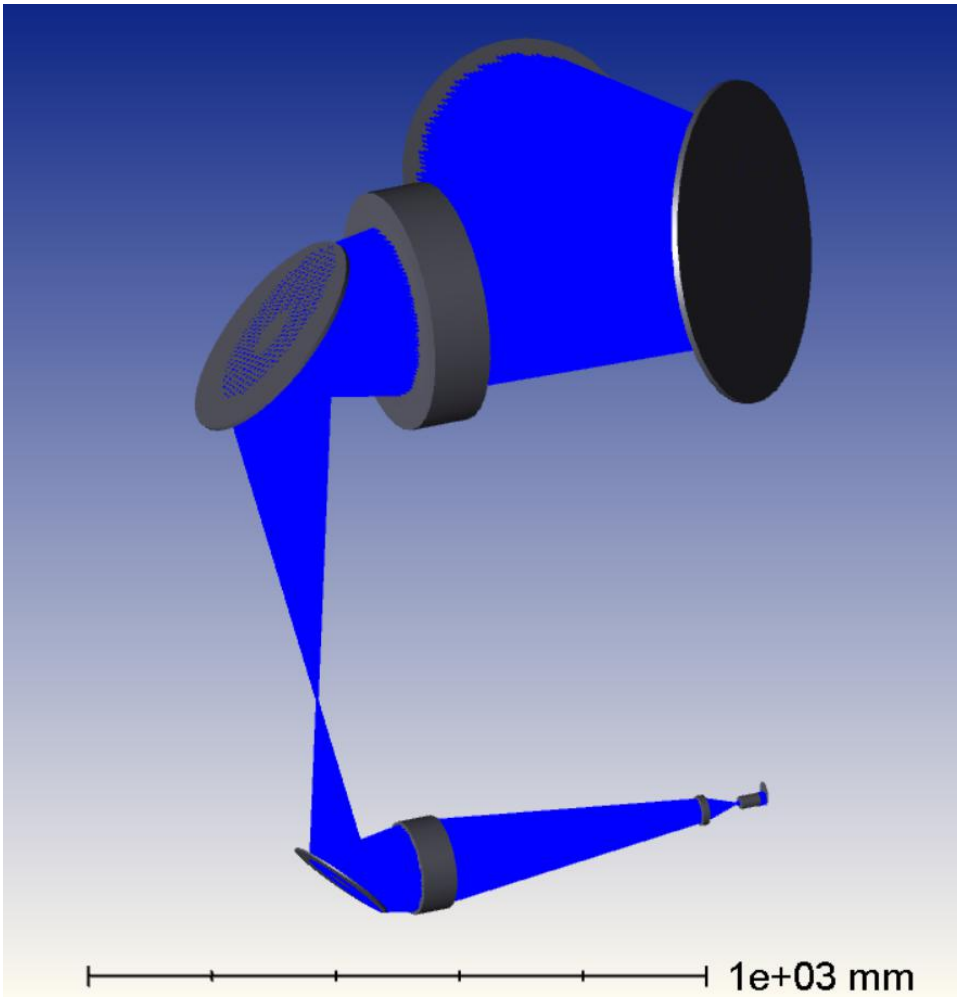

Figure 6.7: Folding design of the system

Chapter 7

Mechanical Design for the SLAO system

Once the optical design of the system with ZEMAX in Chapter 6 has been created, the mechanical design needs to be added. It represents the layout that will hold and support the lens system and allows the system to perform as it should. The mechanical design presented here is a first draft of the real one: it represents the starting point from which Alex Tripsas, another student, will elaborate a more complex design.

Contents

7.1. Presentation of the METIS architecture and location

Before implementing the mechanical design of the SLAO system, it is crucial to understand the surrounding of METIS. The instrument is located on the Nasmyth platform of the ELT, with the 2 other instruments that will equip the telescope (see Figures 7.1).

MICADO (for Multi-AO Imaging Camera for Deep Observations) is the first dedicated imaging camera for the ELT and works with the multi-conjugate adaptive optics module MAORY (Davies et al., 2016 [22]). Its wavelength range will be in the near-infrared, with a sensitivity comparable to NIRcam on the James Webb Space Telescope but with the high-resolution provided by the ELT aperture and the atmospheric correction thanks to MAORY. It also has a single-slit spectrograph to obtain the spectra from objects by diffracting the light coming from them.

HARMONI (for High Angular Resolution Monolithic Optical and Near-infrared Integral field spectrograph) will be the telescope spectrograph in the near-infrared ($0.47-2.45\ \mu m$). This integral field spectrograph (Thatte et al., 2014 [75]) will be able to create pixel-by-pixel spectra of objects at very high spectral resolution, enabling the observation of individual contributions of sub-structures that will be resolved by the ELT. It will benefit from a post-focal Laser Tomographic Adaptive Optics (LTAO).

The location of the SLAO system on the architecture of the instrument, presented in Chapter 1, induced some constraint on the system's size:

- Since the system should be compact, the maximum size allowed in width is the METIS width, which is $\approx 4\ m$.
- The depth of the system has to remain small enough so that it can be placed between the PFS and the WCU chariot. This creates a constraint in depth, that must be smaller than $\approx 0.6\ m$.

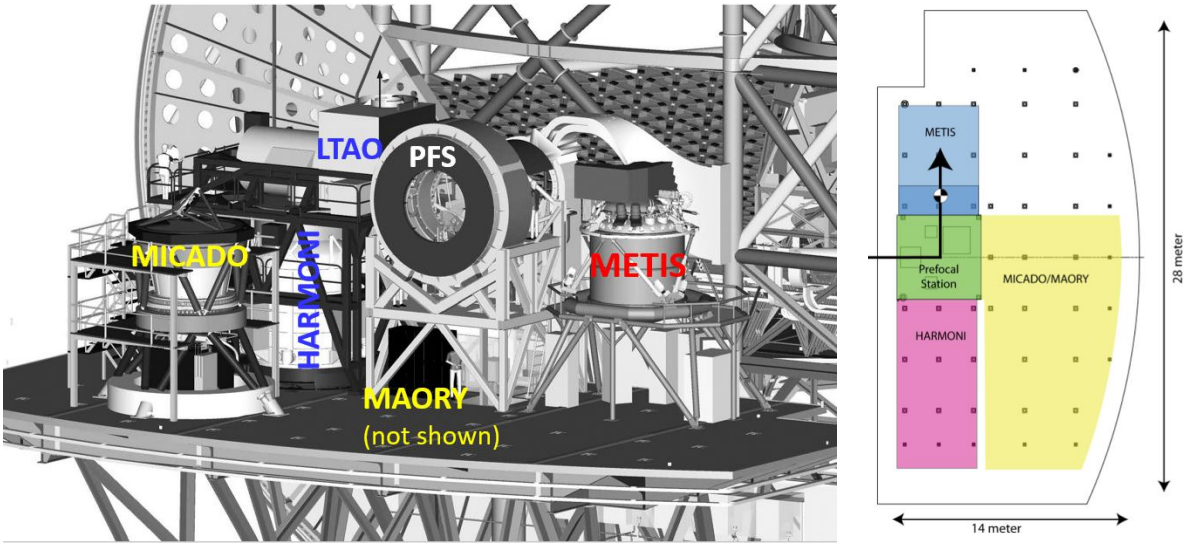

(a) Global view of the instruments (MAORY has been removed for visibility reasons)

(b) Aerial view of the instruments

Figure 7.1: Layout of the Nasmyth platform (Brandl et al., 2016 [15])

- Finally, the height of the system must be such that the system can also lie on the platform where the cryostat is located, to prevent as much as possible the optical miss-alignment and independent movements with the instrument METIS. For this reason, the instrument should not exceed the $\approx 3\ m$ in height.

These constraints on the size are not hard to follow, except the one concerning the depth of the SLAO system. As it has been shown with the optical design earlier, the space envelope required for the optics is way smaller than this one.

7.2. The SLAO system mechanical design

This mechanical design that will be presented here has been built from the ZEMAX export file. Although not complete, it allows having a first estimation of the size and layout of the system.

7.2.1. The structure of the system

The idea for the design is to put the optics inside a cage, whose structure completely covers the structure of the system. The blue and green beams represent the cone of light emitted by the LGS that is going through the system. The blue one represents the light coming from the center of the FoV, while the green one represents the one coming with a 5" angle from the center, to simulate the 10" FoV of the system.

The three configurations that are illustrated in Figure 7.2 represent the configurations where the ELT is pointing at a LGS with respectively a 0 and 60° zenith angle, and the one where the SLAO system is not used. These configurations represent the extreme configuration for which the system will be confronted. Several decisions were then made regarding the global layout of the system:

- First, the lenses $L1$ and $L2$ have been placed on the same place, so that it is easy to create a structure that can hold them both. The structure that is used for them is perfectly integrated with the cage structure dimensions so that the stiffness can be as large as possible.
- The holding support for the $L3$ and the telecentric lens have been made with a simple support. The purpose here was to have a first estimation of the holding support dimensions.
- The annular mirror has been placed right at the focal point of the ELT. The dimensions of the hole are not adjusted yet, as it should be according to Chapter 2.
- The folding mirrors have been used to reduce the size of the system, allowing smaller dimensions.

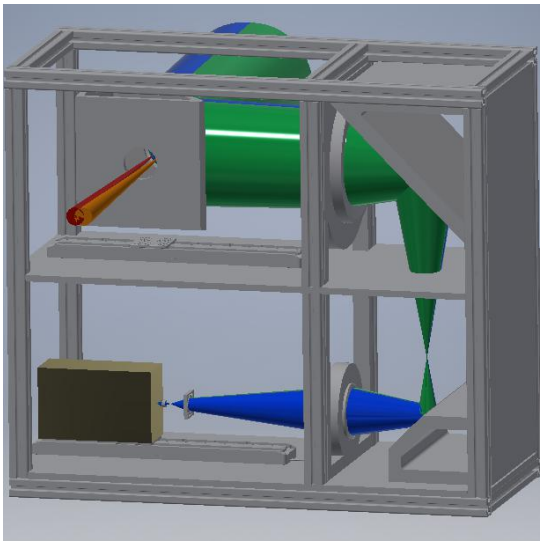

(a) Zenith angle

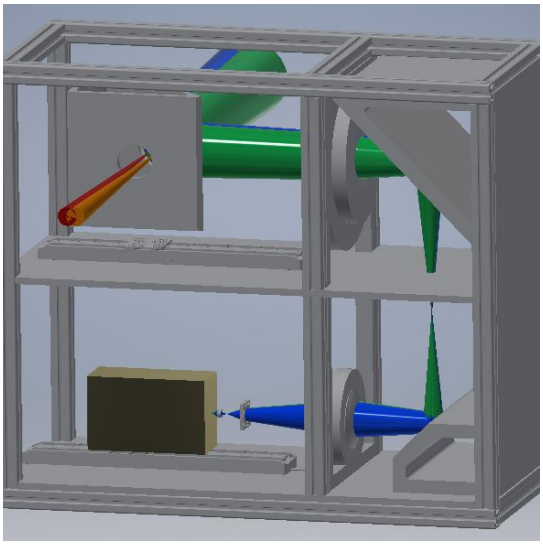

(b) 60° zenith angle

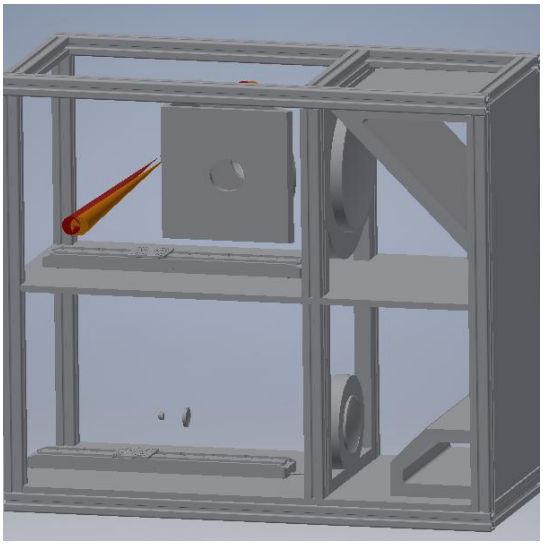

(c) No SLAO system

(d) QR code to get access to 3D model of the system

Figure 7.2: Visual mechanical design for the SLAO system, for three configurations

- The profiles used for making the bars of the cage have been found on the website https://www.item24.de/index.html. They have then been copied and extended to the desired size, assembled to obtain the desired dimensions of the system.
- Normally, the stiffness of the profiles is not enough to reach the micro-meter precision required for such systems. Therefore, the final system would have some layers between the bars to hold the lenses and mirror supports, as it is shown in Figure 7.2 for the system holding the two folding mirrors.

7.2.2. Moving sections

The system must also enable the translation of two moving stages:

- The first one is the annular mirror translation stage. When the SLAO system is used, the mirror will be here to direct the LGS beam toward the focus and SH-WFS optics. However, it has been shown in Chapter 2 that the use of this mirror will considerably decrease the FoV of the system. Thus, while the SLAO system is not used, this mirror will need to be put out of the science FoV to keep it as large as possible.

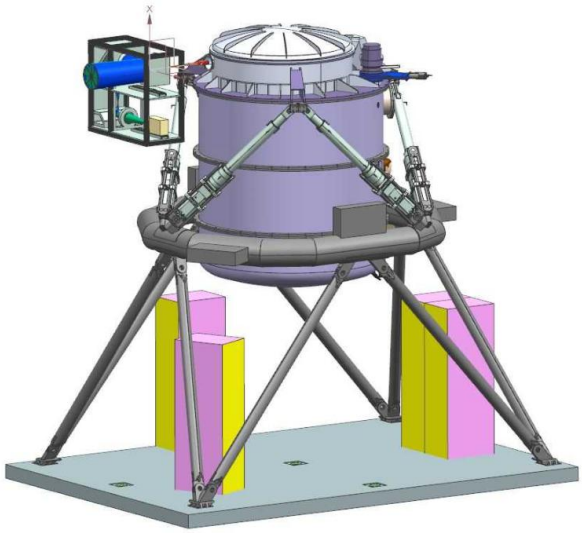

Figure 7.3: Global architecture of the ELT/METIS on the Nasmyth platform

- The second one is the distance between the second and third lens, which needs to be adjusted relatively to the zenith angle of the system to keep the focus on the same plane. The $L3$, telecentric lens, lenslet array, and camera will move all together in that part. The mechanical will have to make this translation stage possible.

Both systems have different constraints: the translation of the annular mirror mostly requires to move an elliptical object and its support whose dimensions are estimated to be 550 $mm \times 400$ mm. This part will be massive, but the precision required is also not as crucial as for the $L3$ system. On the other hand, the $L3$ system will be probably lighter but will need an excellent precision to adjust the focus of the system at any zenith angle.

Conclusion

This chapter aims at presenting the first mechanical design that has been made thanks to AUTODESK-Inventor. The main goal of this part was to prepare the work performed during the thesis for the other student Alex Tripsas that will work more precisely on the mechanical implementation of the system. Although the holding support is not real yet, it paves the way for further advances and gives a general idea about the size of the system, and how it would be designed.

Chapter 8

Sky Coverage calculations

Now that the system's characteristics and performances have been presented, the final step of the project is to calculate the sky coverage of the SLAO system. The primary purpose of this system was to obtain an AO correction at any location in the sky, allowing the possibility to do high-resolution science everywhere. In addition to the sky coverage calculations, the purpose of this part is also to present the problem of the optimal wavelength range.

Contents

8.1. Calculation of the ideal wavelength range

The wavelength range is the integration boundaries between which the system will capture information. It is crucial to define, as a too large one will bring the unnecessary noise from the atmosphere, while a too small one could cut some essential parts of the signal. Moreover, some bands have for example a higher stellar emission but also include higher sky emission. For this reason, it is essential to define the exact range for which the signal to noise ratio of the system will be the most important.

8.1.1. The sky transmission and background emission wavelength evolution

The sky background emission is not flat, as it can be seen in Figure 8.1b. The primary emissions come from the OH features that are present in the atmosphere, where these molecules excited by the energetic photons from space are emitting noise. The thermal component of the atmosphere is also important, especially in the K-band which is considered as the beginning of the thermal infrared.

The transmission from the atmosphere is not flat either (cf Figure 8.1a). The main absorption lines are due to the presence of water in the upper atmosphere, which creates a massive decrease in transmission efficiency. The curves have been generated thanks to the ESO simulator, available at `https://www.eso.org/observing/`. The entries are the default ones for a location at Cero Paranal, which is very similar conditions as Armazones. It means that the seeing, position of the moon, zodiacal light, hour of observation are set to median conditions. The zenith angle is set to 30°, which is the standard value used in the YAO simulations. The curves are plotted in the J-, H- and K-band, with logarithmic steps ($\lambda/\Delta\lambda = 20,000$).

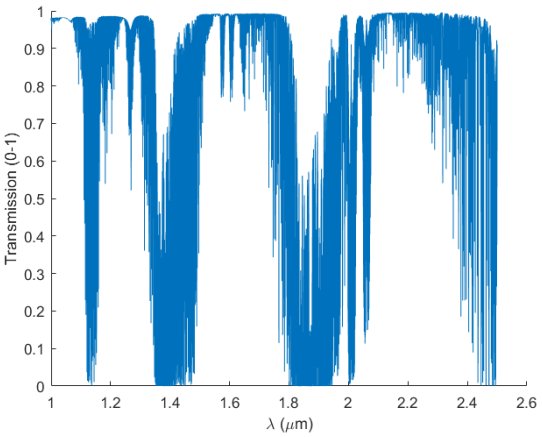

(a) Sky Transmission

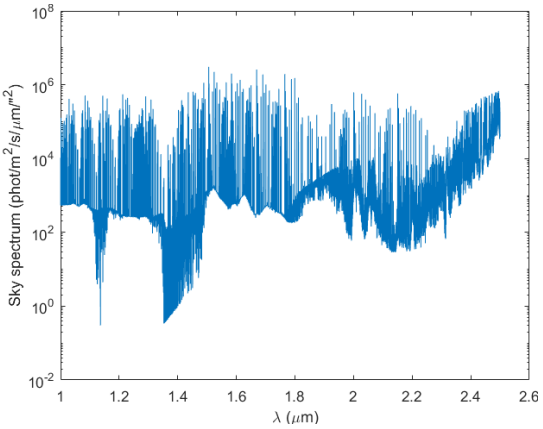

(b) Sky Emission

Figure 8.1: Atmospheric key parameters relatively to wavelength. These curves come from the ESO atmospheric model (Noll et al., 2012 [53] ; Jones et al., 2013 [37])

8.1.2. Instruments transmission wavelength evolution

As for the detector noise, the SAPHIRA detector can cover the J-/H- and K-band efficiently. The Quantum Efficiency (QE) will be slightly wavelength dependent, as it is shown in Figure 8.2a. The curve for the quantum efficiency taken is the one with an important APD Gain. However, since the wavelengths used are in the J-, H- and K-band, the cutoff frequency observed here does not matter. For this reason, the quantum efficiency has been modeled as the brown curve that can be seen in Figure 8.2a.

For the instrument transmission, this is different: the optics required for the system, in particular, the Common Fore Optics (CFO), have an impact on the system transmission. The CFO is designed to let go through the science beam of METIS, in addition to the SCAO beam which is in the K-band. Thus, the optic will be less efficient in transmission in the J and H bands. It can be seen on the Figure 8.2b. Finally, the ELT's transmission can be considered as flat in a first approximation for the wavelength range JHK. The mirrors have a reflective curve that is approximately the same for every wavelength. Thus, the global transmission has been set to $\epsilon = 0.9$.

8.1.3. The global stellar spectrum

One fundamental question to consider is the near-infrared spectrum expected from the typical target for the NGS. The problem is quite complex, because it has to take into account for example that bright stars categories such as O- or B- types are much rarer but emits way more light, whereas the typical K- or M- types are common but visible only at a smaller range. The categories for the star have been created relatively to the spectral type of the star, which is directly linked to its mass and its age. The density of a star's nature can be estimated via several models such as the Salpeter distribution (Salpeter, 1955 [67]) and its modifications (Kroupa, 2002 [41]). Moreover, some bright extra-galactic objects such as Active Galactic Nuclei could also be used as guides (Netzer, 2015 [52]), which have a completely different spectrum.

As shown in Figure 8.3, the difference of emission in the J-band can considerably differ depending on the type of stars used. Between an O-type and an M-type, it can be as large as 10×. To correctly estimate the number of photons taken from a "typical" object, what is required would be an average spectrum of all the objects that can be seen with up to the limiting brightness of the SLAO system. However, it has not been found during the researches, and will probably need to be made in a more extended study of the problem. This typical spectrum will most likely depend also on the galactic latitude.

8.1.4. The ideal wavelength range

The Sections before have shown that the ideal wavelength is a multi-parameter problem, unsolvable with only physical considerations. Thus, a map of the signal-to-noise ratio has been built, a function of λ_{min} and λ_{max} the boundaries of the waveband.

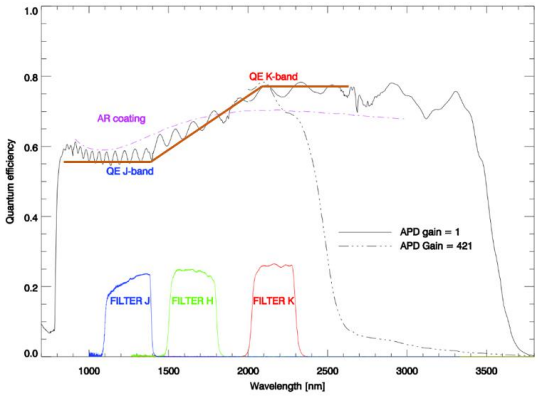

(a) Quantum efficiency (ESO, 2017 [26])

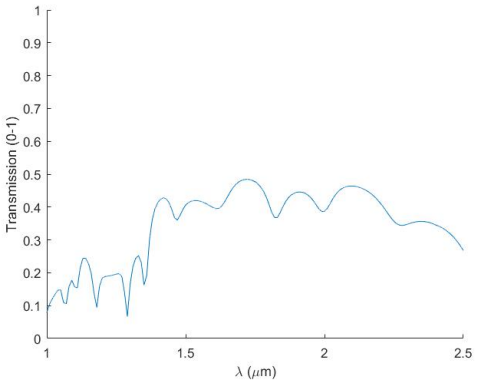

(b) CFO and SCAO optics transmission (Agocs, 2018 [1])

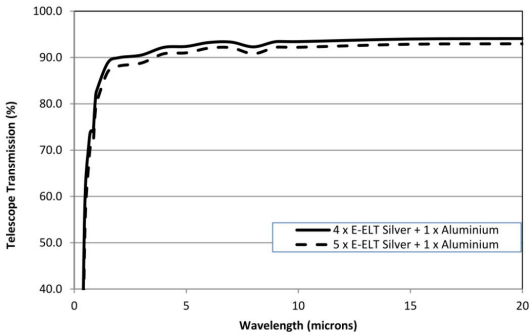

(c) ELT's optics transmission (Agocs, 2018 [1])

Figure 8.2: Instrumental performances relatively to the wavelength

Several things can be discussed in Figure 8.4a:

- The lower diagonal is not filled, since λ_{min} cannot be larger than λ_{max}.
- The iso-SNR lines are almost diagonal, which shows that there is no preferred wavelength range: the larger the integration waveband, the higher the SNR. This is because even if the integration could be better in the J and H bands, for example, the lack of instrumental transmission equalizes everything.
- It can be surprising to see that the larger the integration band, the better the SNR. However, the atmospheric transmission in Figure 8.1a indicates that there is almost no point of integrating outside the JHK bands since only sky noise will be integrated without any star's signal. The reason lies in the noises perturbations that are not linked to the atmospheric emission, the RON, and DC. These noises have approximately the same value no matter the band considered, and for this reason, they globally leveled everything to low SNR. Moreover, it is important to also consider that since this is a "Sky-background dominated problem", the signal to noise ratio evolves as $SNR \propto N_{phot}/\sqrt{N_{back}}$. This can, therefore, be seen as something like: "even if a small amount of photons is recovered, it is better than nothing." Figure 8.4b can convince the reader that in the same conditions but not taking into account the DC and RON, the decrease in the SNR

From the Figure 8.4a, the best wavelength range can be determined by looking at the values of wavelength for which the signal to noise ratio is the most important. Thus, the best integration band seems here to be $1\ \mu m \rightarrow 2.35\ \mu m$. These values can change regarding the K-band magnitude of the plot. For example, for a 10 mag_K star, the optimal wavelength will be extended to 2.5 μm since the star is so luminous that the more light, the better. The K-band magnitude chosen for the plot corresponds to the limiting magnitude for which the truth sensing correction in MATLAB (cf Chapter 4) is stable within that magnitude range.

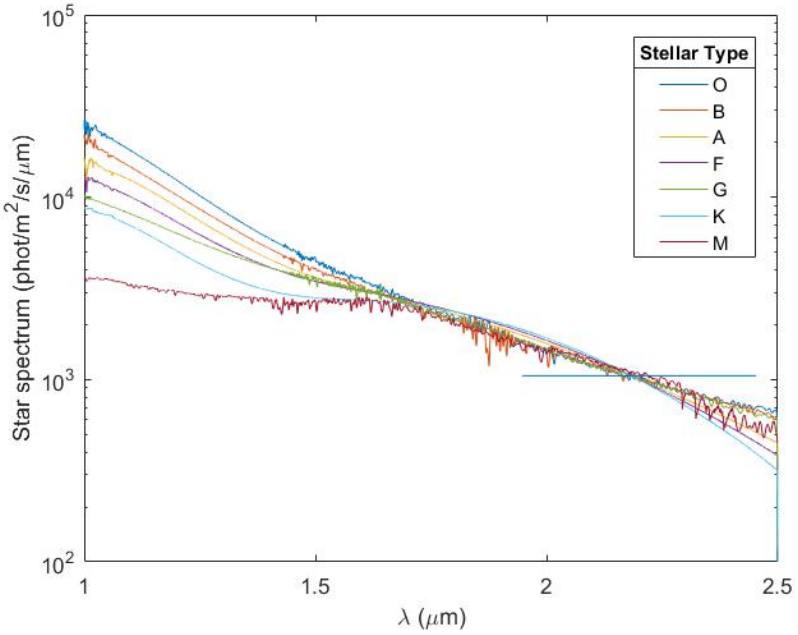

Figure 8.3: Evolution of the stellar spectrum for the same K-band magnitude of 16.6, illustrated by the horizontal blue bar.

8.2. The sky coverage expected with the SLAO system

In the chapter 4, the limiting magnitude required for the SLAO system to behave correctly has been defined. It is estimated to be around a K-band magnitude of 16.5. Answering the question: "how frequent are objects with such a magnitude ?" is calculating the sky coverage of the SLAO system. Since humankind is living in the Milky Way, it is easily understandable that the star density will be different relatively to the direction of the galactic latitude targeted. The Milky Way is thought to be a barred spiral galaxy, with a structure similar to the one presented on Figure 8.5.

Because the galaxy is a disk, the probability of finding stars in the galactic plane is way more important than at high galactic latitudes. The arms of the spiral galaxies are supposed to be density waves that propagate around the galactic center, triggering the star formation in their path. The reason why they appear blue is that they are populated with newly populated stars, with strong emissions in the blue wavelengths. The Sun and our solar system are located in one of the galaxy's arms, and the stars are thus more rare at high galactic latitudes, especially the bright stars. This is illustrated by Figures 8.6a, 8.7a and 8.7b. For a given number of stars in a 1 deg^2 FoV, the higher the galactic latitude, the lower the limiting magnitude.

One thing that can also be noticed from Figures 8.6b, 8.7a and 8.7b is that the Near InfraRed (NIR) bands used are also important. For a given number of stars in a 1 deg^2 FoV, the J-band will require a brighter object than the K-band. This is mainly due to the flu conventions, as the normalization flux to calculate the magnitude is changing relatively to the band used. In all the work performed in this chapter, the spectrum has been normalized using K-band magnitude. For this reason, this is this band that will be used to calculate the sky coverage. From the figures, it can also be noticed that the data used produce the same order of results as the one from the 2MASS survey (Skrutskie et al., 2006 [73]).

Now that the data have been defined, it is possible to investigate for the stellar density. Taking the information from Figure 8.6a, it can be estimated that the number of stars with a magnitude below or equal to 16.5 K-band magnitude for low, medium and high galactic latitudes is respectively 2×10^4, 3.5×10^3 and 2×10^3 #/deg^2. This can be converted directly into the number of stars into the METIS FoV, taking into account that the FoV of the instrument will only be round, with a circular diameter of ≈ 30". The results can be found in Table 8.1.

As it can be seen on the Table 8.1, the FoV and sky coverage of the system are enough to have a 100% sky coverage at low galactic latitudes. However, this is not the case anymore for higher galactic latitudes, where

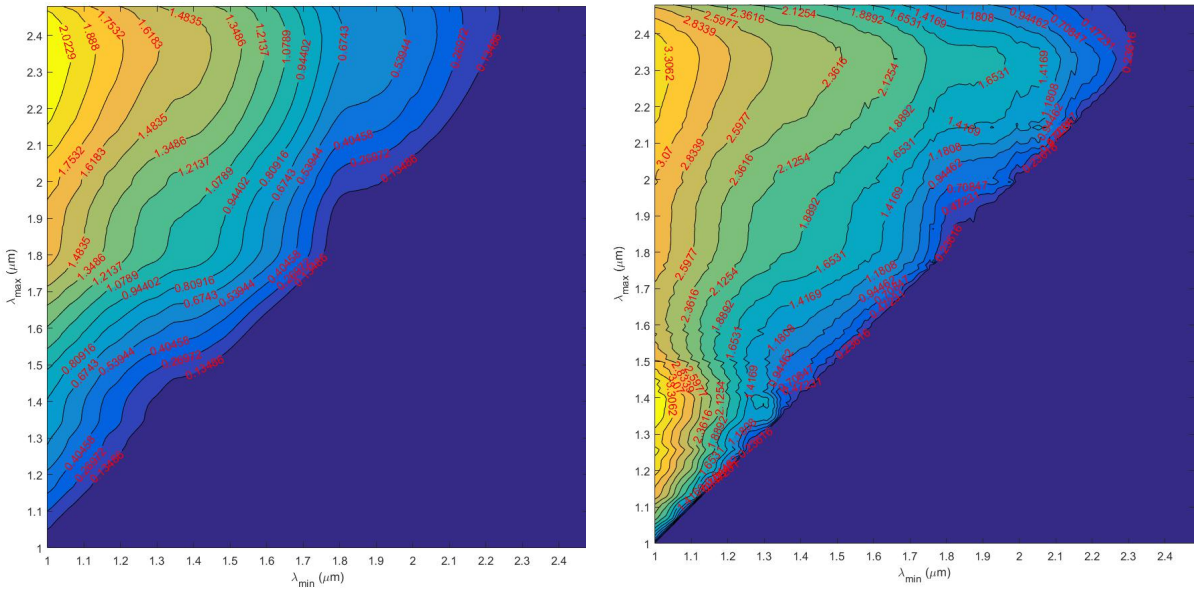

(a) Realistic estimation of the SNR

(b) Estimation without the DC and RON

Figure 8.4: Signal-to-Noise Ratio map for a star of magnitude 16.5

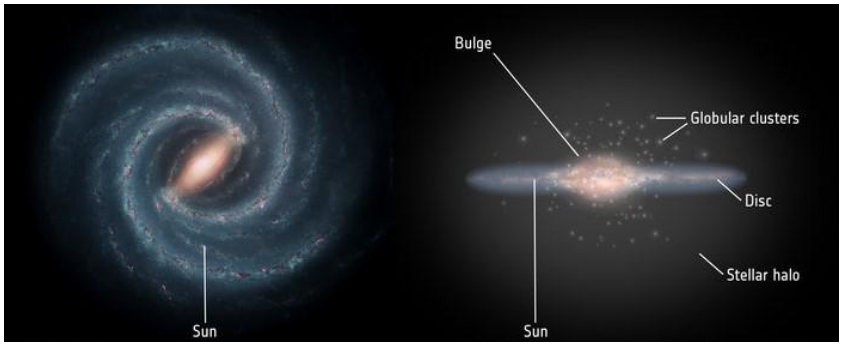

Figure 8.5: Presentation of the Milky Way structure (ESA, www.esa.int)

the sky coverage decreases to 10%. The results found are a good first estimation of the sky coverage. However, several things need to be taken into account:

- The number of stars in a given FoV estimated with the 2*MASS* survey might be underestimated. It can be seen from the Figures 8.6a and 8.6b that the survey has a limiting magnitude. The question is to know whether this limit is created by the deepness of the survey (the magnitude limit for the survey) or if this is just a limit of stars (no more stars in the Milky Way within the range). However, the second option is improbable, like very deep surveys such as COSMOS (Laigle et al., 2016 [43]) show stars with a K-band magnitude lower than 16.5. For this reason, it is safe to assume that the number of stars will be much greater than the one predicted by the 2*MASS* data, increasing the sky coverage.
- The FoV of the instrument taken for the calculations is equal to 30", which is the METIS FoV. However, it has been seen in Chapter 2 that the actual FoV for the science beam might be reduced. This will also have drastic consequences on the sky coverage, as the only chance of having a sufficiently bright NGS will be that the scientific object observed is bright enough in the mid-infrared bands.

The final graph of this work can be represented as the one in Figure 8.8. It represents the Strehl ratio that can be expected, given the K-band magnitude. As it can be seen, the maximum performances or for the SCAO configuration, but it also requires a star so bright that the sky coverage is estimated at 1%. Then, the SLAO system with high-frequency truth sensing can be used. This configuration is for the moment under investigation but could provide better performances than the typical SLAO system, given a bright enough NGS in

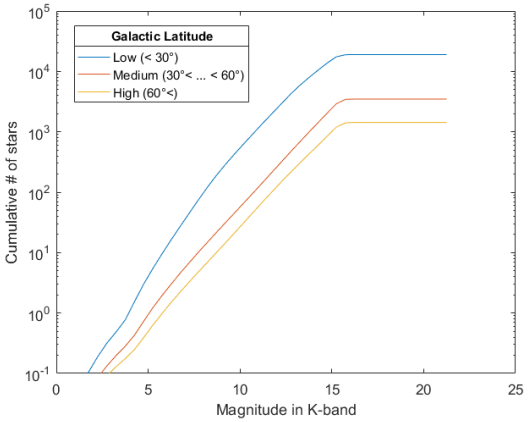

(a) K-band at several galactic latitudes

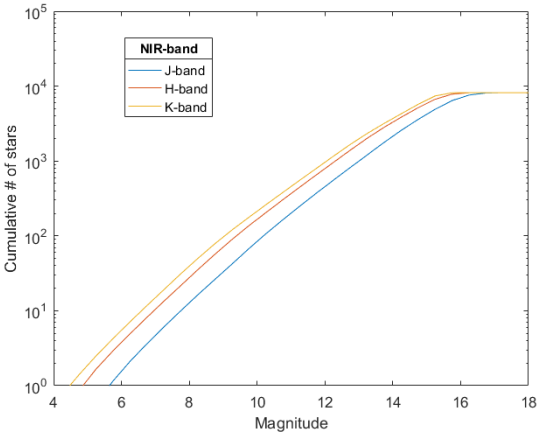

(b) J-/H-/K-band for a global galactic latitude

Figure 8.6: Representation of the cumulative number of stars above a given magnitude

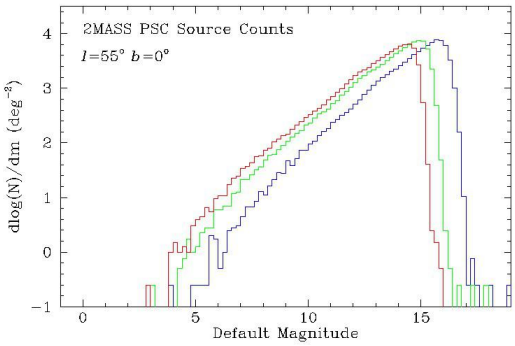

(a) Galactic latitude $l = 55°$

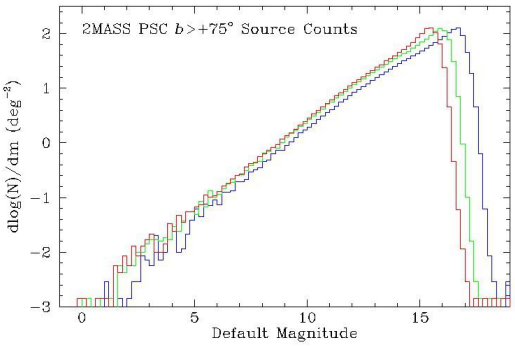

(b) Galactic latitude $l > 75°$

Figure 8.7: Representation of the cumulative number of stars above a given magnitude for J-/H-/K-band by the 2MASS survey (Skrutskie et al., 2006 [73])

the FoV. After this, the SLAO system developed in this project could be used with a sky coverage estimated to ≈ 100%. Moreover, in the case where no NGS will be available, the system will still be able to perform Strehl performances between 20 and 50%, depending mainly on the sodium layer profile. The limits between the different configurations are not fixed and need to be investigated, at it depends on parameters such as the sodium profile, target of observation, seeing of the atmosphere. But this plot gives a good estimation of what could be achieved with such a system.

Conclusion

The purpose of this chapter was to assess the sky coverage of the SLAO system. The first part consisted in an estimation of the wavelength integration range for the SCAO sensor to determine the lowest magnitude achievable for the NGS for which the truth correction is still effective. Taking into account all the parameters, the best compromise seems to be a global JHK-band integration range, leading to a minimum NGS magnitude of ≈ 16.5. *The second part was estimating the sky coverage that could be reached with such a magnitude: although more than one star will be located inside METIS FoV at low galactic latitude, this is not true anymore for higher galactic latitudes. However, several parameters in this study might indicate that the cumulative number of stars at* $m_K = 16.5$ *is higher, leading to a higher sky coverage that could reach the* 100 %.

Table 8.1: Sky coverage estimations for several galactic latitudes

Galactic Latitude	**Low** $b < 30°$	**Medium** $30° < b < 60°$	**Large** $b > 60°$
Star density at $m_K = 16.5$	2×10^4 #/ deg^2	3.5×10^3 #/ deg^2	2×10^3 #/ deg^2
# stars in METIS FoV (30")	1.1	0.19	0.11
FoV for 100% sky coverage	28.6"	1′08.2"	1′30.5"

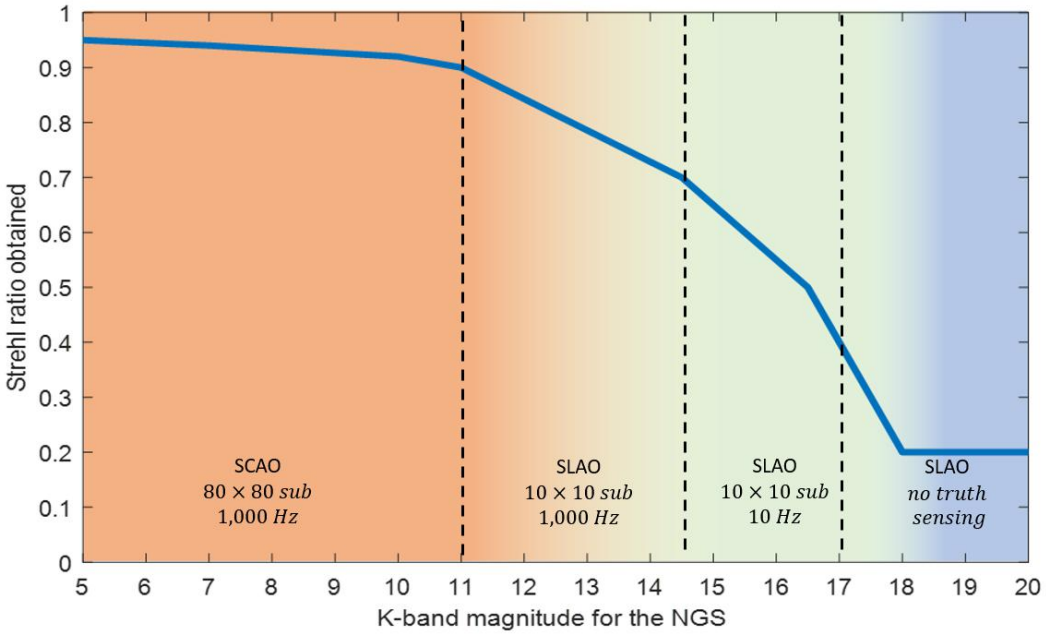

Figure 8.8: Strehl evolution according to the NGS magnitude. The trends for the SLAO system have not been precisely observed, and they have been plotted regarding the limit conditions of the system. The SLAO without truth is estimated at 20%, but the real performances might be higher for most of the sodium layer profiles.

Conclusion

This work has been performed to create a working solution for the Single Laser Adaptive Optics for the ELT instrument METIS. The motivations are based on the limitation of the current Adaptive Optics system planned for METIS: although the Strehl performances will be very high (> 90% Strehl), the magnitude from the NGS required to perform the high-resolution observations is relatively high $m_K < 11$ and limits the sky coverage of the system to about 1%. It limits considerably the possibility to use high-resolution for extra-galactic science, where the probability to find a bright enough NGS is almost zero. The solution is thus to create a LGS from the 90 km sodium layer, launched from one of the LLT on the side of the ELT. It enfranchises the system from the NGS magnitude constraint, allowing high-resolution observations in almost all the sky. The context of this work is particular: although the METIS instrument is already financed, the SLAO system is out of the baseline yet. This project is the opportunity to prove at ESO that a SLAO system would be possible for METIS, giving good Strehl performances for minimal cost, weight, and size.

This thesis needed to find plausible solutions for the several stages that are included in the implementation of the SLAO system. First of all, a beam splitter was required to separate the LGS light from the science one, since their footprint is coincident. The annular mirror seems to be the best compromise, although it includes to carefully chose the inner diameter to enable a science FoV as broad a possible while keeping the science beam intact while being able to perform observations at several zenith angles. A solution has been proposed in Chapter 2, but it needs to be investigated by scientists to see what is the best compromise relatively to the needs of the observations.

Once the LGS beam separated from the science one, the information from the atmospheric wavefront needs to be recovered: this is the purpose of the high-order SH-WFS. This sensor has to deal with the beam elongation, something that was already seen for the VLT LGS system but becomes much more critical in the case of the 37-meter aperture ELT. The beam becomes so elongated in that case that it has to be cropped to fit in the SH-WFS FoV. However, this is created instabilities as the system is not able to perform the centroiding of the beam properly since some information might have been lost. The solution found was to use a large FoV of 10", while still keeping the sampling relatively low at $0.5"/pix$ and using a maximum of 800×800 pixels so that the system can still be run at $1,000\ Hz$. This configuration for the LGS WFS allows to get rid of the instabilities but relies a lot on the sodium layer profile. Some fixed patterns are thus observed, patterns that could be corrected by running an unbiased WFS coupled with a NGS.

The so-called truth sensing is mandatory for such a system to keep high Strehl ratio for long exposure. The SCAO PWFS already built in METIS is planned to be used, allowing the detection of the tip/tilt invisible for the LGS WFS and the offsets patterns created by it. The purpose of the Chapter 4 was to determine whether it was possible or not to correct the offsets, and what were the requirements for the NGS magnitude. An AO simulator in MATLAB has been created for this reason, using the residuals provided by the YAO simulations where the LGS and tip/tilt corrections have already been made. It has been possible to infer that the LGS can be corrected by a 10×10 PWFS at a frequency of 10 Hz, with a brightness for the NGS $m_K < 16.5$.

Now that the reasons for the optimal parameters has been explained, it has been possible to calculate the Strehl performances for the SLAO system with the YAO simulator. This has been performed in Chapter 5, where the results seem to indicate that a 60% Strehl ratio seems plausible while counting on the truth sensing when the sodium layer profile damages effectively the resolution of the system. These results have been confirmed by the ESO's AO experts and the results of their simulations made on an independent software OCTOPUS. In future research, it could be interesting to write a truth sensing system directly in YAO instead of doing it independently in MATLAB. Nevertheless, these first results are encouraging.

Once the simulations made, the optical design of such a system has been made in Chapter 6. This has been performed with ZEMAX and used the SH-WFS specifications that have been defined in Chapter 3. The system created can deliver, under any zenith angle, low aberration (typically a diffraction pattern with a width smaller than the pixel size of 24 μm), while focusing the pupil image on the lenslet and the LGS beam on the detector. Although not perfect, this system might be a good start for future optical designs. This part also includes a

first mechanical design made with AUTODESK, in addition to a first weight and size estimation of the SLAO system.

Finally, the sky coverage of the system has been investigated, with a tentative to optimize the wavelength range to increase it. The researches in Chapter 8 have taken into account the behavior of the atmosphere and the system regarding the near-infrared wavelength used. It has been determined, under some assumptions about the spectrum of the NGS, that a global JHK-band filter seems to provide the maximum SNR at a given magnitude m_K, leading to a sky coverage of almost 100%.

The work performed during the Master thesis will be used both as a proof that the SLAO system for METIS is viable and as a basis for a more sophisticated design. The appendices describe how the science made with a full resolution mid-infrared instrument could be interesting. This ability has never been seen before, and not even the JWST will be able to have such a high spatial resolution. However, a lot of work still needs to be performed before observing $H-\alpha$ emissions from high-redshift galaxies with the SLAO system of the ELT/METIS.

Bibliography

[1] Tibor Agocs. Metis troughput budget. Technical report, NOVA, 2018.

[2] A. Alonso-Herrero, G. H. Rieke, M. J. Rieke, and N. Z. Scoville. Massive Star Formation in Luminous Infrared Galaxies: Giant H II Regions and Their Relation to Super-Star Clusters. AJ, 124:166–182, July 2002. doi: 10.1086/340963.

[3] L. Armus, J. M. Mazzarella, A. S. Evans, J. A. Surace, D. B. Sanders, K. Iwasawa, D. T. Frayer, J. H. Howell, B. Chan, A. Petric, T. Vavilkin, D. C. Kim, S. Haan, H. Inami, E. J. Murphy, P. N. Appleton, J. E. Barnes, G. Bothun, C. R. Bridge, V. Charmandaris, J. B. Jensen, L. J. Kewley, S. Lord, B. F. Madore, J. A. Marshall, J. E. Melbourne, J. Rich, S. Satyapal, B. Schulz, H. W. W. Spoon, E. Sturm, V. U, S. Veilleux, and K. Xu. GOALS: The Great Observatories All-Sky LIRG Survey. PASP, 121:559, June 2009. doi: 10.1086/600092.

[4] P. Barriga, B. Sedghi, M. Dimmler, and N. Kornweibel. Status of E-ELT M5 scale-one demonstrator. In *Ground-based and Airborne Telescopes V*, volume 9145 of Proc. SPIE, page 91451O, July 2014. doi: 10.1117/12.2056821.

[5] S. V. W. Beckwith, M. Stiavelli, A. M. Koekemoer, J. A. R. Caldwell, H. C. Ferguson, R. Hook, R. A. Lucas, L. E. Bergeron, M. Corbin, S. Jogee, N. Panagia, M. Robberto, P. Royle, R. S. Somerville, and M. Sosey. The Hubble Ultra Deep Field. AJ, 132:1729–1755, November 2006. doi: 10.1086/507302.

[6] P. Beirão, B. R. Brandl, P. N. Appleton, B. Groves, L. Armus, N. M. Förster Schreiber, J. D. Smith, V. Charmandaris, and J. R. Houck. Spatially Resolved Spitzer IRS Spectroscopy of the Central Region of M82. ApJ, 676:304-316, March 2008. doi: 10.1086/527343.

[7] P. Beirão, P. N. Appleton, B. R. Brandl, M. Seibert, T. Jarrett, and J. R. Houck. Powerful H_2 Emission and Star Formation on the Interacting Galaxy System Arp 143: Observations with Spitzer and Galex. ApJ, 693: 1650–1665, March 2009. doi: 10.1088/0004-637X/693/2/1650.

[8] Thomas Bertram. Wavefront sensing for. In *WFSensing in the VLT/ELT era II*, 2017.

[9] L. Blanco. Lgs spot truncation mitigation in elts: optimizing the pixel usage. In *AO4ELT*. Laboratoire d'Astrophysique de Marseille, 2017.

[10] B. R. Brandl, J. Bernard-Salas, H. W. W. Spoon, D. Devost, G. C. Sloan, S. Guilles, Y. Wu, J. R. Houck, D. W. Weedman, L. Armus, P. N. Appleton, B. T. Soifer, V. Charmandaris, L. Hao, S. J. Higdon J. A. Marshall, and T. L. Herter. The mid-infrared properties of starburst galaxies from spitzer-irs spectroscopy. *The Astrophysical Journal*, 653(2):1129, 2006. URL http://stacks.iop.org/0004-637X/653/i=2/a=1129.

[11] B. R. Brandl, L. Snijders, M. den Brok, D. G. Whelan, B. Groves, P. van der Werf, V. Charmandaris, J. D. Smith, L. Armus, R. C. Kennicutt, Jr., and J. R. Houck. Spitzer-IRS Study of the Antennae Galaxies NGC 4038/39. ApJ, 699:1982-2001, July 2009. doi: 10.1088/0004-637X/699/2/1982.

[12] B. R. Brandl, N. L. Martín-Hernández, D. Schaerer, M. Rosenberg, and P. P. van der Werf. High resolution IR observations of the starburst ring in NGC 7552. One ring to rule them all? A&A, 543:A61, July 2012. doi: 10.1051/0004-6361/201117568.

[13] B. R. Brandl, M. Feldt, A. Glasse, M. Guedel, S. Heikamp, M. Kenworthy, R. Lenzen, M. R. Meyer, F. Molster, S. Paalvast, E. J. Pantin, S. P. Quanz, E. Schmalzl, R. Stuik, L. Venema, and C. Waelkens. METIS: the mid-infrared E-ELT imager and spectrograph. In *Ground-based and Airborne Instrumentation for Astronomy V*, volume 9147 of Proc. SPIE, page 914721, August 2014. doi: 10.1117/12.2056468.

[14] Bernhard Brandl, editor. *The Future of Ground-based extragalactic MID-IR astronomy OR Extragalactic science with METIS on the E-ELT*, 2015.

[15] Bernhard R Brandl, Tibor Agócs, Gabby Aitink-Kroes, Thomas Bertram, Felix Bettonvil, Roy van Boekel, Olivier Boulade, Markus Feldt, Alistair Glasse, Adrian Glauser, et al. Status of the mid-infrared e-elt imager and spectrograph metis. In *Ground-based and Airborne Instrumentation for Astronomy VI*, volume 9908, page 990820. International Society for Optics and Photonics, 2016.

[16] L. Burtscher, K. Meisenheimer, K. R. W. Tristram, W. Jaffe, S. F. Hönig, R. I. Davies, M. Kishimoto, J.-U. Pott, H. Röttgering, M. Schartmann, G. Weigelt, and S. Wolf. A diversity of dusty AGN tori. Data release for the VLTI/MIDI AGN Large Program and first results for 23 galaxies. A&A, 558:A149, October 2013. doi: 10.1051/0004-6361/201321890.

[17] R. Cañameras, N. Nesvadba, R. Kneissl, B. Frye, R. Gavazzi, S. Koenig, E. Le Floc'h, M. Limousin, I. Oteo, and D. Scott. Planck's dusty GEMS. IV. Star formation and feedback in a maximum starburst at z = 3 seen at 60-pc resolution. A&A, 604:A117, August 2017. doi: 10.1051/0004-6361/201630186.

[18] F. Cantalloube, T. Bertra, A. Obereder, and R. Stuik. Poster: Status of the scao design and simulations. 2017.

[19] C. M. Casey, D. Narayanan, and A. Cooray. Dusty star-forming galaxies at high redshift. Phys. Rep., 541: 45–161, August 2014. doi: 10.1016/j.physrep.2014.02.009.

[20] Y.-Y. Chang, E. Le Floc'h, S. Juneau, E. da Cunha, M. Salvato, F. Civano, S. Marchesi, J. M. Gabor, O. Ilbert, C. Laigle, H. J. McCracken, B.-C. Hsieh, and P. Capak. Obscured active galactic nuclei triggered in compact star-forming galaxies. MNRAS, 466:L103–L107, March 2017. doi: 10.1093/mnrasl/slw247.

[21] R. Davies and M. Kasper. Adaptive Optics for Astronomy. ARA&A, 50:305–351, September 2012. doi: 10.1146/annurev-astro-081811-125447.

[22] R. Davies, J. Schubert, M. Hartl, J. Alves, Y. Clénet, F. Lang-Bardl, H. Nicklas, J.-U. Pott, R. Ragazzoni, E. Tolstoy, T. Agocs, H. Anwand-Heerwart, S. Barboza, P. Baudoz, R. Bender, P. Bizenberger, A. Boccaletti, W. Boland, P. Bonifacio, F. Briegel, T. Buey, F. Chapron, M. Cohen, O. Czoske, S. Dreizler, R. Falomo, P. Feautrier, N. Förster Schreiber, E. Gendron, R. Genzel, M. Glück, D. Gratadour, R. Greimel, F. Grupp, M. Häuser, M. Haug, J. Hennawi, H. J. Hess, V. Hörmann, R. Hofferbert, U. Hopp, Z. Hubert, D. Ives, W. Kausch, F. Kerber, H. Kravcar, K. Kuijken, F. Lang-Bardl, M. Leitzinger, K. Leschinski, D. Massari, S. Mei, F. Merlin, L. Mohr, A. Monna, F. Müller, R. Navarro, M. Plattner, N. Przybilla, R. Ramlau, S. Ramsay, T. Ratzka, P. Rhode, J. Richter, H.-W. Rix, G. Rodeghiero, R.-R. Rohloff, G. Rousset, R. Ruddenklau, V. Schaffenroth, J. Schlichter, A. Sevin, R. Stuik, E. Sturm, J. Thomas, N. Tromp, M. Turatto, G. Verdoes-Kleijn, F. Vidal, R. Wagner, M. Wegner, W. Zeilinger, B. Ziegler, and G. Zins. MICADO: first light imager for the E-ELT. In *Ground-based and Airborne Instrumentation for Astronomy VI*, volume 9908 of Proc. SPIE, page 99081Z, August 2016. doi: 10.1117/12.2233047.

[23] E Diolaiti, P Ciliegi, R Abicca, G Agapito, C Arcidiacono, A Baruffolo, M Bellazzini, V Biliotti, M Bonaglia, G Bregoli, et al. Maory: adaptive optics module for the e-elt. In *Adaptive Optics Systems V*, volume 9909, page 99092D. International Society for Optics and Photonics, 2016.

[24] F. Eisenhauer, R. Abuter, K. Bickert, F. Biancat-Marchet, H. Bonnet, J. Brynnel, R. D. Conzelmann, B. Delabre, R. Donaldson, J. Farinato, E. Fedrigo, R. Genzel, N. N. Hubin, C. Iserlohe, M. E. Kasper, M. Kissler-Patig, G. J. Monnet, C. Roehrle, J. Schreiber, S. Stroebele, M. Tecza, N. A. Thatte, and H. Weisz. SINFONI - Integral field spectroscopy at 50 milli-arcsecond resolution with the ESO VLT. In M. Iye and A. F. M. Moorwood, editors, *Instrument Design and Performance for Optical/Infrared Ground-based Telescopes*, volume 4841 of Proc. SPIE, pages 1548–1561, March 2003. doi: 10.1117/12.459468.

[25] European Southern Observatory ESO. E-elt main structure, 2011. URL https://www.eso.org/sci/facilities/eelt/telescope/mstructure/.

[26] *Large format science detectors and high speed sub-electron noise sensors for ground-based astronomy*, 2017. ESO (European Southern Observatory).

[27] J. A. Fernández-Ontiveros, K. R. W. Tristram, S. Hönig, P. Gandhi, and G. Weigelt. Embedded AGN and star formation in the central 80 pc of IC 3639. *ArXiv e-prints*, November 2017.

[28] T. Fusco. Atlas phase a study, executive summary. Technical report, ONERA, 2010.

[29] E. Galliano, D. Alloin, E. Pantin, G. L. Granato, P. Delva, L. Silva, P. O. Lagage, and P. Panuzzo. Extremely massive young clusters in NGC 1365. A&A, 492:3–22, December 2008. doi: 10.1051/0004-6361:20077621.

[30] R.C. Gonzalez and R.E. Woods. *Digital Image Processing*. Pearson/Prentice Hall, 2008. ISBN 9780131687288. URL https://books.google.fr/books?id=8uGOnjRGEzoC.

[31] N. A. Grogin, D. D. Kocevski, S. M. Faber, H. C. Ferguson, A. M. Koekemoer, A. G. Riess, V. Acquaviva, D. M. Alexander, O. Almaini, M. L. N. Ashby, M. Barden, E. F. Bell, F. Bournaud, T. M. Brown, K. I. Caputi, S. Casertano, P. Cassata, M. Castellano, P. Challis, R.-R. Chary, E. Cheung, M. Cirasuolo, C. J. Conselice, A. Roshan Cooray, D. J. Croton, E. Daddi, T. Dahlen, R. Davé, D. F. de Mello, A. Dekel, M. Dickinson, T. Dolch, J. L. Donley, J. S. Dunlop, A. A. Dutton, D. Elbaz, G. G. Fazio, A. V. Filippenko, S. L. Finkelstein, A. Fontana, J. P. Gardner, P. M. Garnavich, E. Gawiser, M. Giavalisco, A. Grazian, Y. Guo, N. P. Hathi, B. Häussler, P. F. Hopkins, J.-S. Huang, K.-H. Huang, S. W. Jha, J. S. Kartaltepe, R. P. Kirshner, D. C. Koo, K. Lai, K.-S. Lee, W. Li, J. M. Lotz, R. A. Lucas, P. Madau, P. J. McCarthy, E. J. McGrath, D. H. McIntosh, R. J. McLure, B. Mobasher, L. A. Moustakas, M. Mozena, K. Nandra, J. A. Newman, S.-M. Niemi, K. G. Noeske, C. J. Papovich, L. Pentericci, A. Pope, J. R. Primack, A. Rajan, S. Ravindranath, N. A. Reddy, A. Renzini, H.-W. Rix, A. R. Robaina, S. A. Rodney, D. J. Rosario, P. Rosati, S. Salimbeni, C. Scarlata, B. Siana, L. Simard, J. Smidt, R. S. Somerville, H. Spinrad, A. N. Straughn, L.-G. Strolger, O. Telford, H. I. Teplitz, J. R. Trump, A. van der Wel, C. Villforth, R. H. Wechsler, B. J. Weiner, T. Wiklind, V. Wild, G. Wilson, S. Wuyts, H.-J. Yan, and M. S. Yun. CANDELS: The Cosmic Assembly Near-infrared Deep Extragalactic Legacy Survey. ApJS, 197:35, December 2011. doi: 10.1088/0067-0049/197/2/35.

[32] M. G. Haehnelt and G. Kauffmann. The correlation between black hole mass and bulge velocity dispersion in hierarchical galaxy formation models. MNRAS, 318:L35–L38, November 2000. doi: 10.1046/j.1365-8711.2000.03989.x.

[33] W. E. Harris, G. L. H. Harris, and M. Alessi. A Catalog of Globular Cluster Systems: What Determines the Size of a Galaxy's Globular Cluster Population? ApJ, 772:82, August 2013. doi: 10.1088/0004-637X/772/2/82.

[34] Paul Hickson. Atmospheric and adaptive optics. *The Astronomy and Astrophysics Review*, 22(1):76, Nov 2014. ISSN 1432-0754. doi: 10.1007/s00159-014-0076-9. URL https://doi.org/10.1007/s00159-014-0076-9.

[35] S. Ikarashi, R. J. Ivison, K. I. Caputi, I. Aretxaga, J. S. Dunlop, B. Hatsukade, D. H. Hughes, D. Iono, T. Izumi, R. Kawabe, K. Kohno, C. D. P. Lagos, K. Motohara, K. Nakanishi, K. Ohta, Y. Tamura, H. Umehata, G. W. Wilson, K. Yabe, and M. S. Yun. Compact Starbursts in z = 3-6 Submillimeter Galaxies Revealed by ALMA. ApJ, 810:133, September 2015. doi: 10.1088/0004-637X/810/2/133.

[36] S. Ikarashi, R. J. Ivison, K. I. Caputi, K. Nakanishi, C. D. P. Lagos, M. L. N. Ashby, I. Aretxaga, J. S. Dunlop, B. Hatsukade, D. H. Hughes, D. Iono, T. Izumi, R. Kawabe, K. Kohno, K. Motohara, K. Ohta, Y. Tamura, H. Umehata, G. W. Wilson, K. Yabe, and M. S. Yun. Extremely Red Submillimeter Galaxies: New z = 4-6 Candidates Discovered using ALMA and Jansky VLA. ApJ, 835:286, February 2017. doi: 10.3847/1538-4357/835/2/286.

[37] A. Jones, S. Noll, W. Kausch, C. Szyszka, and S. Kimeswenger. An advanced scattered moonlight model for Cerro Paranal. A&A, 560:A91, December 2013. doi: 10.1051/0004-6361/201322433.

[38] R. C. Kennicutt, Jr. Star Formation in Galaxies Along the Hubble Sequence. ARA&A, 36:189–232, 1998. doi: 10.1146/annurev.astro.36.1.189.

[39] C. Kitchin. *Galaxies in Turmoil: The Active and Starburst Galaxies and the Black Holes that Drive them*. Springer, 2007.

[40] C. R. Kitchin. *Astronomy Techniques: An Introduction to Practical Astronomy*. Taylor and Francis Group, LLC, 2014.

[41] P. Kroupa. The Initial Mass Function of Stars: Evidence for Uniformity in Variable Systems. *Science*, 295:82–91, January 2002. doi: 10.1126/science.1067524.

[42] Paolo La Penna, S Ströbele, E Aller Carpentier, J Argomedo, R Arsenault, RD Conzelmann, B Delabre, R Donaldson, M Duchateau, E Fedrigo, et al. Galacsi integration and functional tests. In *Adaptive Optics Systems IV*, volume 9148, page 91482V. International Society for Optics and Photonics, 2014.

[43] C. Laigle, H. J. McCracken, O. Ilbert, B. C. Hsieh, I. Davidzon, P. Capak, G. Hasinger, J. D. Silverman, C. Pichon, J. Coupon, H. Aussel, D. Le Borgne, K. Caputi, P. Cassata, Y.-Y. Chang, F. Civano, J. Dunlop, J. Fynbo, J. S. Kartaltepe, A. Koekemoer, O. Le Fèvre, E. Le Floc'h, A. Leauthaud, S. Lilly, L. Lin, S. Marchesi, B. Milvang-Jensen, M. Salvato, D. B. Sanders, N. Scoville, V. Smolcic, M. Stockmann, Y. Taniguchi, L. Tasca, S. Toft, M. Vaccari, and J. Zabl. The COSMOS2015 Catalog: Exploring the $1 \leq z \leq 6$ Universe with Half a Million Galaxies. ApJS, 224:24, June 2016. doi: 10.3847/0067-0049/224/2/24.

[44] E. Le Floc'h, V. Charmandaris, K. Gordon, W. J. Forrest, B. Brandl, D. Schaerer, M. Dessauges-Zavadsky, and L. Armus. The First Infrared Study of the Close Environment of a Long Gamma-Ray Burst. ApJ, 746: 7, February 2012. doi: 10.1088/0004-637X/746/1/7.

[45] Emeric Le Floch́. Extragalactic science with metis. Technical report, CEA-Saclay, 2016.

[46] Miska Le Louarn. Metis slao simulations. Technical report, ESO, 2018.

[47] Roberts Jr. Lewis C., Bradford L. William, Neyman Christopher R., and Liu Alan Z. Measurements of mesospheric sodium abundance above the hawaiian islands. *Publications of the Astronomical Society of the Pacific*, 119(857):787–792, 2007. URL http://www.jstor.org/stable/10.1086/520626.

[48] D. Lutz, S. Berta, A. Contursi, N. M. Förster Schreiber, R. Genzel, J. Graciá-Carpio, R. Herrera-Camus, H. Netzer, E. Sturm, L. J. Tacconi, K. Tadaki, and S. Veilleux. The far-infrared emitting region in local galaxies and QSOs: Size and scaling relations. A&A, 591:A136, June 2016. doi: 10.1051/0004-6361/201527706.

[49] Enrico Marchetti. Relevant atmospheric parameters for E-ELT AO analysis and simulations. Technical report, European Space Observatory, 2015.

[50] J. C. Muñoz-Mateos, K. Sheth, M. Regan, T. Kim, J. Laine, S. Erroz-Ferrer, A. Gil de Paz, S. Comeron, J. Hinz, E. Laurikainen, H. Salo, E. Athanassoula, A. Bosma, A. Y. K. Bouquin, E. Schinnerer, L. Ho, D. Zaritsky, D. A. Gadotti, B. Madore, B. Holwerda, K. Menéndez-Delmestre, J. H. Knapen, S. Meidt, M. Querejeta, T. Mizusawa, M. Seibert, S. Laine, and H. Courtois. The Spitzer Survey of Stellar Structure in Galaxies (S^4G): Stellar Masses, Sizes, and Radial Profiles for 2352 Nearby Galaxies. ApJS, 219:3, July 2015. doi: 10.1088/0067-0049/219/1/3.

[51] Takao Nakagawa. Spica mission for mid-and far-infrared astronomy. In *Space Telescopes and Instrumentation 2008: Optical, Infrared, and Millimeter*, volume 7010, page 70100H. International Society for Optics and Photonics, 2008.

[52] H. Netzer. Revisiting the Unified Model of Active Galactic Nuclei. ARA&A, 53:365–408, August 2015. doi: 10.1146/annurev-astro-082214-122302.

[53] S. Noll, W. Kausch, M. Barden, A. M. Jones, C. Szyszka, S. Kimeswenger, and J. Vinther. An atmospheric radiation model for Cerro Paranal. I. The optical spectral range. A&A, 543:A92, July 2012. doi: 10.1051/0004-6361/201219040.

[54] I. Oteo, M. A. Zwaan, R. J. Ivison, I. Smail, and A. D. Biggs. ALMACAL I: First Dual-band Number Counts from a Deep and Wide ALMA Submillimeter Survey, Free from Cosmic Variance. ApJ, 822:36, May 2016. doi: 10.3847/0004-637X/822/1/36.

[55] I. Oteo, R. J. Ivison, M. Negrello, I. Smail, I. Pérez-Fournon, M. Bremer, G. De Zotti, S. A. Eales, D. Farrah, P. Temi, D. L. Clements, A. Cooray, H. Dannerbauer, S. Duivenvoorden, L. Dunne, E. Ibar, A. J. R. Lewis, R. Marques-Chaves, P. Martínez-Navajas, M. J. Michałowski, A. Omont, S. Oliver, D. Riechers, D. Scott, and P. van der Werf. Witnessing the birth of the red sequence: the physical scale and morphology of dust emission in hyper-luminous starbursts in the early Universe. *ArXiv e-prints*, September 2017.

[56] I. Oteo, M. A. Zwaan, R. J. Ivison, I. Smail, and A. D. Biggs. ALMACAL II: Extreme Star Formation Rate Densities in Dusty Starbursts Revealed by ALMA 20 mas Resolution Imaging. ApJ, 837:182, March 2017. doi: 10.3847/1538-4357/aa5da4.

[57] T. Pfrommer and P. Hickson. High resolution mesospheric sodium properties for adaptive optics applications. A&A, 565:A102, May 2014. doi: 10.1051/0004-6361/201423460.

[58] Thomas Pfrommer, Paul Hickson, and Chiao Yao She. A large aperture sodium fluorescence lidar with very high resolution for mesopause dynamics and adaptive optics studies. *Geophysical Research Letters*, 36(15), 8 2009. ISSN 1944-8007. doi: 10.1029/2009GL038802. URL http:https://doi.org/10.1029/2009GL038802.

[59] J. Piqueras López, L. Colina, S. Arribas, M. Pereira-Santaella, and A. Alonso-Herrero. VLT-SINFONI sub-kpc study of the star formation in local LIRGs and ULIRGs. Analysis of the global Σ_{SFR} structure and characterisation of individual star-forming clumps. A&A, 590:A67, May 2016. doi: 10.1051/0004-6361/201527671.

[60] J. T. Radomski, C. Packham, N. A. Levenson, E. Perlman, L. L. Leeuw, H. Matthews, R. Mason, J. M. De Buizer, C. M. Telesco, and M. Orduna. Gemini Imaging of Mid-Infrared Emission from the Nuclear Region of Centaurus A. ApJ, 681:141-150, July 2008. doi: 10.1086/587771.

[61] F. Renaud, F. Bournaud, K. Kraljic, and P.-A. Duc. Starbursts triggered by intergalactic tides andinterstellar compressive turbulence. MNRAS, 442:L33–L37, July 2014. doi: 10.1093/mnrasl/slu050.

[62] Michael E Ressler, Hyung Cho, Richard AM Lee, Kalyani G Sukhatme, John J Drab, George Domingo, Mark E McKelvey, Robert E McMurray, and Jessie L Dotson. Performance of the jwst/miri si: As detectors. In *High Energy, Optical, and Infrared Detectors for Astronomy III*, volume 7021, page 70210O. International Society for Optics and Photonics, 2008.

[63] Yvon Rio, Pierre-Olivier Lagage, Didier Dubreuil, Gilles A Durand, Charles Lyraud, Jan-Willem Pel, Johannes CM de Haas, Anton Schoenmaker, and Hoite Tolsma. Visir: the mid-infrared imager and spectrometer for the vlt. In *Infrared Astronomical Instrumentation*, volume 3354, pages 615–627. International Society for Optics and Photonics, 1998.

[64] F. Roddier. *Adaptive Optics in Astronomy*. Cambridge University Press, November 2004.

[65] Matthias Rosensteiner. Cumulative reconstructor: fast wavefront reconstruction algorithm for extremely large telescopes. *J. Opt. Soc. Am. A*, 28(10):2132–2138, Oct 2011. doi: 10.1364/JOSAA.28.002132. URL http://josaa.osa.org/abstract.cfm?URI=josaa-28-10-2132.

[66] Matthias Rosensteiner. Wavefront reconstruction for extremely large telescopes via cure with domain decomposition. *J. Opt. Soc. Am. A*, 29(11):2328–2336, Nov 2012. doi: 10.1364/JOSAA.29.002328. URL http://josaa.osa.org/abstract.cfm?URI=josaa-29-11-2328.

[67] E. E. Salpeter. Energy production in stars. *Vistas in Astronomy*, 1:283–290, 1955. doi: 10.1016/0083-6656(55)90037-4.

[68] E. Schmalzl and J. Meisner, editors. *The METIS simulator*, 2013.

[69] L. Schreiber, I. Foppiani, C. Robert, E. Diolaiti, J.–M. Conan, and M. Lombini. Laser guide stars for extremely large telescopes: efficient shack–hartmann wavefront sensor design using the weighted centre–of–gravity algorithm. *Monthly Notices of the Royal Astronomical Society*, 396(3):1513–1521, 2009. doi: 10.1111/j.1365-2966.2009.14797.x. URL http://dx.doi.org/10.1111/j.1365-2966.2009.14797.x.

[70] N. Scoville, H. Aussel, M. Brusa, P. Capak, C. M. Carollo, M. Elvis, M. Giavalisco, L. Guzzo, G. Hasinger, C. Impey, J.-P. Kneib, O. LeFevre, S. J. Lilly, B. Mobasher, A. Renzini, R. M. Rich, D. B. Sanders, E. Schinnerer, D. Schminovich, P. Shopbell, Y. Taniguchi, and N. D. Tyson. The Cosmic Evolution Survey (COSMOS): Overview. ApJS, 172:1–8, September 2007. doi: 10.1086/516585.

[71] ES Selex. *SAPHIRA Avalanche Photodiode Array*, 2014.

[72] T. Shibuya, M. Ouchi, and Y. Harikane. Morphologies of ≈ 190,000 Galaxies at z = 0-10 Revealed with HST Legacy Data. I. Size Evolution. ApJS, 219:15, August 2015. doi: 10.1088/0067-0049/219/2/15.

[73] MF Skrutskie, RM Cutri, R Stiening, MD Weinberg, S Schneider, JM Carpenter, Capps Beichman, R Capps, T Chester, J Elias, et al. The two micron all sky survey (2mass). *The Astronomical Journal*, 131(2):1163, 2006.

[74] L. S. Sparke and J. S. Gallagher, III. *Galaxies in the Universe: An Introduction*. Cambridge University Press, 2007.

[75] N. A. Thatte, F. Clarke, I. Bryson, H. Schnetler, M. Tecza, R. M. Bacon, A. Remillieux, E. Mediavilla, J. M. Herreros Linares, S. Arribas, C. J. Evans, D. W. Lunney, T. Fusco, K. O'Brien, I. A. Tosh, D. J. Ives, G. Finger, R. Houghton, R. L. Davies, J. D. Lynn, J. R. Allen, S. D. Zieleniewski, S. Kendrew, V. Ferraro-Wood, A. Pécontal-Rousset, J. Kosmalski, J. Richard, A. Jarno, A. M. Gallie, D. M. Montgomery, D. Henry, G. Zins, D. Freeman, B. García-Lorenzo, L. F. Rodríguez-Ramos, J. S. C. Revuelta, E. Hernandez Suarez, A. Bueno-Bueno, J. V. Gigante-Ripoll, A. Garcia, K. Dohlen, and B. Neichel. HARMONI: the first light integral field spectrograph for the E-ELT. In *Ground-based and Airborne Instrumentation for Astronomy V*, volume 9147 of Proc. SPIE, page 914725, August 2014. doi: 10.1117/12.2055436.

[76] G. A. Tyler. Rapid evaluation of d_0: the effective diameter of a laser- guide-star adaptive-optics system. *Journal of the Optical Society of America A*, 11:325–338, January 1994. doi: 10.1364/JOSAA.11.000325.

[77] R. Tyson. *Principles of Adaptive Optics, Third Edition*. Series in Optics and Optoelectronics. CRC Press, 2010. ISBN 9781439808597. URL https://books.google.nl/books?id=x1PUYBvHHqcC.

[78] R.K. Tyson and B.W. Frazier. *Field Guide to Adaptive Optics*. SPIE field guides. Society of Photo Optical, 2012. ISBN 9780819490179. URL https://books.google.nl/books?id=_otytgAACAAJ.

[79] A. van der Wel, M. Franx, P. G. van Dokkum, R. E. Skelton, I. G. Momcheva, K. E. Whitaker, G. B. Brammer, E. F. Bell, H.-W. Rix, S. Wuyts, H. C. Ferguson, B. P. Holden, G. Barro, A. M. Koekemoer, Y.-Y. Chang, E. J. McGrath, B. Häussler, A. Dekel, P. Behroozi, M. Fumagalli, J. Leja, B. F. Lundgren, M. V. Maseda, E. J. Nelson, D. A. Wake, S. G. Patel, I. Labbé, S. M. Faber, N. A. Grogin, and D. D. Kocevski. 3D-HST+CANDELS: The Evolution of the Galaxy Size-Mass Distribution since z = 3. ApJ, 788:28, June 2014. doi: 10.1088/0004-637X/788/1/28.

[80] MW Werner, TL Roellig, FJ Low, GH Rieke, M Rieke, WF Hoffmann, E Young, JR Houck, B Brandl, GG Fazio, et al. The spitzer space telescope mission. *The Astrophysical Journal Supplement Series*, 154 (1):1, 2004.

[81] P. L. Wizinowich, D. Le Mignant, A. H. Bouchez, R. D. Campbell, J. C. Y. Chin, A. R. Contos, M. A. van Dam, S. K. Hartman, E. M. Johansson, R. E. Lafon, H. Lewis, P. J. Stomski, D. M. Summers, C. G. Brown, P. M. Danforth, C. E. Max, and D. M. Pennington. The W. M. Keck Observatory Laser Guide Star Adaptive Optics System: Overview. PASP, 118:297–309, February 2006. doi: 10.1086/499290.

Appendices

The 3 next appendices that will be presented here are a part of the report that has been written during the first the first three months of internship at CEA-Saclay. This part has been mainly focused on the research of suitable science cases for the ELT/METIS, mostly by simulating the expected performances on scientific objects. This work has not been performed during the thesis project. However, it gives a good overview about the kind of science that could be enabled with a working SLAO system, provided that the sky coverage is sufficient.

The Appendix A will cover a systematic study that has been made on the COSMOS database to identify the type and occurrence of typical objects detectable by the ELT/METIS. Then the Appendix B will review more in details the science that can be learned from such objects, and will try to constrain more the physical parameters values such as the Star Formation Rate (SFR) that are required. Finally, the Appendix C will take existing objects that are already observed and try to simulate what would be the ELT/METIS performances on these objects, put at several distances.

Chapter A

Research of observable candidates within the COSMOS deep survey and GOALS and S4G legacies

This part will deal with the types of objects detectable by the instrument. Based on the observations made by several legacy studies such as GOALS, S4G or COSMOS, it is possible to determine the proportion of objects that would be detectable by the ELT/METIS. Moreover, instruments such as the JWST or SPICA will be launched before the first lights of METIS, and they will operate as the same wavelengths as the instrument. For this reason, the objects observed by METIS have also to be scientifically relevant, especially at a time when the JWST will have been launched 10 years ago.

Contents

The analysis of the cases was simple: establishing a list of objects with criteria (flux at a certain wavelength, AGN fraction), retrieving the images of these objects and analyzing whether a detection by METIS would be possible or not, based on the surface brightness of these images. There is a simple reason why the images are required: The literature in Astronomy references well the flux of astronomical objects or even their luminosity. If the research were about punctual objects or global fluxes from them, it would have been easier to look for papers mentioning these objects, or even directly used catalogs such as the one made for COSMOS (Laigle et al., 2016 [43]) or CANDELS (Grogin et al., 2011 [31]). However, the parameter that needs to be estimated here is

the surface brightness of the several objects, which is particularly relevant for METIS because of the very high resolution provided by the ELT. This is the reason why downloading images becomes mandatory: the sources will not be punctual for ELT/METIS, and therefore the precise surface brightness of each pixel in the image needs to be looked.

A.1. The GOALS survey

A.1.1. Presentation of the survey

The Great Observatories All-sky LIRGS Survey (cf Armus et al., 2009 [3]) is the observation of the 186 most luminous infrared selected objects in the local Universe ($z \leq 0.088$). These objects all have $L_{3-1000\mu m} \geq 10^{11} L_{\odot}$, and 20 of them even have $L_{3-1000\mu m} \geq 10^{12} L_{\odot}$ (considered as Ultra Luminous InfraRed Galaxies). They display lots of nuclear spectral types, such as Type-1 and Type-2 AGNs, LINERs and starbursts nucleus. For the METIS point of view, these objects are the ones that would have the highest probability to be detected, since they are the most luminous in the METIS bands for the local Universe.
These observations have been made by the SPITZER space telescope, more precisely by the IRAC instrument. This instrument is an infrared imager, with wavebands centered on $3.6\mu m$, $4.5\mu m$, $5.8\mu m$ and $8.0\mu m$: the wavelength domain is shared with METIS. Here the bands used in the analysis are the IRAC-ch1 ($3.6\mu m$) and IRAC-ch4 ($8.0\mu m$) bands. These bands are interesting because they are generated by two different physical phenomena:

- The ch1-band represents the end of the stellar emission, the infrared continuum that is emitted by the stars. Even if the main stellar emission is more centered on the UV/near-UV light, a part of it will be bright enough to be observed in the near-infrared (the Rayleigh-Jean part).
- In the ch4-band, the light emitted is mostly due to hot dust particles that have absorbed the stellar emissions and are re-emitting it with a black-body emission. This band will allow the observation of buried objects, which can't emit in the visible/near-IR because of the dust absorption but become visible in the Mid-IR because they excite the dust which emits at these wavelength.

For this reason, it might be interesting to identify the number of objects that could be detectable at these wavelengths, which are wavelengths shared by METIS and IRAC.

The resolution of the instrument can be found easily with the relation $\theta \approx 1.22 \times \lambda / D$ (rad). With an aperture of 0.85 m, Spitzer/IRAC resolution is approximately 45× less important than the ELT/METIS one. The consequences on the results will be discussed afterwards. Because the technology used to create the Spitzer/IRAC instrument is way older than the one that will be employed on the ELT/METIS, the sensitivity will also be less important.

A.1.2. Extraction of the data

Like most of the legacies, the data from this survey are public and available on the website `http://irsa.ipac.caltech.edu`. For extracting these data, a file needs to be created with the location of the objects from GOALS. The website will then return a ".bat" file, with the link for all the images ".fits". The problem here is that these images are from the four IRAC channels plus more information that are useless for the analysis, and only one was desired at a time. A small IDL routine extracts the right information from the file using the tools *IndexOf("IRAC-ch1")* for example. Once the files retrieved, the surface brightness from each of these files needs to be read in an automatic way. After looking at the flux of several objects, it appeared that the flux is dropping really fast outside the center of the object. In fact, apart from the maximum surface brightness, most of the pixels around don't have enough surface brightness to be detectable by METIS (cf subsection A.1.4). So the surface brightness that was interesting for the analysis was the maximum surface brightness of the object. But the problem is that in a ".fits" given by IRAC, several objects can appear (cf the stars in Figure A.1 inside the circles).

In that case, the maximum of the image is not necessarily the maximum for the object. For this reason, the research for the maximum needs to be concentrated in a small square around the exact position of the object center, as it is shown in the image. After few tries, a square of 10" was giving good values, in the sense that the reduction of this size was barely changing the results obtained (the maximum of the object was indeed taken) but a higher value increases the maximum found for some images (other objects were taken into account,

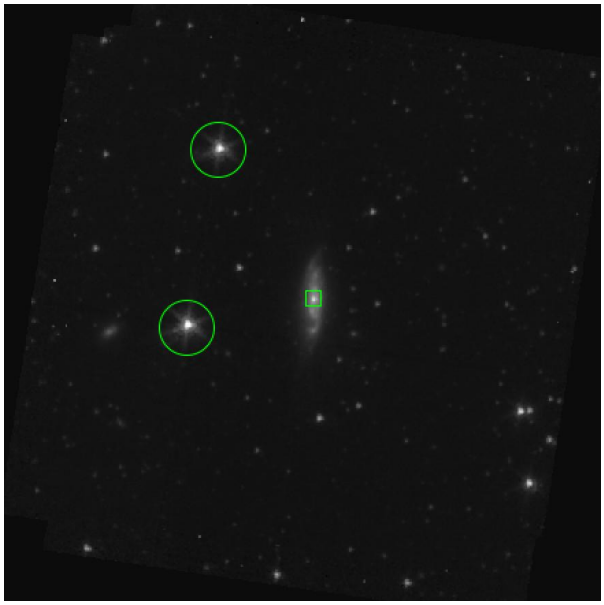

Figure A.1: Illustration of the problem of maximum research in an IRAC ".fits" image

which are not necessarily the studied objects but rather stars around for example). For the exact position of the object, it is found in the header of the object, extracted with the IDL function *extast*. The RA and Decl are then found using the function *sxpar()*, with the key words RA_ref and Decl_ref.
We are conscious that this method is not perfect, mostly because the coordinates given by the keywords *RA_ref* and *Decl_ref* might not be at the exact center of the object. But it is a good first approximation to have a qualitative representation of the GOALS maximum surface brightness.

A.1.3. Results

Finally, an histogram has been plotted. The y-axis represents the number of objects that are found for the x-axis value of maximum surface-brightness. The red line represents the sensitivity for a resolved source found on the talk from Schmalzl and Meisner, 2013 [68], assuming a Strouhal number $SR \approx 1$. The value of sensitivity found in the literature has been divided by 2, so that the sensitivity is calculated for a S/N ratio of 5: this is the incertitude used by convention in physic to decide whether a result can be identified as true or as a possible error. A 5-sigma result represents a confidence interval of 99.99994%. The galaxies detected by the ELT/METIS will be the ones on the right of this red bar, which is approximately **126 objects out of the 186** from the survey. The surface brightness have been contained between 0 and 500 MJy/str for better visibility, the objects above this limit are probably errors (stars instead of galaxies) or unique objects that are not statistically representative of the galaxies sample.

The same protocol can be done for the IRAC-ch4 band. The histogram can be found in A.2b. The sensitivity of the instrument has been changed and can also be found in Schmalzl and Meisner, 2013 [68]. This value has also been divided by 2 to have a S/N = 5.

A.1.4. Discussion

As it can be seen on the A.2a, the majority ($\approx$ 70%) of the objects have a central surface brightness which will be above the METIS sensitivity for the L-band, and $\approx$ 25% for the N-band (cf A.2b). Which means that for these galaxies, METIS will be able to see the central part of these objects. However, few things have to be taken into account:

- First, the sample used needs to be considerate. As it has been stated before, GOALS is a survey of the most luminous infrared galaxies in the local universe. Which means that being able to detect them is clearly not an achievement, especially not for an instrument such as METIS that will be launched in 2030. The detectability of the majority of the objects is a good and reassuring thing, but it is normal. It is the opposite that would have been surprising, and frightening. In that state of mind, it can be noticed that "only" 25% of them are detectable in the N-band.

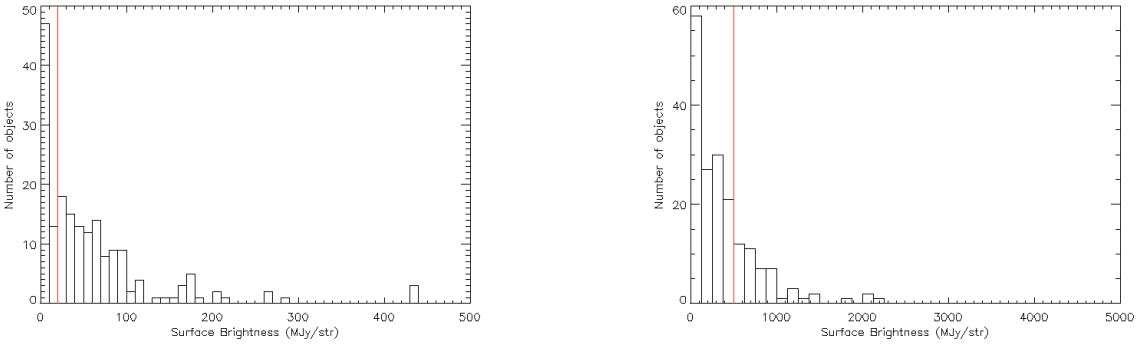

(a) IRAC-ch1 (3.6μm)

(b) IRAC-ch4 (8.0μm)

Figure A.2: Histogram of the maximum surface brightness for the GOALS population

- Second, one needs to remember that this is the MAXIMUM surface brightness of the object. And for lots of objects, especially for LIRGs and ULIRGs which are often powered by very compact sources such as AGN in their center, the surface brightness is dropping really fast out of this very luminous center (which is what is observing for most of the object in the GOALS survey). The illustration of this problem have been made by doing a mean on the values inside the square presented on Figure A.1. The values displayed are the sum of all the pixel's surface brightness in the square divided by the number of pixels inside.

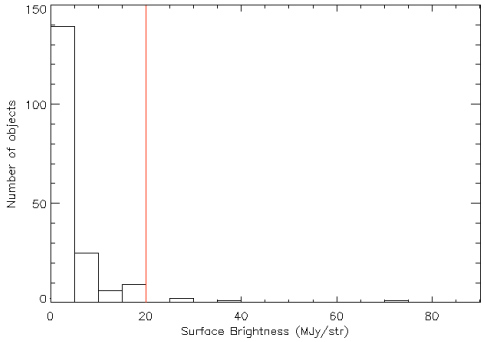

Figure A.3: Histogram of the mean surface brightness in a square of 10" for the GOALS population

  It represents the global surface brightness around the most luminous point on the galaxy, for a square of 10". As it can be seen on Figure A.1, this square is not really huge and still inside the galaxy. However, it can be seen with Figure A.3 that this is enough for removing almost all the sources from the detectability range of METIS. The first conclusion can be drawn thanks to that about the potential sources for METIS: the major part of the galaxy except for the central bright nucleus will be invisible for METIS, which comforts our idea that only the maximum surface brightness needed to be studied for this survey.

- Finally, it can be seen that there are 3 times less objects that can be detected by METIS in the N-band than in the L-band. Which is probably a consequence of the growing sensibility limit for the N-band, way faster then the SED of the galaxies for the same wavelengths. The L-band may be the most sensitive band of METIS to detect faint objects, whereas the N-band might be used only for very compact and luminous ones.

Now that the study have been conducted on a particular sample of galaxies, the same principle is going to be applied on a broader sample, which is the S4G survey. Let's see if the conclusions drawn by this analysis are the same.

A.2. The S4G survey

A.2.1. Presentation of the survey

The Spitzer Survey of Stellar Structure in Galaxies is a survey that concerns about 2,300 nearby galaxies at $3.6\mu m$ and $4.5\mu m$ (cf Muñoz-Mateos et al., 2015 [50]). On the contrary of the GOALS survey, this is a very deep survey that probes objects with a surface brightness of up to 27 $mag\ arcsec^{-2}$ at the wavelength of $3.6\mu m$. For our analysis, the 100 most luminous objects will be considered at the IRAC-ch1 ($3.6\mu m$) wavelength.
For the METIS point of view, these objects represent a more standard population of galaxies, even though the most luminous ones have still be selected.
These observations have been made by the SPITZER space telescope, with the same characteristics as the ones in the previous analysis.

A.2.2. Extraction of the data

With the exact same protocol as before, the maximum surface brightness can be extracted for the ".fits" files of the S4G survey. The only differences are the syntax ones that are slightly different from one survey to another.

A.2.3. Results

Here is the histogram of the MAXIMUM surface brightness of the 100 most luminous object in the S4G survey.

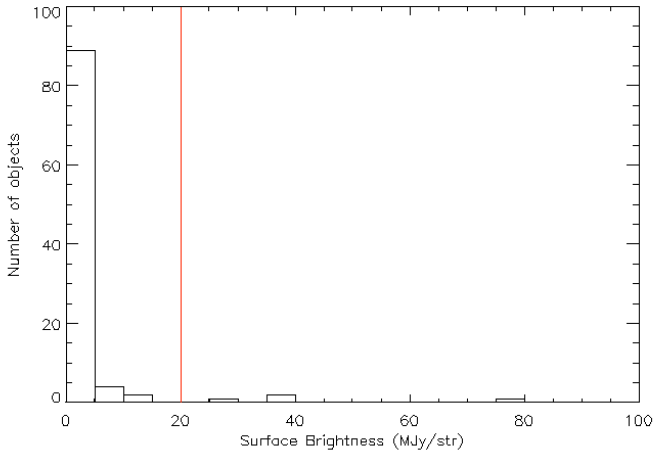

Figure A.4: Histogram of the maximum surface brightness for the S4G population IRAC-ch1

The red line still represents the detection limit of METIS for S/N = 5 in the L-band.

A.2.4. Discussion

As it can be seen on this histogram, almost all the objects are undetectable by the ELT/METIS. Which means that for a "standard" population of galaxies, the METIS instrument won't be able to detect the majority of them, only the few brightest and only near the center. It has been proved in the talk from Brandl, 2015 [14] that even with a larger diameter, the sensitivity for extended sources on an ELT remains the same as on a 4-meter telescope.

However, the resolution from the telescope will be way more important than the Spitzer space telescope. Even if it makes the surface brightness even lower in the case of extended sources, it can also resolve way smaller sources. The Figures A.5a, A.5b, A.5c illustrate well the difference of resolution between the two instruments. The green circle is 1" radius. As it can be seen, the image is much more compact in the second case, which means that the surface brightness of the object appears much higher for this observation. One pixel of the IRAC image can approximately be considered as the mean of 20×20 pixels from the HST/ACS image. For this reason, objects whose maximum surface brightness is not above $20 MJy/str$ with the IRAC images (blue line)

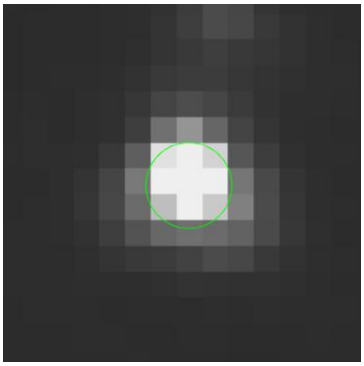

(a) Spitzer/IRAC-ch1 image (1" diameter circle)

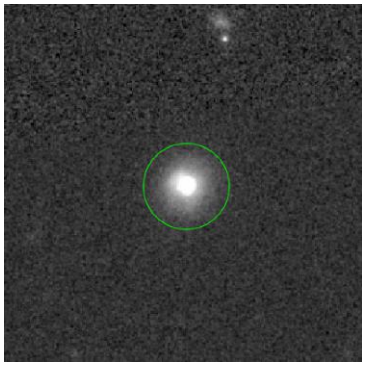

(b) HST/ACS-F814W image (1" diameter circle)

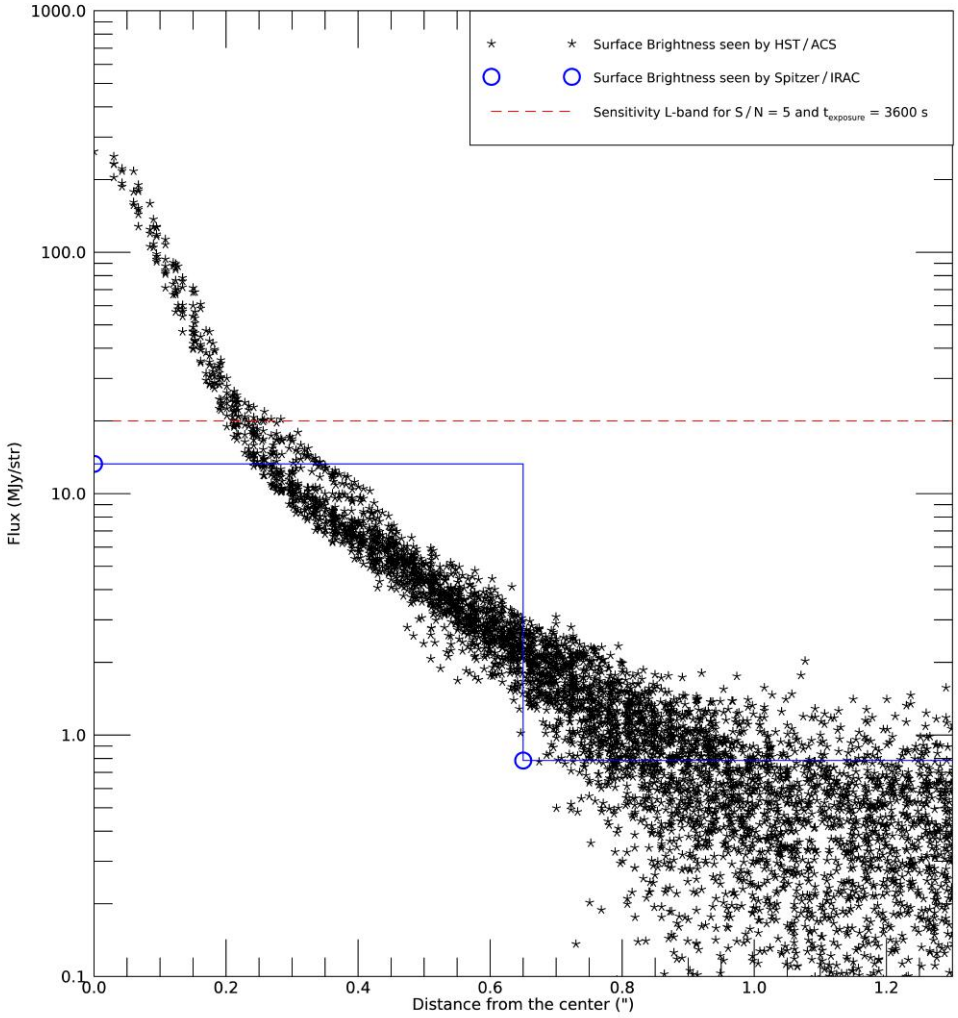

(c) Surface Brightness VS Distance from the center

Figure A.5: Comparison between a SPITZER/IRAC (3.6μm) and a HST/ACS (0.8μm) image (COSMOS) for illustrating the problem of resolution

can have a part of them above this limit with HST resolution (black dots), as it is shown in Figure A.5c. And since the METIS resolution is even higher than for the HST, this might be even more true for METIS images.

For this reason, some objects that have not been detected in the two previous surveys might contain a part detectable in higher resolution observations.

The conclusion from this second analysis reaches the same as the first one: very few objects are detectable, and the one that could be detected are only detected near their center, where the AGN, starburst or stellar activity is high enough to heat the dust which will re-emit in the mid-IR, and create a detectable signal. It can also be noticed that the most frequent objects detected will probably be very luminous and compact objects. So probably AGNs. It has been shown in the discussion that the HST and Spitzer images are really different, mostly because of the difference of resolution between the images. The last analysis in the COSMOS deep field will take into account this remark, and try to simulate an image with the resolution of the HST/ACS but with the flux from Spitzer/IRAC in the MIR.

A.3. The COSMOS deep survey

A.3.1. Presentation of the survey

The COSMic-evOlution Survey is a Hubble Space Telescope project, whose primary goal was to create an ultra-deep field of two square degree (cf Scoville et al., 2007 [70]). The size of this field allows the astrophysicist to consider that it is statistically relevant, which means that the properties derived from this field can be applied to any other.

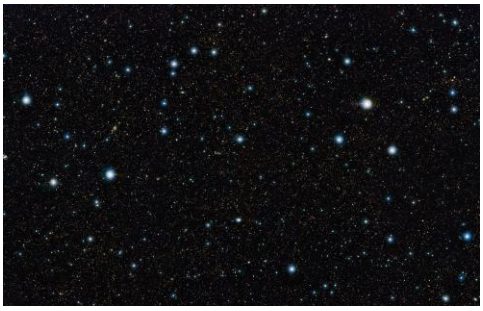

Figure A.6: The COSMOS deep field

This survey have also been seen by several telescopes/instruments, such as the Spitzer/IRAC space telescope, the Very Large Array VLA, the XMM-Newton satellite or even the HST. This is a multi-wavelength survey, creating unique opportunity to do statistical multi-wavelength observations from its objects.

For the METIS point of view, it is very interesting because it means that the objects detectable in this field will approximately be representative of the objects detectable in the entire Universe (the statistic significance of a field of 2 deg × 2 deg, even if it is considered that COSMOS is a little bit less dense that the global Universe density).
These observations have been made by the Hubble Space telescope, more precisely by the Advanced Camera for Survey ACS instrument. The ACS instrument is a UV to near-infrared imager, with a really great resolution and sensibility. The waveband for our analysis is centered on $0.814 \mu m$, which represents the F814W band on the camera. The resolution of the instrument can be found easily with the relation $R \approx 1.22 \times \lambda / D$. With an aperture of 2.4 m, this is approximately $4\times$ less than the METIS's one at $3.6 \mu m$. While still lower than the ELT/METIS resolution, the HST/ACS images are a better approximation of what would be expected from images at the resolution of the ELT.

A.3.2. Extraction of the data

This time, the extraction of the data is slightly more difficult. The concept remains the same: selected objects by criteria, then downloading the corresponding images and making interpretations on the surface brightness of these objects. But the images downloaded will not be the Spitzer/IRAC images at 3.6 μm this time, but rather the HST/ACS images at 0.814 μm. And to have realistic fluxes that can be compared with METIS sensibility, these images are going to be normalized to the flux observed in the IRAC bands. The list below describes the steps of the analysis:

1. The catalog is read, and the data from it extracted thanks to the IDL function *mrdfits*. The data from a the Spectral Energy Distribution catalog (Chang et al., 2017 [20]) are also extracted at the same time. This represents the information on every objects in the COSMOS deep field, such as their flux, AGN fraction, coordinates.

2. Now the relevant objects for the analysis have to be selected. As it has been stated before as a conclusion for the S4G analysis, it represents the most compact and the most luminous objects. Which means the AGNs. For finding them among the COSMOS survey, several criteria have been used:

   - The luminosity is written in the catalog, accessible via the value *splash1* for IRAC-ch1 for example. The selection is made in order to have approximately the 100 most luminous objects in the catalog. A maximum luminosity has also been put to avoid the unrealistic values put by mistake.

   - Then the object selected has to belong outside of our galaxy, so it can be sure that it is not a star. For this reason, a minimum value for the redshift has been set, which is $z = 0.05$. For the same reasons as before, a maximum value has also been set. This redshift has to be true, which is not always the case. The catalog is indexing indifferently stars and galaxies, so what could be taken for a QSO object can be in fact a star. So the idea is to select objects with a photometric redshift to get rid of these errors: the redshift is computed by fitting the SED of objects with a templates catalog of galaxies SED, and the ones with too much incertitude are removed.

   - The coordinates of the object has to be in the HST COSMOS survey, which is not necessarily the case. For this reason, a low-resolution HST image has been taken to identify the precise limitation of this survey (minimum and maximum right-ascension and declination), and limits have been imposed on the selection of objects.

   - It could be useful to see how much the objects detected are "AGN-like". This information explicits whether the object detected with this method is an AGN or not. Dr. Yu-Yen has worked on the AGN-fraction of objects in Chang et al., 2017 [20]. Given a set of measurements for an object at several wavelengths (red points), she has written a script that can reconstruct the corresponding SED seen in Figure A.7 for an AGN (orange curve), a galaxy without AGN (blue one) and a combination of the two (black one). The monochromatic AGN fraction is defined as the ratio between the flux received at a certain wavelength from an AGN (orange curve) divided by the sum of the flux received at this wavelength from an AGN and a galaxy without one. For the total AGN fraction, it's the same but with the flux over all the infrared interval (from $3\mu m$ to $1000\mu m$).

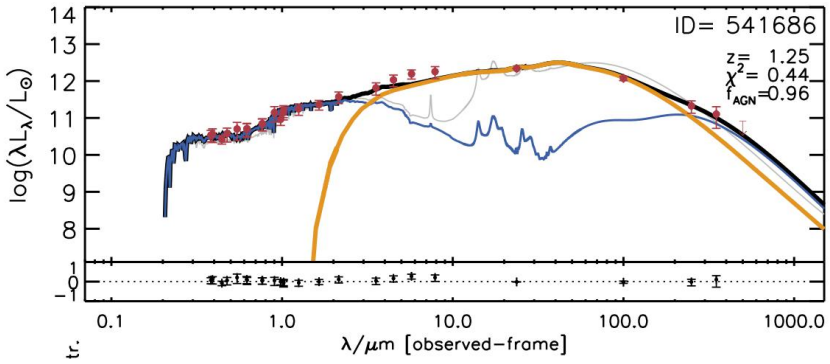

Figure A.7: SED of an Active Galactic Nuclei showed in Figure A.8a by Chang, Y.

According to the literature and her work, the AGN proportion of flux emitted at $3.6\mu m$ over the total flux reconstructed by the algorithm characterized the AGN fraction: a high AGN proportion at this wavelength means high probability of having an AGN buried in the center of this object. For this reason one of the "AGN-like" criteria was an AGN fraction higher than 30%. The other criteria was on the growth of the IRAC flux for an AGN. As it can be seen on Figure A.7, the presence of an AGN creates a positive slope in the interval $[3.6\mu m\ ,\ 8.0\mu m]$. According to the paper of Radomski et al., 2008 [60], the energy provided by the accretion disk of the AGN heats the dust at higher temperature than what the star formation would do. So the thermal emission from the

dust does not start in that case in the Far-IR but rather in the Mid-IR. Has a consequence that positive slope on this interval, which is the second criteria for identifying an object as "AGN-like".

3. Once the criteria have been defined, a file can be written with all the data about the objects selected: their position, but also their luminosity, their redshift, their AGN fraction (the global one) and their index in the catalog. This input is used to recover all the HST images from COSMOS, by using the coordinates to recover cutouts of 5" × 5" in the website http://irsa.ipac.caltech.edu

4. This file is extracted by another program, in addition to the pictures of the objects. The ".fits" images are extracted on IDL using the function *readfits*. The first thing to do is to change the units: the pixels values are in an arbitrary units, and need to be converted to a more physical one, in MJy/str. The function *aper* is used: it is going to measure the flux in a given radius (an aperture of 1" have been used), centered on a given point. This flux is then compared to the real flux measured by IRAC in the same aperture and stored in the catalog, and the image can be normalized with the following relation:

$$I_{new} = I_{old} \times \frac{F_{IRAC}\ (MJy)}{F_{APER}} \times \frac{1}{S_{pixel}\ (str)} \tag{A.1}$$

This method is not very precise, the size of the aperture for the IDL function has been chosen so that it includes all of the object pointed, without including other objects that could add some flux which had not been taken into account in the COSMOS catalog. But for objects such as AGN, it is working fairly well.

The HST/ACS image is now normalized with the IRAC flux, with a resolution that becomes close to the HST one.

A.3.3. Results

Once it is normalized, the surface brightness relatively to the center's distance can be plotted. Thanks to this plot, it is possible to determine whether an object is compact or not, and which part of the object would be detectable by the instrument. It has been plotted for all the object selected in the catalog, and here are presented some of the most relevant ones. The A.8a is a representation of the HST/ACS image with the corresponding surface brightness of this object in A.8b. The red line represents the limit of detectability for the METIS instrument in the given wavelength ($3.6\mu m$), found in the METIS presentation by Schmalzl and Meisner, 2013 [68].

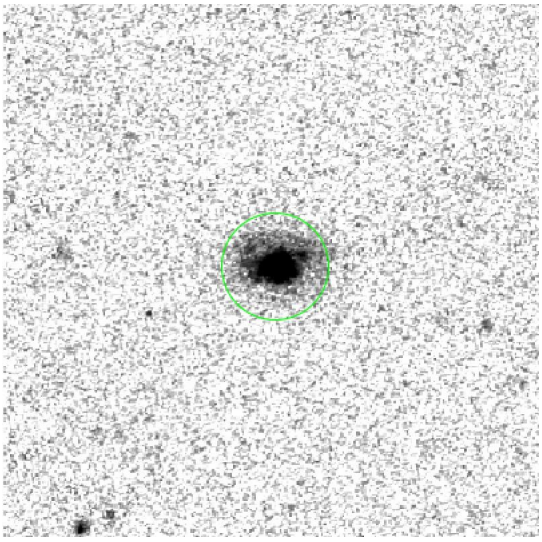

(a) HST/ACS-F814W image (1" diameter circle)

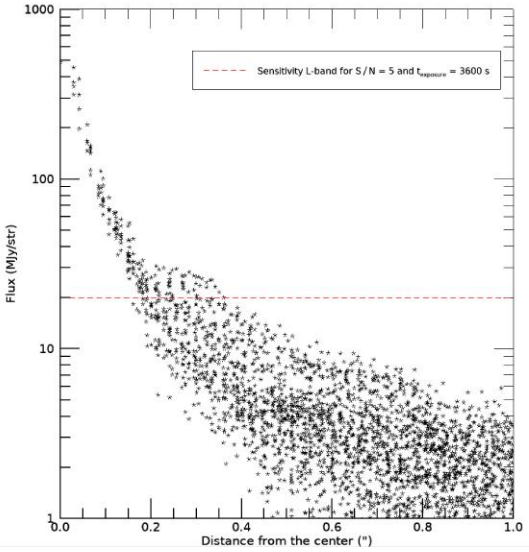

(b) Surface Brightness VS Distance from the center

Figure A.8: Selected object with $z \approx 1.25$ and $\Delta AGN = 94\%$

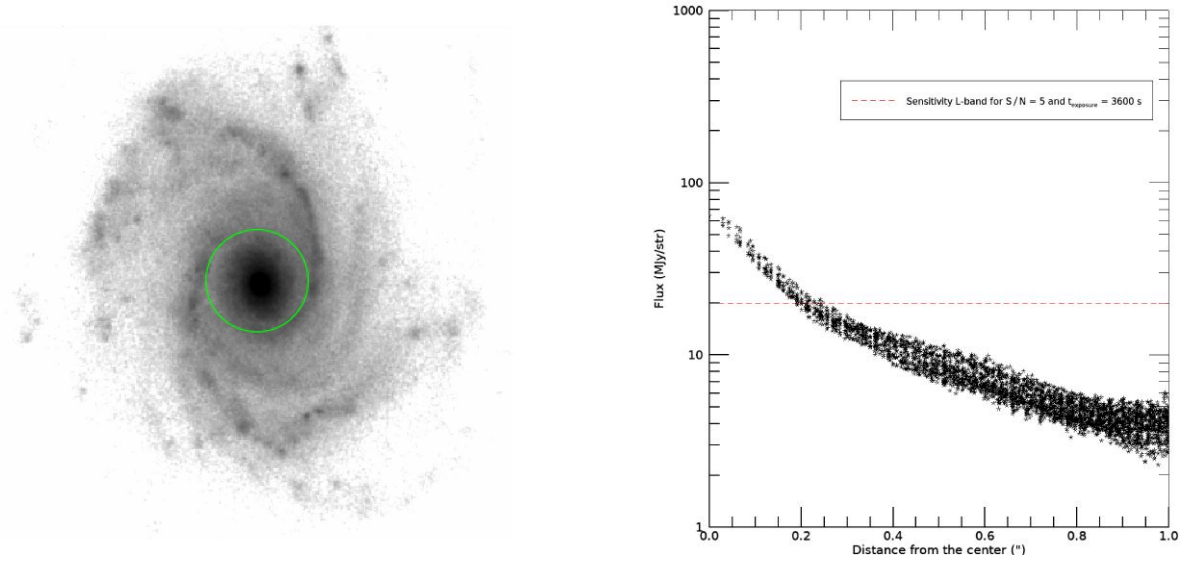

(a) HST/ACS-F814W image (1" radius circle)

(b) Surface Brightness VS Distance from the center

Figure A.9: Selected object with $z \approx 0.23$ and $\Delta AGN = 7\%$

A large part of the object surface brightness is above the detection limit of METIS, so this object's nucleus should be detectable by the instrument. Thanks to these measurements, it is also possible to verify the hypothesis from before, which stated that only the nucleus part of the galaxy will be detectable. The same conclusions can be drawn on the second object on Figure A.9b, with again only the central region of this galaxy detectable.

A.3.4. Discussion

Using these criteria, ≈ 20 objects would be detectable by the ELT/METIS in the L-band. These objects are all ultra-compact and ultra-luminous AGNs. One of the most impressive thing is that some of them are detectable at redshifts up to $z \approx 3-4$. However, several things have to be taken into account:

- First, the wavelength of the flux at which the image have been normalized (IRAC-ch1 at 3.6 μm) is not the same as the one of the images (HST/ACS-F814W at 0.814 μm). And it can have a huge impact on the morphology of the objects. Most of the AGN or starburst places are embedded in dust or gas (that's the material that is in part powering them), which has a consequence an absorption of the light at visible wavelength and a re-emission by blackbody radiation at infrared wavelength. The Figure A.10 below represents the significant difference that different wavelength can have on the morphology of an object: the cold gas and dust cloud absorbs the light from the stars behind it in the visible wavelengths, whereas the infrared photons can penetrate it.

  For this reason, the analysis can be biased, especially because the most luminous objects observed are strong Active Galactic Nuclei or intense star formation places, which are often particularly embedded in dust and gas. The HST/ACS images used to simulate L-band images with a high resolution might be different, with the possibility of very compact regions appearance that are not visible in the HST/ACS/I-band.

- The second thing that needs to be taken into account is the usefulness of these objects' observations. The size of an AGN is typically in the range $\approx 1\ pc$ according to interferometry observations of nearby AGNs (Burtscher et al., 2013 [16]), so even at the ELT resolution the objects will be point like for distances higher than $\approx 10\ Mpc$ in the L-band. The interest is therefore limited if the light is only created by a super-massive black hole, since the observation from METIS will not bring more information than the current instruments, because the SMBH will also not be resolved by the METIS instrument. However, starburst rings in circumnuclear regions very close to the central AGN can also contributed to the emission, such as the one described by Brandl et al., 2012 [12] or the one in the paper of Fernández-Ontiveros et al., 2017 [27]: in the observation here, these clusters might be blended with the central AGN and re-

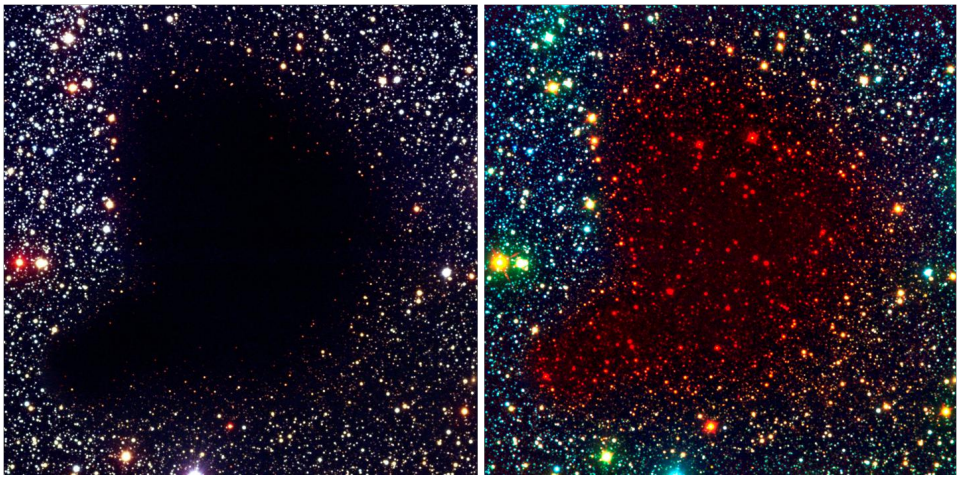

Figure A.10: Comparison between the infrared emission and the visible emission of Barnard 68 (ESO/VLT)

main invisible. Objects are very close (respectively 19.5 Mpc and 49.4 Mpc away in [12] and [27]), it is possible to resolve the clusters even with current instruments, But for higher observation distances, this becomes impossible because of the aperture size diffraction. In that case, higher resolution observations could resolve the star clusters around the nucleus at greater distances than what is currently done (cf section B.1). Their study could help for example the scientists to better understand the coeval growth of the galaxies and the super-massive black hole in their center.

- Finally, even if the light is only emitted by an AGN, the study of these objects spectrum can still be interesting. Since the sources will be point-like for the ELT/METIS, the sensitivity will be more important than the one for extended sources and the objects will be detectable even at very high redshifts. This, combined with the very high resolution ($R = 100,00$) IFU-spectrometer, could bring information on these AGN. This will be described in section B.2.

A.4. Confirmation of the Results

The goal of this part is to be able to confirm the information that have just been presented: METIS will only be able to detect the center of galaxies for $S/N = 5$. In fact, it needs to be proven that only compact and luminous objects will be detectable by METIS, in addition to the proof that such objects exist. In order to do this, simulation inputs created during my internship and a very simple simulation of METIS response have been used. Then, these images simulated have been compared to real data extracted from the CANDELS catalog Grogin et al., 2011 [31], the size of the image and its emitted flux. The purpose is here to compare the results from a study with much less hypothesis, and see if it is consistent with the former one.

The process to create the plot is as follow:

1. The simulation is created with the function *psfgaussian*: the FWHM is implemented so that it represents a typical size of objects observed in our Universe at $z \approx 3$ (Shibuya et al., 2015 [72]). For the fluxes emitted by the entire simulation objects, they are the typical fluxes found for objects at redshift $z \approx 3$. The simulation then needs to be converted in MJy/str to be put in the simulator. The exact same procedure as in Chapter A has been used, using the Equation A.1.

2. Now that the simulation has been created, the response from ELT/METIS needs to be simulated. The image is convoluted with the typical PSF of the ELT/METIS in the L-band (a Gaussian PSF with a FWHM equal to the resolution of the instrument in this band ≈ 0.04"), and a random Gaussian noise equals to METIS sensibility for extended sources with $S/N = 1$ is added to the image (4 MJy/str for the L-band). It was not obvious that the noise that needed to be added per pixel was equal to the noise for an extended source produced by METIS. To determine approximately the value of it, images from the simulator with a high S/N ratio have been used. Once the image normalized in MJy/str with the Equation A.1, an histogram of the values can be plotted. Since the signal represents only few pixels

compare to the total image, the hypothesis can be made that the histogram obtained is the one created by the noise. And the standard deviation observed in this plot is equal to 4 MJy/str, which is the value of the sensibility for an extended source with $S/N = 1$.

3. In the meantime, data are extracted from the CANDELS catalog: the size scale (R_e, which is the radius within which half the light of the object is contained) obtained with the HST/WFC3-F160W camera and the flux of the object (Spitzer/IRAC-ch1) at 3.6 μm. The thing interesting here is that the catalog contains $\approx 35,000$ objects, so the objects detected are statistically representative of the global sky. The objects selected are the ones with the highest surface brightness. After discarding the objects with wrong values (with size not measured or flux with too much uncertainties), the ones with the maximum ratio $F_{3.6\ \mu m}/R_e^2$ are chosen, which represents the object with the maximum compactness

Once the data from both are retrieved, it is possible to plot them on the same graph in order to compare the simulations with the most luminous and compact objects found in CANDELS.

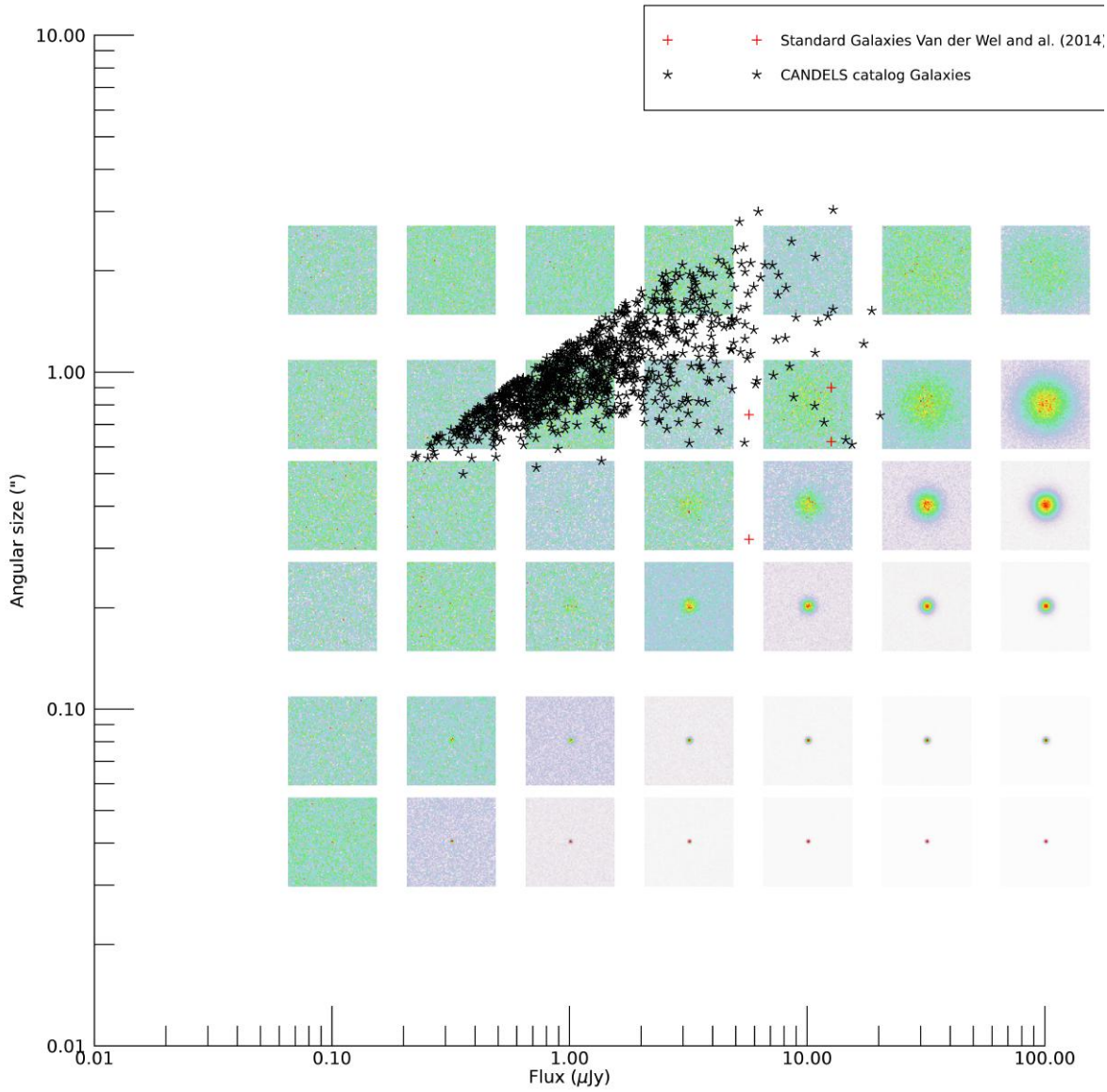

Figure A.11: Comparison between simulations and real observations from CANDELS at $z \approx 3$, for a continuum flux at 3.6 μm (L-band)

As it can be seen on the picture, the conclusions made with COSMOS observations are approximately the same as the one made in the previous part: even the brightest and most compact galaxies (van der Wel et al., 2014 [79]) will hardly be detected by the instrument. However, it is possible that the size of some objects have

been overestimated because of the resolution of the HST/WFC3 instrument. Since the angular size on the plot has been defined as $2 \times R_e$, the instrument can not detect objects with a size lower than ≈ 0.4". Object will a lower size would appear punctual for the instrument, and so the radius size detected will be $\approx FWHM/2$. On the other hand, it can be seen clearly on the plot that such objects would not be really numerous, and even if they were the improvement in the detection will be effective only for objects with flux above 10 μJy.

A.5. Conclusion

The A illustrates well the typical objects that would be detectable by the ELT/METIS, especially at high redshift. Designed to primarily observe extra-solar planetary, the ultra high resolution constrains the objects characteristics observable by METIS. They have to be compact and luminous. These objects, already rare (less than 100 objects could be detected by METIS in the COSMOS deep field according to our simulations, for more than half a million object in total there), are mostly LIRGs or ULIRGs with AGN at their center, Star Forming Galaxies and their clumps at low redshift and compact star forming galaxies at very high redshift.

Chapter B

Scientific cases for METIS

In the A, precise constraints have been defined for the detection of candidates. The purpose of this part is, starting from the constraints defined, to present objects that might be detectable by the ELT/METIS, whose detection would be scientifically relevant. The scientific interest of these objects will also be discussed.

Contents

B.1. Observation of super star clusters in the local Universe

B.1.1. The super star clusters

Super star clusters are really young and massive clusters, which might be the structures from which originate the globular clusters. The young and massive stars ionize the environment of the cluster, creating HII regions. These regions are usually embedded in dust, which means that the extinction is very high. The only way to observe them is usually by infrared and radio observations. They are called "super" because their high luminosity and compact sizes are way above the usual star clusters. Their mass is typically $\geq 10^5 M_\odot$ within radius $\geq 5pc$ and ages $\geq 100\ Myr$ (Alonso-Herrero et al., 2002 [2]). The super star clusters are predominantly found in starbursting and merging galaxy systems, even if lots of them have been found in more standard ones such as the barred galaxies and classic spiral ones (cf B.1a).

The primary characteristics for the formation of stellar clusters is a star formation efficiency greater than ≈ 0.2 to 0.5, in order to avoid the gaseous material to be expelled by the early formation of massive stars (stellar winds, supernovae). A high pressure environment can also help the cluster to remain bound: the star formation can happen on a shorter timescale, and the materials are less likely to be expelled.

The observation of stellar globular clusters could be interesting and feasible, because they are very compact and luminous objects. Since they are mostly observable in the infrared and radio wavelength, high resolution

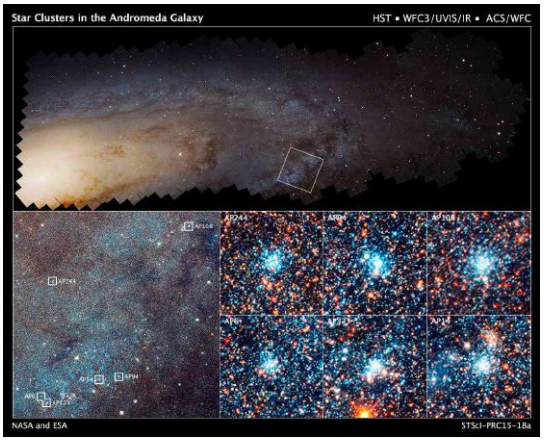

(a) The Andromeda galaxy and the Super Star Clusters in it (NASA & ESA images)

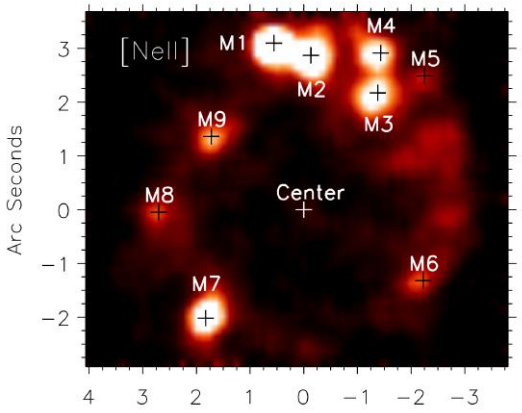

(b) NGC-7552 (19.5 Mpc) Image from the VLT/VISIR at 12.8 μm from [12]

Figure B.1: Example of Super Star Clusters in a standard galaxy (left) and an active one (right)

observations are currently difficult. For this reason, their sizes are not really well known on distant galaxies and only upper limits can be made. At 19.5 Mpc with the VLT/VISIR instrument (cf Figure C.3b), the sources appear as punctual according to the work of Brandl et al., 2012 [12]. Which means that their size must be under 30 pc of diameter. But thanks to the high resolution observations provided by the ELT, it would be possible to better constrain the size of this object, and even to resolve it for close distances.

B.1.2. Detection of the super star clusters

The first problem was to constrain the "standard flux" emitted by these kind of objects. For this reason, the flux at 12 μm was taken from several publications and added to the same graph.

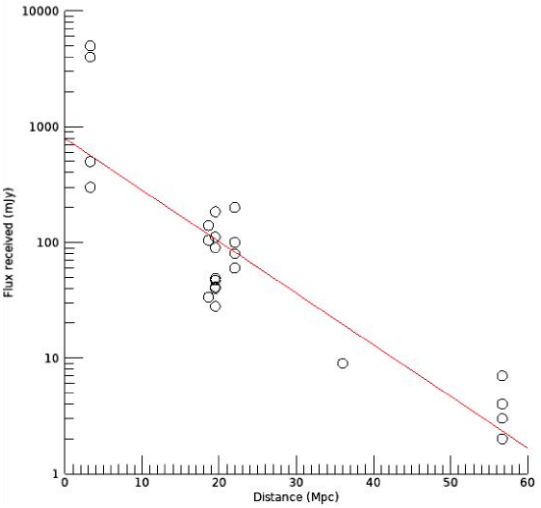

(a) Flux received from the clusters ([12] [44] [29] [11] [7] [6])

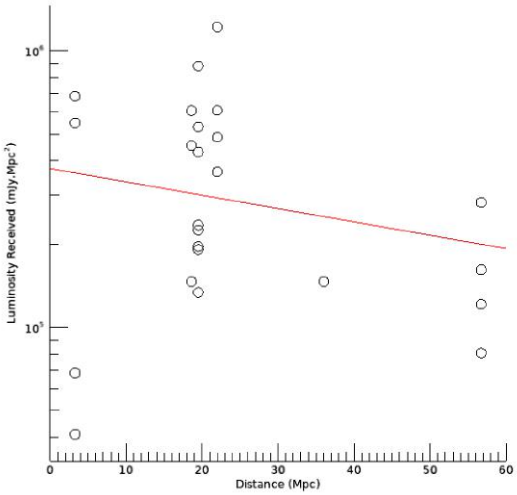

(b) Luminosity received from the clusters

Figure B.2: Population of clusters at 12 μm extracted from several papers

From this graph it is approximately possible to identify a "standard" population of super star clusters, which are for example the ones presented in the paper of Brandl et al., 2012 [12] (they are equally scattered along the correlation between the distance and the flux). The question is now to determine, from the current flux measured by a standard cluster, what is the maximum distance at which they could be detected, considering that they appear punctual for the METIS instrument (which is true for distances greater than $20 Mpc$ at 12 μm, for a supposed size of less than 10 pc per the B.3a).

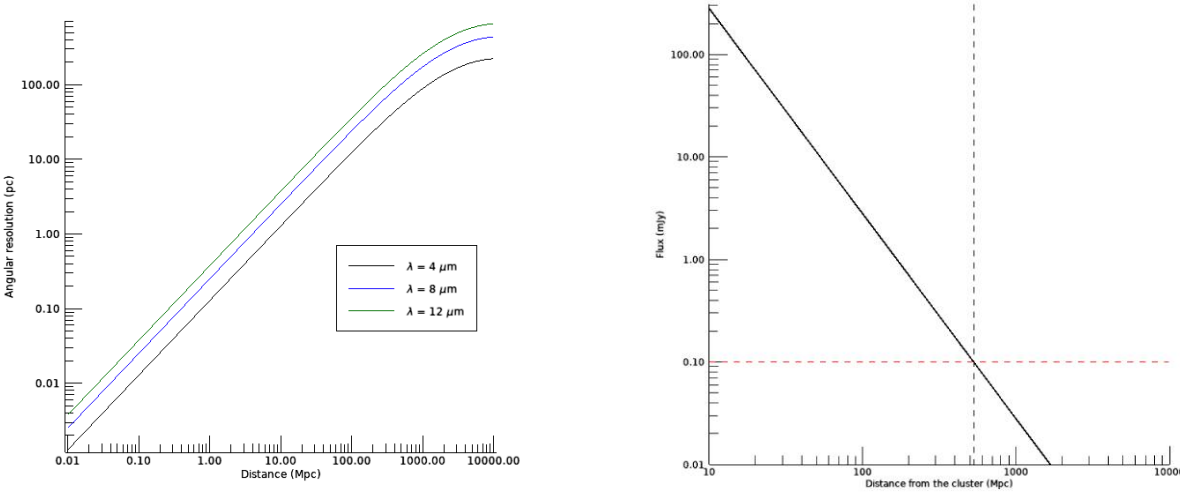

(a) Physical resolution plot at several distances for the L/M/N-bands of METIS

(b) Flux received from a cluster for a given light distance at 12 μm

Figure B.3: Plots made for this "normal" population of super star clusters

The Figure B.3b represents the evolution of the flux for a "normal sized" cluster. The red dot line represents the limit of sensibility of METIS at 12 μm, for an exposition time of 3600 sec and a Signal to Noise ratio $S/N = 10$ [13]. It can be seen in this figure that the corresponding distance from the observer is approximately 500 Mpc.

Considered as punctual sources, the instrument METIS will be able to detect the super star clusters to a distance of 500 Mpc ($z \approx 0.108$) if the object is considered as detectable when its flux is above the sensibility of METIS for $S/N = 10$. The idea here is to use the incredible resolution of METIS not to resolve individually each cluster, but to be able to differentiate the several clusters. At 12 μm, for a distance of 500 Mpc, the angular resolution of METIS will be approximately $\Delta\gamma \approx 150pc$. If the galaxy NGC-7552 is considered for example (Brandl et al., 2012 [12]), the typical separation between the upper and lower clusters is approximately 500 pc. The maximum separation from two clusters is more than two times more the resolution of METIS at the highest detection distance. The instrument would be able to analyze the clusters individually at a higher distance than what is currently done.

B.1.3. Science from Super Stellar Clusters

The question is now to determine what kind of information could be get with these observations.

The resolution combined with less extincted observations in the L-band (with for example Br-α 4.05 μm) line would allow METIS to detect more precisely the characteristics of the star-forming regions. It would be possible to resolve the substructures of the clumps and the interaction between embedded massive clusters for ULIRGs at up to $\approx$ 500 Mpc. As you can see on Figure B.4, the red structures could be further investigated by the instrument, even if the more extended part would be invisible for the instrument. Thanks to the high-resolution IFU, the chemical composition of this environment could be studied in details ([S IV], [Ne II], PAHs, ...) which might lead to the study of the local temperatures and densities of ionized gas which surround the star forming regions or the derivation of the relative ages of the clusters and link it to the star formation histories created by quenching or triggering. Images could even be compared to J-band or H-band observations to trace the dust extinction and therefore the over-density places. All of this would bring more information about this process which, even if more and more studied thanks to infrared observations, remains a mystery in some aspects: what are the processes that trigger the formation of stars at high formation rate ($\geq 1{,}000\ M_\odot/yr$), what is the star formation history of a given galaxy, ... ?

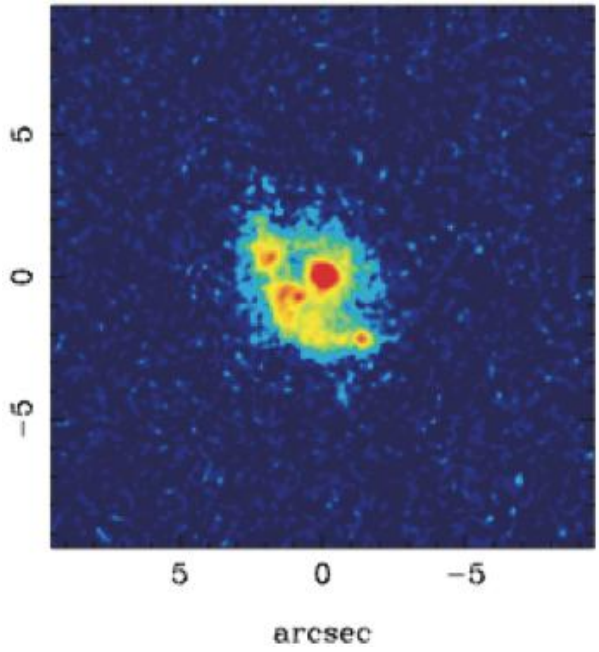

Figure B.4: Example of observations performed from the ground made with the Gemini/T-ReCS by Alonso-Herrero et al. 2014 at 1.1μm, Pa-α band and N-band. ($z \approx 0.014$)

B.2. Observation of AGN in the local and distant Universe

B.2.1. The Active Galactic Nuclei

Active Galaxies are often described as the ones hosted an Active Galactic Nuclei, even if some starburst galaxies are also considered as "active". An Active Galactic Nuclei is a nuclei from a galaxy that emits very important radiations, while its host galaxy might remain relatively normal. The origin of these radiations are thought to be non-thermal radiations, which means emissions that are not due to the thermal emission of a blackbody. The phenomenon seems to be created by the interactions between materials (gas and dust) that is feeding a Super Massive BlackHole located at the center of the galaxy. The mass of these blackholes is very diverse, ranging from $10^5 M_\odot$ to $10^9 M_\odot$ (Netzer, 2015 [52]). While it is thought that almost every galaxy hide a SMBH in its center, only the ones that are currently consuming materials appear as active. For example, the one is our own galaxy is not active, even if its presence can be detected by its gravitational interaction with nearby stars.

The emissions from an AGN are really diverse, and are thought to come from diverse phenomena (Kitchin, 2007 [39]):

- Gamma-ray, X-ray and Ultraviolet emissions, due to the inverse Compton scattering (interaction between very high-energy matter and photons).
- Emission lines in the optical, because of excited atoms that are re-emitting when they come back to less excited states
- Thermal emission in the infrared, from dust heated by the central phenomena that is re-emitting in different wavelength
- Radio emission, created sometimes by radio-lobes but also by the Synchrotron Radiation and the Free-Free radiation not absorbed by dust.

AGNs also sometimes exhibit ejection materials at high velocities: there can be identified as two opposed narrow jets, in addition to rapid variability in their luminosity. All these features are information about the phenomena that are occurring in the central region. Most of these AGNs are deeply embedded in dust, and therefore highly obscured in high-energy wavelength. For this reason, most of them are only visible in the infrared and radio wavelength. The category of ULIRGs discussed in the GOALS analysis are mostly constitute

of AGN: embedded in dust, they heat their dust environment which re-emits at infrared wavelengths the received energy.

B.2.2. Detectability of AGN

As it has been showed in A, the object that are thought to be detectable would be the very compact and luminous AGN buried in the center of the ULIRGs. Since they appear as punctual, they would be detectable even at very large distances such as redshifts 6 or 7. For example in COSMOS the most distant AGN detected would be at $z \approx 2.32$, but these objects are pretty rare and so the results obtained on a $2deg^2$ field might not be representative. Since they are very luminous and punctual, it should be possible to see AGNs even It can be noted that the AGN detected are almost all Type I AGNs (see subsection B.2.3).

B.2.3. Science for AGNs

High-resolution observations with the ELT/METIS will be better than what is currently achieved. However, it will not be enough to resolve the AGN. For this reason, observing AGN with the instrument should have other purposes than putting more constraints on the size, which is in any case impossible to resolve with the instruments.

The unification theorem

The Super Massive BlackHoles are very compact objects. The Figure B.5b represents the typical size of a SMBH, under the assumption of the unification model. This model is an tentative to explain the difference seen between the spectra of a Type I AGN and a Type II (see Figure B.5a). It is one of the most important discovery about AGN for the last decades, and astrophysicists are still looking for evidences that could confirm/infirm it. As it can be seen, the Type-I displays broad emission lines, whereas the ones from the Type-II are very thin and faint. According to this model, the differences observed (size of the emission and absorption lines) come from the viewing angle of the AGN, which center is partially hidden by the dusty torus: seeing face-on, it appears as Type I and edge-on as Type II (Netzer, 2015 [52]).

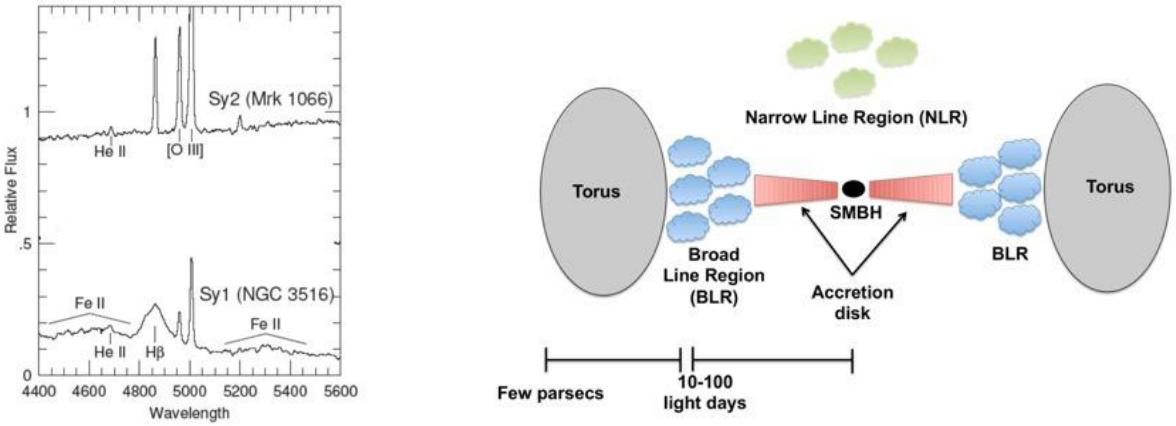

(a) Spectra of Type-I and Type-II AGNs

(b) Schematisation of the unification model

Figure B.5: The unification model for Active Galactic Nuclei

For a Type-I, the torus does not hide the central region, and in particular the Broad Line Region. This region is formed of individual dense gas clouds that are typically 1 AU across, orbiting in more or less random orbits around the central core inside the torus. The Narrow Line Region consists of approximately the same type of object, but the main difference is that this region is located far away from the SMBH. For this reason, the temperature of the BLR is way higher, in addition to higher velocities. Which means highly ionized particles and, because of the Doppler effect, broad emission lines that can be seen on the spectra. However, for Type-II AGN, the light observed on the Type I AGN is blocked by the dusty torus so that only the light coming from the Narrow Line Region is visible. Strong evidences due to the observation of polarized light coming from the AGN support this idea. Light coming from the BLR that has been reflected on the torus has been observed at a certain polarization angle, showing that the region still exist on a Type-II AGN but seems hidden by the dusty torus. However, there are also observations of the variability of the emitted light or the discovery of

intermediate Type of AGN (Type 1.5) which make the astrophysicist believe that the unification model is more complicated than the simple presence of a uniform dusty torus.

One of the particular aspect of this model is that the dusty torus, composed in part of Silicate grains, is supposed to emit in the N-bands at $\approx 9.7 \mu m$. Thanks to the high resolution of the ELT, METIS would be able to better constrain these emissions to help providing evidences in agreement/disagreement with the unification model, like a better characterization of the dusty torus, which is now thought to be consisted of small dense clouds scattered rather than a uniform dusty cloud. Another thing that could be interesting would be to measure the mid-IR continuum, which is linked to the conversion efficiency of nuclear UV/X-rays to IR. Thanks to that, the dust-covering fraction of the AGN could be measured, which might also bring information about the unified model. These observations can not be done with the current instruments, due to a lack of sensitivity or resolution. But with the ELT/METIS, it would become possible to resolve the central region and to measure it without being perturbed by the stellar, gas or dust emission around it.

The AGN-SFR connection

One thing that is particularly remarkable with SMBH is the observed link between them and their host galaxy, even more if it is taken into account that $R_{Host} = R_\bullet \times 10^8$, (the size of a rock compared to the Earth radius) and $M_* = M_\bullet \times 10^4$ (a coin of 2€ compared to an adult) for a "standard" galaxy. The best correlation found is the one between the mass of the SMBH compared to the velocity dispersion of the bulge, which is linked to the mass of the bulge (cf Haehnelt and Kauffmann, 2000 [32]). Another thing that can be noticed is that this correlation extends from $\approx 10^4 M_\odot$ to $\approx 10^{10} M_\odot$, so for a very broad range of mass. Current explanations of the link between the two are using the SMBH feedback on the AGN host, with the disk winds and jets that would push the gas out of the galaxy, quenching the star formation. However, to bring evidence for these theories, the formation of these SMBH need to be observed, which means that AGN need to be seen at redshift $\sim 7-8$. Since these objects are particularly embedded in dust, they are only visible in the infrared. Moreover, the redshift makes them even redder. ELT/METIS observations would be a unique opportunity to shed light on some of these mysteries.

B.3. Sub-millimeter galaxies

B.3.1. Description of the object

Sub-millimeters galaxies, also called Dusty Star Forming Galaxies are one of the most important discovery of the 1990s in astrophysics. Their particularity is that they are so bright that even at really high distances ($z \geq 6$) they are still visible in the sub-millimeter wavelength, in spite of the extinction, the redshift, ... Current theories based on the fact that the size of DSFGs is lower than the massive quiescent galaxies state that they could be the progenitors of these so called 'read-and-dead' giants after extreme bursts of star formation. Furthermore, the discovery of galaxies at only one Gyr after the big-bang raise some questions about their formation: what are the phenomena that drive their formation, ... (Casey et al., 2014 [19]) ?

All these questions make these objects one of the most observed object for extra-galactic astronomy. For this reason it could be interesting for the instrument METIS to observe them.

As it can be inferred from their name, the sub-millimeter galaxies are objects that are very bright in the wavelength between 0.3 mm and 1 mm. Only a handful of them have been found until recently, but the advent of the Herschel Space Observatory and its observations in the FIR increased the number in a very important manner. Papers such as Oteo et al., 2017 [55] shows that a significant population of unlensed ultrared DSFGs are present at redshift of $z \sim 4-6$. These objects are among the most luminous observed, with SFR for an individual galaxy that could rise up to $\sim 2400\ M_\odot/yr$. However, because of the dust extinction, these objects are not visible in all wavelengths and are for example almost impossible to see in the visible light. The possible history of the DSFGs can be found in the Figure B.6.

As it can be seen on the figure before, the DSGs could be the explanation for the creation of AGNs observed at very high distances, but also the giant dead elliptical galaxies that could be found nowadays.

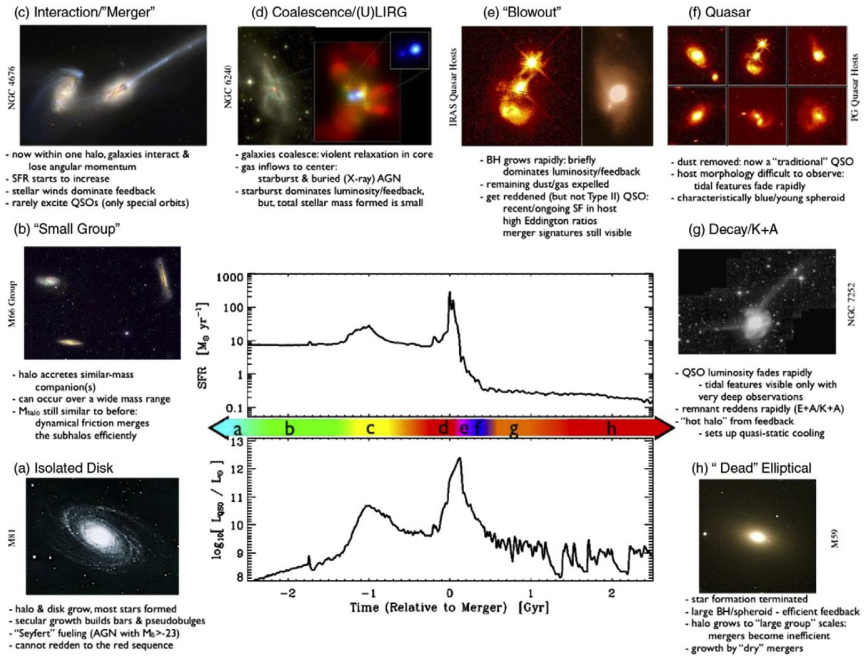

Figure B.6: The evolution of DSFGs over time (Caitlin M. Casey et al., 2014)

B.3.2. Detectability of the object

Here the detection will not be performed by the large bands of the imager, as it has been the case before. The interest here would be to take advantage of the H-α line redshifted in the L-band and use the IFU to detect the star formation rate of these objects at high-redshift. The process to determine whether these objects would be detectable consists of gathering simulations of the METIS response and real observations of objects taken in papers. The goal here is to determine at which angular size and SFR the objects would be detectable by the METIS instrument based on the response of the simulator, and then to determine if such objects exist in the Universe, as it can be seen in Figure B.7.

The figures that can be seen in the background of the plot represent the PSF gaussian that have been created by Emeric Le Floc'h using the IDL tool. This PSF has been normalized to the right star formation rate. But to simulate these inputs, the units have to be in MJy/str. For this reason, the relation from Kennicutt, 1998 [38] has been used, so that the SFR can be linked to the intensity of the H-α line. This transformation will be explained more in details in the next simulation part. Then these plots have been sent to the Leiden University, and simulated in the METIS simulator by Jeff Meisner for an exposition time of 3600 sec under standard seeing conditions.

In this plot, the points represent data that have been found in the literature: on the left part the galaxies represented are classified as LIRGs, and on the right size these are the DSFGs and hyper-luminous ones found at high redshift. The dark line represents the relation between the star formation rate and the angular size of the bright gravitationally lensed galaxy: the "Ruby" Cañameras et al., 2017 [17]. From the typical SFR density of this object, one can derive the relation between the SFR and the angular size at a given redshift. The red symbol represents the typical object (size of $\sim 1-2$ kpc) found in these lensed galaxies. ([55] [36] [59] [48] [35] [56]).

When the SFR was not provided in the papers, the relation from Kennicutt, 1998 [38] has been used to link the FIR luminosity with the SFR.

$$SFR\,(M_\odot.yr^{-1}) = \frac{L(H\alpha)}{1.26\times10^{41} erg.s^{-1}} \tag{B.1}$$

Several things can be observed with this graph:

- First, it can be noticed that the results from Chapter A are confirmed: the standard galaxies and even the LIRGs will not be detectable for METIS because of their lack of compactness. On the diagram, it

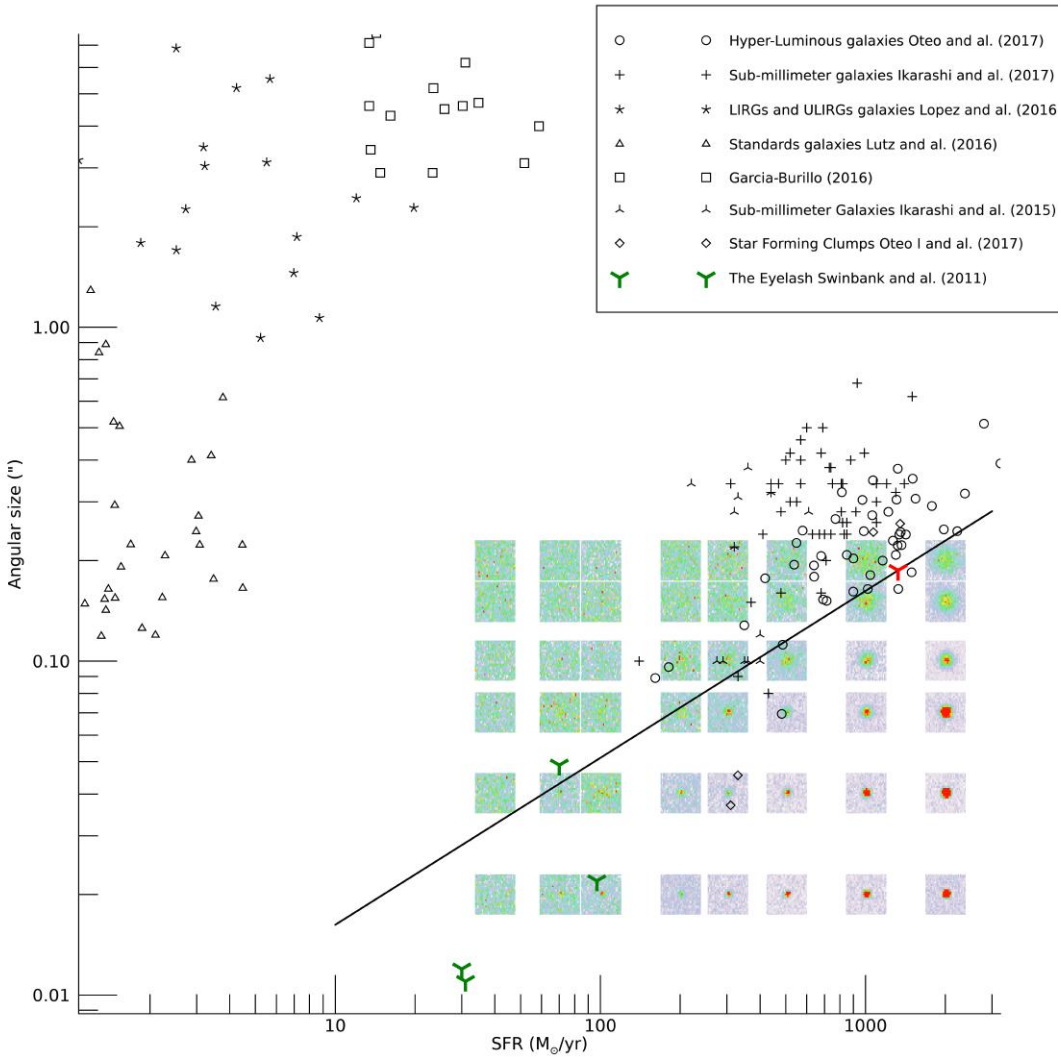

Figure B.7: The comparison between simulations (Le Floc'h E, Meisner J.) and real observations for the H-α emission line at $z = 4$

can be observed that even if some of them have SFRs that can go up to $\sim 100 M_{\odot}$, their important size prevents their detection by METIS (the image have not even been plotted).

- On the contrary, it can be observed that the DSFGs from the literature seem to be at the edge of METIS detectability. Objects magnified by gravitational lensing such as the one in Cañameras et al., 2017 [17] or hyper-luminous galaxies such as shown in Oteo et al., 2017 [55] display sufficient compactness and SFR to be in the range of detection of METIS. The observation of very high redshift star-forming galaxies might be achievable with the instrument.

- Finally, some singular objects can be observed in the diagram that appear clearly in the range of detection, such as the star forming clumps discussed by Oteo et al., 2017 [56]. The compactness of these objects is so important that it makes them perfect candidates for being detected by METIS. The possibility to resolve these clumps could allow the scientists to study their morphology, or even their spectra from different regions thanks to the IFU.

Thanks to the plot, it is possible to show that a certain type of object will be detectable by METIS. The next step will be done in Chapter C, where the observation with the L-band IFU of the object presented in Oteo et al., 2017 [56] will be simulated.

B.3.3. Science on high-redshift star forming galaxies

The interest here would be to carry observations on these distant galaxies to gather information about the star formation few million years after the big bang. The current instruments that are observing the star formation of these objects do not have enough spatial resolution to dissociate the individual contributions of the sub-structures of the source. Being able to constrain more precisely the size of these sources could shed light on some of the current questions about the early star formation in our Universe, when the metallicity and the physical conditions were way different than what is observed in our close Universe. Some information are obtained through the UV light redshifted in the visible bands, where the spatial resolution is still important. However, the UV light is more affected by the extinction than the H-α light. Extinction that was important in these types of objects, which has a consequence a bias in the observations that is not really constrain yet.

Chapter C

Simulation of the ELT/METIS performances

In order to predict the exact performances of the ELT instrument METIS, a simulator has been created by Jeff Meisner and Eva Schmaltz. Information about it can be found in the talk from Schmalzl and Meisner, 2013 [68]. A part of my internship consisted in the creation of several input for this simulator to investigate whether or not they would be interesting to observe with the instrument. I also tried to implement a very simple simulator to test the coherence of my inputs, without having to send them to the real simulator. It allows the detection of big mistakes with unrealistic fluxes for example without taking time from the simulator.

Contents

C.1. Hydrodynamic simulation

C.1.1. Presentation of the simulation

This hydrodynamic simulation represents the merger of the Antennae galaxies (cf C.1a), but at an epoch when the merger was really compact. It has been created in the CEA-Saclay by Renaud et al., 2014 [61]. Mergers are most of the time really interesting for Astrophysicist, and in particular the ones that emits in the infrared. Due to the torque exerted by one galaxy on the other, the gas contained in the galaxies has a tendency to collapse more easily.

The so-called "wet mergers" for example display usually strong starburst zones, sometimes highly buried in the dust and the gas as it can be seen in C.1a. As it has been explained in the chapter 1, the infrared observation will penetrate this shell and allowed the observations of deeply embedded clusters for example. Starburst activity is also compact and luminous in the infrared, most UV and visible emissions. Compact and luminous in the infrared make them perfect objects of interest for an infrared instrument such as METIS.

(a) Galaxies observed by HST/ACS (ESA)

(b) Simulation of the merger [61]

Figure C.1: Antennae-galaxies (NGC-4038/4039)

C.1.2. Creation of the image

The size of the simulation is approximately 5 kpc. The problem here is that the flux of the simulation is not normalized, so to make the simulation for the METIS simulator realistic, it has to be converted to MJy/str. The idea is to use the flux observed at $12\mu m$ by Spitzer/MIPS and use the same method as the one used to normalize the HST/ACS image by a Spitzer/IRAC flux (cf subsection A.3.2). Once the image normalized with the Equation A.1, the distance between the observer and the object can be simulated with IDL. The steps are simple:

1. The flux from the image is adapted. Indeed, without even taking into account the dust extinction or the redshift effect (that changes the wavelength and therefore the flux at a given wavelength, called mostly the K-correction), the flux from an object decreases with the square of the distance. The relation is the following, assuming no beaming effect:

$$F(d) = F(d_{real}) \times \left(\frac{d_{real}}{d}\right)^2 \tag{C.1}$$

2. The size of the image is changed, so that the sensitivity of this image is the same as the one required for the METIS simulator input $\theta = 0.01"/pix$. Using the real size of the simulation which is 5 kpc, the IDL script is calculating what angular size represents this image, and re-scale the image so that the resolution is the same as the METIS simulator one with the function *hcongrid*. If the resolution of the image is too high compared to the desired one, the function is going to lower it by doing a mean on the pixels. But if the resolution was too low, it is going to interpolate the values with a simple polynomial interpolation.

3. Now that the new image with the right resolution has been created, this image needs to be re-sized so that it has the same size as the desired size for the METIS simulator, which is 1024 × 1024 pixels. Again, two possibilities:

   - If the size of the image is larger than 1024 × 1024, then a cut is going to be made using the function *hextract*. The extraction will be centered around the maximum of the image.
   - If the size of the image is smaller than 1024 × 1024, the entire image is going to be placed at the center of an empty square of 1024 × 1024.

4. Finally, a header is created, which includes the scale used ($\theta = 0.01"/pix$), the number of pixel per dimension (1024), the reference value for the pixel (the maximum of the image) and its reference co-

ordinates (RA = 150 deg and $Decl$ = 1 deg). The object is not real, any reference coordinates could be put.

C.1.3. Simulation of METIS performances

Now that the image has been created, it could be interesting to simulate how the ELT/METIS will see these objects. The way to simulate it is the same way as follow:

1. The image is convoluted with the PSF of the instrument with the function *convolve*. The PSF is approximated to be a Gaussian PSF, with the FWHM equal to the theoritical resolution of the instrument at the wavelength of the observations.

2. The noise is generated by the function *randomn*. The standard deviation is set to be equal to the extended source sensitivity of METIS imager for S/N = 1. As it has been seen previously, this is the standard deviation of the noise on the image that is returned by the true simulator, based on the simulation made on the continuum at 12 μm. Once this noise found, it can be added to the image pixel by pixel: for each pixel, a noise has been added which standard deviation is equal to the extended source sensitivity of METIS for S/N = 1.

Again, the hypothesis make the result different from what could be the real output. However, it has allowed us to compare the result from the input with other simulations to test the coherence of the results. You can find on the C.2a the hydrodynamic simulation at several distances.

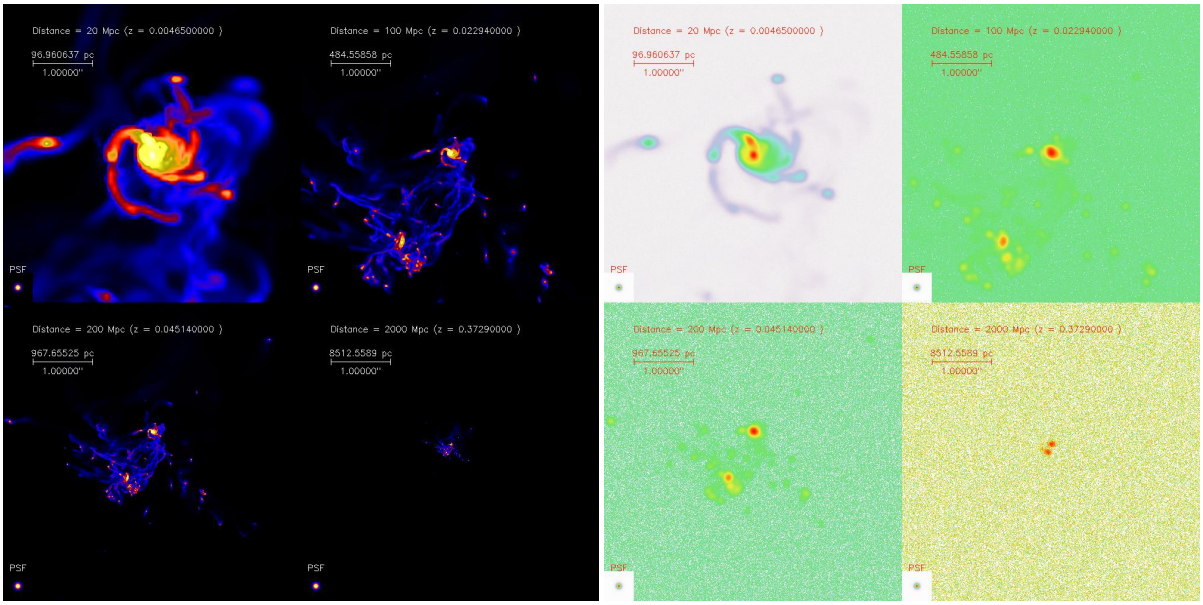

(a) Simulation without noise

(b) Simulation of the METIS simulator response

Figure C.2: Hydrodynamic simulation at several distances (5"× 5") in the N-band continuum

The PSF in the bottom left of each image represents the size of the METIS PSF at 12 μm, which means that beneath this size the instrument will not be able to differentiate two elements and will blend them.

This object represents one of the brightest object in our neighborhood, but at a stage when it was way more compact. As it can be seen on this figure, at 2000 Mpc it becomes impossible to see the features of the object except the central part where the star formation is occurring. This illustrates well the point that shows that the ELT/METIS will only be able to detect the brightest and most compact zone objects, here the two star clusters. However, one can also notice that even at a distance of 2000 Mpc they are still resolved by the telescope. It is still possible to observe the two clusters separately and to determine their properties individually, which is something completely new for that kind of distance at these wavelengths. For that reason, the ELT/METIS could bring some unique information.

C.2. Circumnuclear ring from NGC-7552

C.2.1. Presentation of the problem

As it has been seen in the section B.1, the study of clusters could be very interesting for the METIS instrument. <their size is so small that they will be punctual sources for distances greater than 20 Mpc, even for METIS. However, being able to differentiate them from others could be very interesting: it would be possible to compare for example the flux from the different clusters, and identify relations between their position in the circumnuclear ring and their spectra, in addition to be able to measure their individual contribution to the total flux observed.

At low distances (cf C.3b, the current telescopes are able to resolve the clusters individually. NGC-7552 is not a very common object, and if the astronomers want to study more of them, they will have to search for deeper observation, which means at distances larger than 20 Mpc. Just a reminder, if observation of galaxies like that can be made at 2× the current distance, it means that the volume observed is 8× more important, so way more objects (considering an Euclidian Universe). But at these distances, the angular distance between each cluster is reducing drastically. Only a High-resolution telescope in the infrared could be able to resolve each cluster (which are themselves unresolved) individually. The purpose of this part is to simulate this super star clusters at several distances, and see for which range of distance they are individually detectable by the instrument.

C.2.2. Creation of the image

This time, on the contrary of the section C.1, no ".fits" files have been provided. The images on the paper from Brandl et al., 2012 [12] are not retrievable easily, and they have been post-treated. For this reason, it has been decided to create the image with IDL. The method is simple: each cluster is represented by a PSF with the IDL function *psf_gaussian*, and normalized so that the flux from this PSF is equal to the one provided in the paper Brandl et al., 2012 [12]. In order to place correctly each cluster and respect the distances between them, the WCS system has been used with the coordinates found in the paper Brandl et al., 2012 [12].

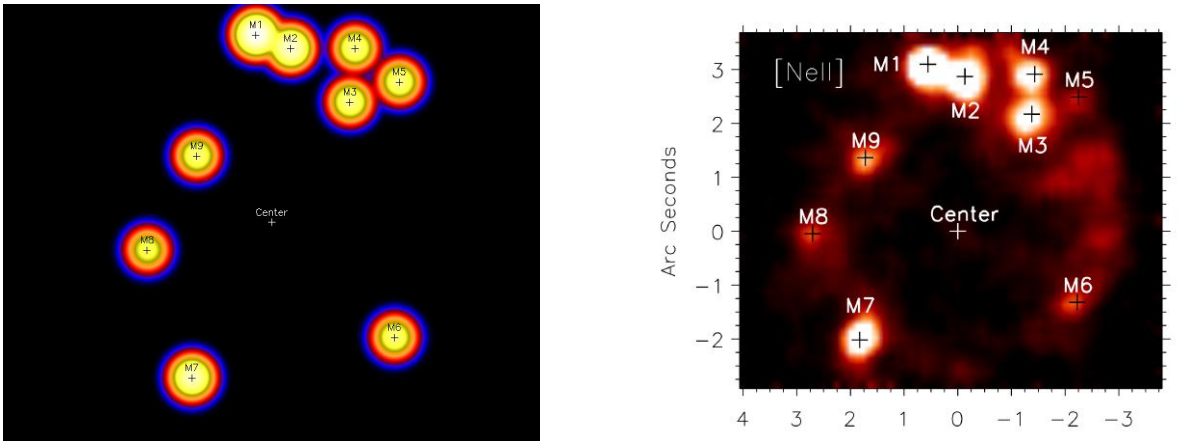

(a) Simulation with the size of the clumps equal to the VLT/VISIR FWHM (= 0.3")

(b) Real image taken by VLT/VISIR (resolution ≈ 0.3")

Figure C.3: Simulation and real VLT/VISIR image of NGC-7552 circumnuclear region

Once this image is created, it can be treated as the hydrodynamic image in the section C.1. This time a real image needs to be simulated, and the VLT/VISIR size limit is a little bit too important for globular clusters. Therefore, the size of the clusters have been reduced to 15 pc, which is already a high value for this type of cluster. The flux used is the flux from the 12 μm continuum.

Again, the image is simulated with the exact same method as the one before. You can find on the Figure C.4a & C.4b the super star clusters simulations at several distances.

The PSF in the bottom left of each image represents the size of the METIS PSF at 12 μm, which means that beneath this size the instrument will not be able to differentiate two elements (without using some de-blending

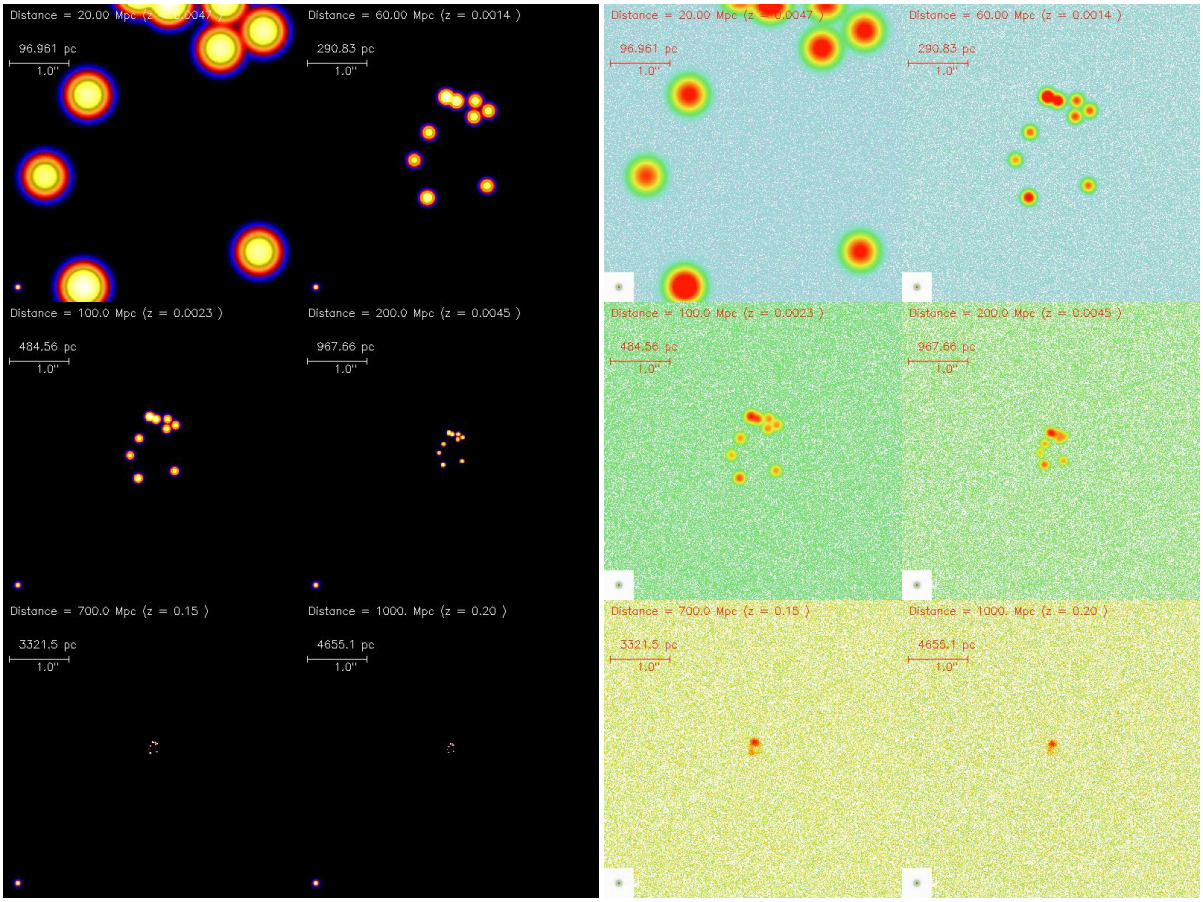

(a) Simulation without noise

(b) Simulation of the METIS simulator response

Figure C.4: The NGC-7552 simulation at several distances seen in the N-band

tools). As it can be seen, even at 2000 Mpc it is still possible to resolve the upper clusters group and the one on the bottom left. Which could be one of the purpose of METIS: using its resolution to dissociate blended objects.

The main incertitude for this simulation is the size of the clusters at 12 μm. These clusters have been modeled by a PSF of 15 pc of radius. As it as been seen in the section B.1, this is an overestimation of what can be found in the local Universe, where it is possible to resolve these clusters. According to Harris et al., 2013 [33], the size mainly depends on the metallicity of the object, its luminosity and its environment. Thanks to the data given in the paper Brandl et al., 2012 [12], the real size can be estimated as ≈ 8 pc. However, this is only a qualitative analysis and the results found are still true.

It can be noticed that these results are in agreement with the analytic calculations made in section B.1. The next step would be to send this simulation, and see if the distance from which the cluster is not detectable anymore is similar to the one predicted in section B.1.

C.3. Sub-millimeter galaxy from ALMACAL-I (Oteo 2017)

C.3.1. Presentation of the problem

As it has been discovered in Chapter B, the objects presented in the paper from Oteo et al., 2017 [56] could potentially be very well detected by METIS because of their compactness and high star formation rate. For this reason it has been decided to prepare an input for the simulator with the same morphology as this object, normalized to its emission in the H-α line. The main problem here is that the emission that will be observed

in the H-α line is not given in the paper: observations have been made thanks to ALMA, and for this reason no information is given about emission in the Mid-infrared, but rather in the sub-mm wavelength. Which is different from the two first other simulations, where the emission in METIS bands was known. One needs to "guess" the value of the flux emitted by the image in this band. This object is at a very high redshift, so the H-α line (0.656 μm) is redshifted in the L-band ($3-4$ μm) for $z \approx 3.6-6.1$. And the ALMACAL-I object has been found at a redshift of $z \approx 3.442$. It can be expected (cf. section B.3) to find similar objects at similar or higher redshift, so that the H-α emission line will be inside the L-band and so detectable by METIS.

C.3.2. Creation of the image

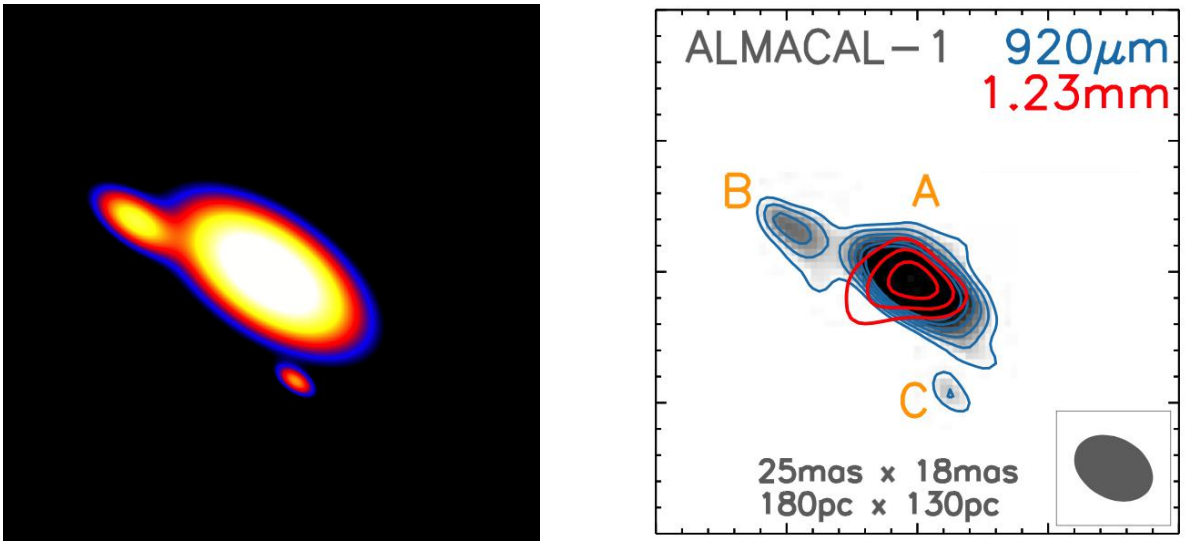

(a) Simulation of the object

(b) Real image taken by ALMA (resolution $\approx 25\ mas \times 18\ mas$)

Figure C.5: Simulation and real ALMA image of ALMACAL-1

The Star Formation Rate have been calculated in this paper Oteo et al., 2017 [56], using ALMA data in the sub-mm for calculating the FIR luminosity which is directly linked to the SFR (Kennicutt, 1998 [38]). Given the star formation rate $\sim 300 M_\odot / yr$ and the distance from the object ($z \approx 3.442$), it is possible to compute the flux of the H-α line from Kennicutt, 1998 [38] with the Equation B.1. Now that this flux has been computed, the flux-density can be found using a typical H-α line profile. By normalizing the SED, it is possible to get the SED of the object in the L-band (assuming only an emission from H-α and a continuum value of $\approx 5 \times 10^{-4} mJy$ found in Oteo et al., 2016 [54]. Once the total flux of the object is calculated, it is really easy to find the surface brightness of the image by using the Equation A.1.

C.3.3. Simulation of METIS performances

Once the image created, the METIS response can be computed. This time, the response we try to simulate is the IFU response. The IFU covers the L and M bands (from 2.9 to 5.4 μm) with a spectral resolution of $R = \frac{\lambda}{\Delta\lambda} = 100,000$. The simulator, as before, adds a noise on the image for each wavelength. In order to calculate the noise, the process has been exactly the same: using an output from the simulator done by Emeric and simulated by Jeff Meisner, the image has been normalized to the right flux and then the standard deviation from the image has been taken, which represents the value per pixel of the noise for $S/N = 1$. Now that the image has been normalized and the noise added, it is possible to "stack" the images along the H-α line. This is simply a sum of the images: the real signal is going to be added but since the noise is distributed as a Gaussian and is completely uncorrelated, it is reduced by this operation.

The following figure representing the object at several distances with or without noise is represented on C.6a.

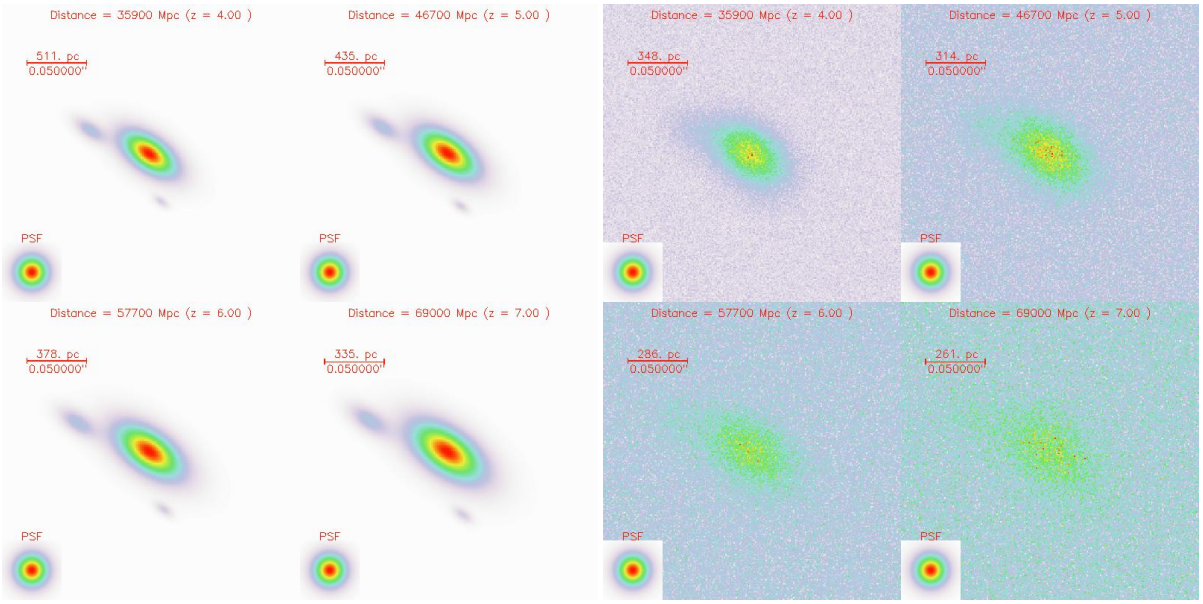

(a) Simulation without noise

(b) Simulation of the METIS simulator response

Figure C.6: The ALMACAL-Galaxy, seen on H-α line

C.4. Remarks

Lots of things still need to be done: the simple simulator has to be tested in addition to the inputs, to determine whether the results obtained here are consistent with the ones obtained with the simulator. As it has been explained before, the performances of the instrument are going to be modified, mostly because there will only be one Laser Guide Star system instead of the 6 recommended for the Adaptive Optics system. Therefore, real simulations would be required to see if the objects proposed could be interesting objects or not. However, these simulations might give an idea of what could be the key observations for the ELT/METIS.